3

Crystalline Whispering Gallery Mode Resonators in Optics and Photonics

Lute Maleki, Vladimir S. Ilchenko, Anatoliy A. Savchenkov, and Andrey B. Matsko
OEwaves Inc.

CONTENTS

3.1 Introduction

Open dielectric resonators with whispering gallery modes (WGMs) are unique because of their ability to store light in microscopically small volumes for long periods of time. The small size of the resonator allows densely packaged optical elements, and the intrinsically high quality (Q) factors of WGMs result in reduced attenuation in photonic circuits.

Evidently, the first indirect observation of WGMs in optics was realized in crystalline WGM lasers when laser action was studied in Sm:CaF_2 crystalline resonators several millimeters in size [1]. Microsecond-long transient laser operation also was observed with a ruby ring of several millimeters in diameter at room temperature [2]. Transient oscillations were attributed to pulsed laser excitation of WGMs with Qs of 10^8–10^9.

WGMs were first directly observed by elastic light scattering from spherical dielectric particles in liquid resonators [3,4]. It was recognized that these modes could help in measurement of the size, shape, refractive index, and temperature of nearly spherical particles [5,6]. WGMs were also used to determine the diameter of an optical fiber [7], and the strong influence of WGMs on fluorescence [8–10] and Raman scattering [11–13] was recognized. Laser action in a free droplet was first studied by Tzeng et al. [14] and Lin et al. [15]. An extensive study of WGM resonators with a focus on their applications was started when high-Q optical modes were observed in solidified droplets of fused amorphous materials [16,17], and after an efficient scheme for coupling with the modes was developed [18–20].

The use of amorphous WGM resonators for practical applications is challenging because of several reasons. (i) The highest quality factor of WGMs in the resonator is determined by Rayleigh scattering occurring due to residual surface roughness and inhomogeneities of the resonator host material [21]. This is generally the case, even though a resonator formed by surface tension forces has nearly a defect-free surface characterized by molecular-scale inhomogeneities. (ii) Amorphous resonators are not environmentally stable. For instance, the quality factor of fused silica resonators degrades with time due to diffusion of atmospheric water into the material. (iii) It is difficult to produce both an optically transparent and a highly nonlinear amorphous dielectric material.

Despite multiple problems including those mentioned above, amorphous resonators are widely studied, and various approaches have been developed to mitigate problems associated with them. Many applications of these resonators have been proposed and some of them are discussed in other chapters of this book.

The primary goal of our research reviewed in this chapter is to return to the early studies of crystalline WGM resonators [1,2] and to develop technologies for controllable fabrication of the resonator, so that various useful properties of crystals that extend beyond the amorphous counterparts can be put to advantage. In what follows we show that this goal, for most parts, has been met. To meet these objectives, we have developed efficient methods of coupling to the high-Q modes of the resonators. Finally, we have used a crystalline WGM resonator for practical optical and photonic applications.

3.2 Fabrication Technique

Any residual roughness on the surface of the resonator results in serious limitation on the achievable WGM Q-factor. Hence, it was commonly believed that high-Q optical WGM resonators cannot be fabricated with transparent crystals. Melting is obviously not suitable for materials with crystalline structure, because it destroys the initial purity, crystalline structure, and stoichiometry of the material. Moreover, during solidification, the original spherical droplet of the melt turns into a rough body with multiple facets and crystal growth steps.

We have fabricated crystalline optical WGM resonators with very high Q-factors ($Q > 10^{11}$) limited in value only by the absorption of the material, and exceeding that of surface-tension-formed resonators. With simple polishing techniques we preserve the original crystalline structure and its composition. In these structures, the unique linear and nonlinear properties of the crystal are enhanced because of the small volume of the high-Q modes. Total internal reflection at the walls of the WGM resonators provides the effect of an ultrabroad band mirror, allowing very high Q-factors across the entire range of material transparency. This property makes crystalline WGM resonators a convenient tool for optical materials studies.

Crystalline WGM resonators, especially those fabricated with sapphire [22], were extensively studied in the microwave frequency range [23]. It was shown that sapphire resonators can have very high quality factors ultimately restricted by material impurities [24]. These resonators were also fabricated using mechanical polishing techniques. However, the requirements on the surfaces smoothness is significantly relaxed in the case of these structures that support microwave modes.

Earlier optical experiments indirectly suggested that mechanical polishing is very promising for the realization of ultra-high Q crystalline WGM resonators. Millimeter-sized calcium fluoride spheres were fabricated by mechanical polishing and WGM resonances were indirectly observed [1]. The fabrication technique described by Bond [25] is based on the mechanical polishing.

In another example, observation of laser action in ruby rings (e.g. 2.38 cm external diameter, 2.22 cm inner diameter with 0.08 cm width, and 0.32 cm height; the C axis was perpendicular to the plane of the ring) suggested the existence of WGMs with $Q \approx 10^9$ [2]. The surface of the ring (except for its inner part) was mechanically polished. A decade later CW laser operation in a Nd:YAG 5 mm sphere was demonstrated [27].

Mechanical polishing of crystalline resonators to obtain high-Q optical WGMs was reinvented at the Jet Propulsion Laboratory (JPL) (Quantum Sciences and Technology Group) 15 years later. A lithium niobate WGM with $Q = 5 \times 10^6$ (at 1.55 μm) resonator was first fabricated [28,29], and the result was repeated by the University of Southern California group

[26,30–32]. The high-Q obtained by mechanical polishing was not a miracle, though. Total internal reflection resonators (another type of open dielectric resonators resembling WGM resonators) made out of lithium niobate have $Q \approx 7 \times 10^8$ (optical path length 1.6 cm, index of refraction 2.19, finesse $F = 6000$, at 2 μm) [33]. The JPL group explicitly demonstrated the capability of mechanical polishing, ultimately producing calcium fluoride WGM resonators with $Q > 10^{11}$ and showing that the material, not the polishing quality, determines the achievable quality factor [34].

Mechanical polishing, along with subsequent annealing, is routinely used to produce ultra-smooth crystalline surfaces. For instance, atomically smooth surface (0.25 nm) on $LiNbO_3$ and $LiTaO_3$ substrates were produced by thermal annealing of mechanically polished samples with 1–2 nm roughness [35]. Even better smoothness (0.1–0.2 nm) can be produced with quartz crystals using soft material polishers, fine abrasive powders, and suitable working environments, and by carefully reducing the mechanical action in the polishing process [36]. Mechanical polishing is not the only technique that can lead to achieving good surfaces. Single point diamond turning is also a very promising approach. For example, surfaces with 3 nm roughness have been achieved with diamond turning of CaF_2 [37].

We adopted various known techniques to fabricate WGM resonators out of different types of crystals. The basic procedure is the following. We start with a crystalline wafer and drill the wafer with a hollow drill to fabricate a cylindrical preform. The preform is then attached to a holder and is either polished or diamond turned. There is no unique recipe for production of a perfect surface. We have achieved ultra-high quality factors by selecting the polishing speed, and the size of the grain in a diamond slurry. As a rule, all the algorithms change from a crystal to a crystal, and from a crystal cut to a crystal cut. To date, the basic achievement is the absence of the Rayleigh scattering in our resonators, which is the basis of the claim that the surface roughness does not restrict the quality factor of crystalline resonators.

Hand polishing works well for fabrication of larger resonators. For resonators with diameters as small as tens of micrometer, diamond turning technique is more suitable. The diamond turning technique we used for fabrication of crystalline microresonators is based on a home-made apparatus [38], and allows precise engineering of geometrical features of the resonator such as surface curvature or profile. We have fabricated magnesium fluoride and calcium fluoride resonators to validate the technique. The quality of the surface of resonators produced with this apparatus is quite high after a final polishing, and is characterized with less than 0.2 nm surface roughness. The quality factor of the microresonators fabricated with CaF_2 exceeds 10^8.

The entire fabrication process of microresonators generally includes two steps. The first step is diamond turning, which employs computer control of a precision lathe. Structures obtained in this step are engineered to about 40 nm precision and have optical Q factors of up to 10^7 (surface quality limited). For instance, a chain of three CaF_2 resonators presented on Figure 3.1 was fabricated with this approach. Resonators are separated by approximately 70 μm and are coupled to each other for efficient energy transfer. If higher Q factors are needed, additional optical polishing has to be performed. This polishing step naturally modifies the structure that is initially obtained by the diamond turning process. Special diamond turning parameters must be employed to avoid brittle machining and to achieve the required surface smoothness. Parameters such as speed of rotation of the workpiece, feed and cutting angle, diamond cutter geometry and sharpness, as well as the type of lubricant are very important in achieving ductile regime of machining [39]. Special attention should also be paid to vibration isolation of the turning process. In our

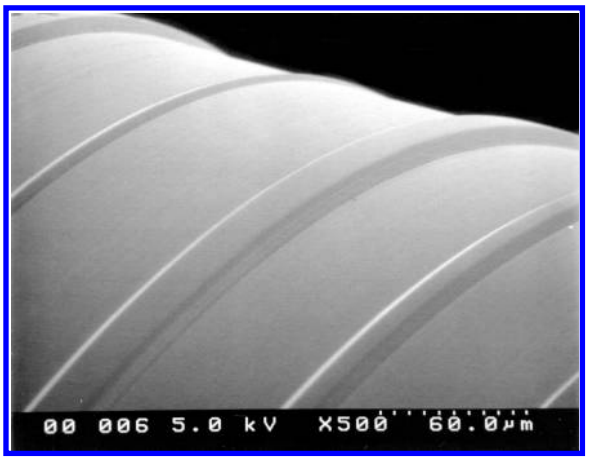

FIGURE 3.1
A stack of three WGM resonators fabricated by diamond turning technique on a cylindrical preform made out of calcium fluoride.

diamond turning setup we use a home-made air bearing to provide the required stiffness and repeatability of rotation of the workpiece. Optical polishing is performed by application of polycrystalline diamond abrasives. Polishing is performed in several steps with decreasing diamond grit size followed by a cleaning process. It was found that small particles are extremely difficult to remove from the surface of the material, and the cleaning process is most critical in achieving ultrahigh Q factor. Cleaning was performed in a clean room environment with the use of organic solvents.

3.3 Coupling Techniques

Efficient coupling of light to microresonators is one of the basic problems of photonics. It is not enough to build a low loss linear or nonlinear resonator; it is also important to be able to send/retrieve light into and out of the device. Thanks to the successful development of waveguide coupling techniques, the first commercial devices utilizing WGMs have now became available [40].

Fundamentally, coupling of light with the resonator is based on phase- and mode-matched power exchange between the mode and the guided wave in a specially engineered coupler (a waveguide or a prism). Parasitic coupling to unwanted modes is quantified by "ideality"—the ratio of power coupled to a desired mode to power coupled or lost to all modes (including the desired mode). Principles of any "ideal" coupling technique are based on (i) phase synchronism, (ii) optimal overlap of the selected WGM and the coupler mode, (iii) selectivity, and (iv) criticality. Phase-matched evanescent field couplers posses all these properties.

3.3.1 Critical Coupling

For the most efficient energy exchange, a resonator must be both ideally, as well as critically, coupled to a chosen waveguide or fiber. The notion of critical coupling, fundamental

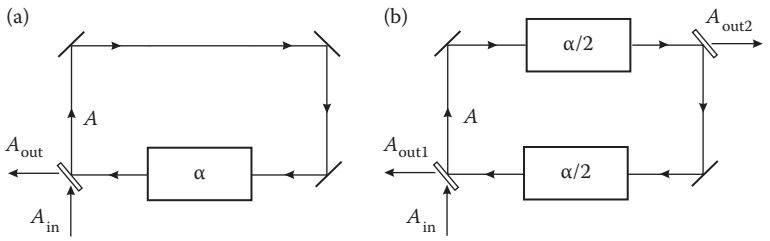

FIGURE 3.2
Models of WGM resonators.

in RF engineering (see e.g. [41,42]), has been recently applied to optical WGM resonators [43]. Indeed, unlike lossless Fabry–Perot (FP) resonators where intrinsic loss is identical to the coupling loss, the strength of evanescent wave coupling to WGM resonators is independent of their intrinsic loss. Criticality implies that the coupling strength between waveguide and resonator must match the loss of any nature to provide a 100% energy exchange at resonance.

Let us model a solid state WGM resonator as a ring cavity containing a linear absorber localized in space (Figure 3.2a). To find the intracavity field A we write the steady state condition

$$A = Ae^{i\omega Ln/c}e^{-\alpha}\sqrt{1-T_c} + \sqrt{T_c}A_{in}, \tag{3.1}$$

where $\alpha \ll 1$ is the (frequency independent) total amplitude absorption of the light in the resonator per round trip, $T_c \ll 1$ is the coupling factor, $L=2\pi R$ is the circumference of the resonator, R is the radius of the resonator, A is the slow amplitude operator of the intracavity light, and n is the refractive index of the material. Equation 3.1 indicates that the steady state of the field amplitude is achieved by compensation of the round trip loss of the external optical pumping A_{in}.

The amplitude of the output pump light A_{out} can be found from equation

$$A_{out} = -Ae^{i\omega Ln/c}e^{-\alpha}\sqrt{T_c} + A_{in}\sqrt{1-T_c}, \tag{3.2}$$

and it is equal to

$$A_{out} = \frac{\sqrt{1-T_c} - \exp[i\omega Ln/c]\exp[-\alpha]}{1-\exp[i\omega Ln/c]\exp[-\alpha]\sqrt{1-T_c}}A_{in}. \tag{3.3}$$

It is convenient to introduce notations

$$\gamma = \frac{\alpha}{L}\frac{c}{n},\ \gamma_c = \frac{T_c}{2L}\frac{c}{n},\ \omega\frac{Ln}{c} = (\omega-\omega_0)\frac{Ln}{c} + 2\pi l,\ 2\pi l = \omega_0\frac{Ln}{c},$$

where ω_0 is the mode frequency, l is the mode number. In the vicinity of the resonance we have

$$A_{out} = -\frac{\gamma_c - \gamma - i(\omega_0-\omega)}{\gamma_c + \gamma + i(\omega_0-\omega)}A_{in}. \tag{3.4}$$

Equation 3.4 shows that all the power is absorbed in the resonator ($A_{out}=0$) if $\gamma_c=\gamma$. This is the condition of the criticality of coupling.

In the case of a WGM resonator with two couplers ("add-drop" configuration, Figure 3.2b) the criticality condition looses its meaning. In fact, the intracavity field in the case of two couplers is calculated from

$$A = Ae^{i\omega Ln/c}e^{-\alpha}\sqrt{1-T_{c1}}\sqrt{1-T_{c2}} + \sqrt{T_{c1}}A_{in}, \tag{3.5}$$

where $T_{c1} \ll 1$ and $T_{c2} \ll 1$ are the coupling factors, for two partially transparent mirrors. Output fields are described by equations

$$A_{out1} = -Ae^{i\omega Ln/c}e^{-\alpha}\sqrt{T_{c1}} + A_{in}\sqrt{1-T_{c1}}, \tag{3.6}$$

$$A_{out2} = Ae^{i\omega Ln/2c}e^{-\alpha/2}\sqrt{T_{c2}}, \tag{3.7}$$

solutions of which are approximated by expressions

$$A_{out1} = -\frac{\gamma_{c1}-\gamma_{c2}-\gamma-i(\omega_0-\omega)}{\gamma_{c1}+\gamma_{c2}+\gamma+i(\omega_0-\omega)}A_{in}, \tag{3.8}$$

$$A_{out2} = -\frac{2\sqrt{\gamma_{c1}\gamma_{c2}}}{\gamma_{c1}+\gamma_{c2}+\gamma+i(\omega_0-\omega)}A_{in}, \tag{3.9}$$

in the vicinity of the resonance. We have taken into account that $e^{i\omega Ln/2c} \approx -1$ in this case. It is easy to see now that the filter is nearly ideal if $\gamma_{c1}=\gamma_{c2} \gg \gamma$. The criticality of the coupling does not make sense here.

3.3.2 Prism

Prism coupling was initially developed to send light to optical waveguides [44–46]. Prism-waveguide coupling efficiency exceeding 90% has been demonstrated elsewhere [47,48]. Prism coupling to WGMs has been investigated both theoretically and experimentally [18–20,49–51]. The best efficiency of prism coupling to WGMs in microspheres reported to date is ~80% [49]. A coupling efficiency exceeding 97% was achieved in elliptical lithium niobate resonators [52]. In this chapter we report on achieving 99% overall nonlocal coupling with a toroidal WGM resonator having 4.2 mm in diameter.

The technique of prism coupling is based on three main principles. First, the input beam is focused inside the prism at an angle that provides phase matching between the evanescent wave of the total internal reflection spot, and the WGM, respectively. Second, the beam shape is tailored to maximize the modal overlap in the near field. And third, the gap between the resonator and the prism is optimized to achieve critical coupling. The loaded quality factor for the prism coupler in the case of the basic WGM sequence of microresonators is given by the expression (see [20]):

$$Q_c = \frac{\pi(n_r^2-1)m^{3/2}}{2n_r\sqrt{n_p^2-n_r^2}}\exp\left(4\pi\sqrt{n_r^2-1}\frac{d}{\lambda}\right), \tag{3.10}$$

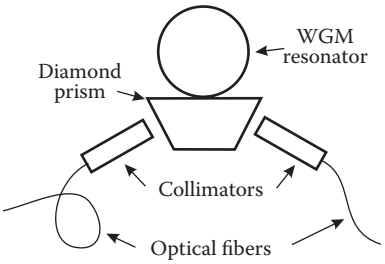

FIGURE 3.3
Schematic of prism coupling with a WGM resonator.

where n_r is the refractive index of the resonator, n_p is the refractive index of the prism, d is the shortest distance from the prism to the resonator, λ is the wavelength of the light in the vacuum, and m is the azimuthal number of the mode. It is easy to see that $n_p > n_r$ is expected.

The schematic diagram of a prism coupler is shown in Figure 3.3. The output of a single mode fiber is collimated and focused on the surface of the prism. The prism is located in the close proximity of the WGM resonator, and the collimated beam is focused on the contact spot between the resonator and the prism. The refractive index of the prism n_p is larger than the refractive index of the resonator n_r, and the phase velocity of the collimated beam along the surface of the prism is $c/n_p \sin\phi$, where c is the speed of light in vacuum, and ϕ is the angle of incidence. The phase velocity of the optical WGM is equal to c/n_r. This trivial approximation is good enough in practice. The modes are phase-matched when

$$\sin\phi \simeq n_r/n_p. \tag{3.11}$$

The phase matching of the modes is not the only factor required for efficient coupling. For example, when the focused beam is not adjusted with the prism–resonator contact point, then there is no coupling at all since there is no aperture matching. Aperture matching is the second important factor for achieving an efficient coupling. Aperture matching with a Gaussian beam occurs when

$$\cos\phi \simeq \sqrt{\frac{r}{R}}, \tag{3.12}$$

where r is the vertical radius of curvature of the resonator in the vicinity of the contact spot, and R is the horizontal radius of curvature of the resonator next to the contact spot. Equations 3.11 and 3.12 show that phase and aperture matching are generally impossible to obtain in the case of coupling with the basic WGM sequence in a microsphere. This is why the best achieved coupling with a microsphere is on the level of 80% [49].

It is possible though to improve the coupling by varying both the incidence angle and some other parameter. Two choices are available for this. One choice is to change the vertical radius of curvature of the resonator, r, i.e. make a toroidal resonator. The resonators rim must be shaped such that

$$r = R\left[1 - \left(\frac{n_r}{n_p}\right)^2\right]. \tag{3.13}$$

Another choice is to select a mode with the effective refractive index

$$n_{\mathrm{r}} = n_{\mathrm{P}}\sqrt{1-\frac{r}{R}}. \tag{3.14}$$

This can be done by selecting modes located deeper in the resonator since

$$n_{\mathrm{r}} > n_{\mathrm{reff}} \simeq n_{\mathrm{r}}\left[1+\alpha_q\left(\frac{m}{2}\right)^{1/3}\right]^{-1}, \tag{3.15}$$

where α_q is the q^{th} root of the Airy function, $Ai(-z)$, which is equal to 2.338, 4.088, and 5.521 for $q=1$, 2, and 3, respectively. Practically speaking, these approaches are both used together. At the onset, the resonator is made so that its curvature parameters satisfy the condition, Equation 3.13. Possible fabrication errors can be fixed by selection of a deeper mode.

It is possible to realize aperture matching with aspherical (astigmatic) optics. An axio-symmetric Gausian beam can be transformed to an elliptical beam that has perfect overlap with modes of an arbitrary WGM resonator. This method is now under development.

The third factor limiting the coupling efficiency is intermodal mixing. WGM modes in larger resonators overlap and interact with each other. The mode of interest emits into other modes limiting the maximum achievable optical coupling (in the sense of the critical coupling). To suppress this effect the number of modes should be reduced by, for example, shaping of the resonator [53]. However, it is possible to achieve excellent coupling even in a toroidal multimode resonator. For example, we have measured 99% nonlocal coupling in a toroidal WGM resonator having 4.2 mm in diameter and 120 μm in thickness Figure 3.4.

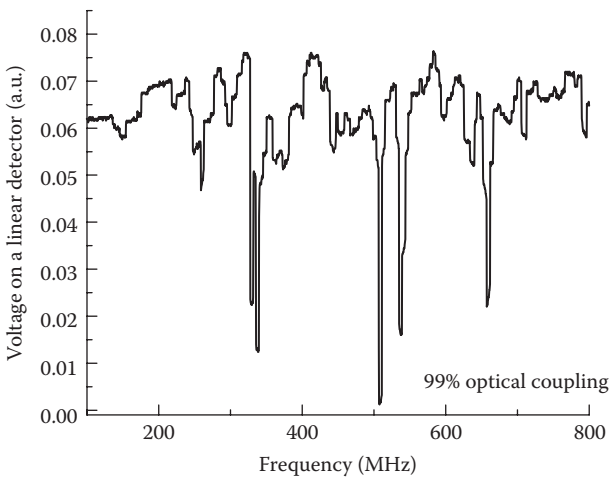

FIGURE 3.4
Spectrum of a WGM resonator taken using a prism coupler. The coupling efficiency approaching 99% is achieved.

It is important to note a common mistake made in the measurement of the coupling efficiency. It is possible to achieve a perfect contrast for the absorption resonance, even though the coupling is far from being critical, by simply changing the position of an output collimator that does not collect all the radiation exiting the resonator. Such an observation is in fact the signature of poor coupling, and the high contrast picture comes from the interference of the light exiting different WGMs. We are aware of claims of 100% coupling achieved with prisms having an index of refraction less than that of the resonator. One of the ways of avoiding such mistakes is to check the output beam profile, which will be Gaussian for the case of perfect coupling.

3.3.3 Angle-Cut Fiber

Another promising method for coupling light and WGM resonators is based on angle-cut fiber couplers. Initially side-polished fiber couplers [54–56] had limited efficiency owing to the residual phase mismatch between the guided wave and the WGMs. Subsequently, a phase-matched coupling technique was developed using an angle-polished fiber tip in which the core-guided wave undergoes total internal reflection [28,57]. Coupling the WGM resonators and semiconductor lasers was also studied by means of a similar technique [58,59].

The main idea of angle-polished fiber coupling is illustrated in Figure 3.5. The tip of a single-mode fiber is angle polished with a steep angle. The light propagating inside the core undergoes total internal reflection at the polished surface and escapes the fiber. Energy exchange between the waveguide mode of the single mode fiber and a WGM occurs at resonance when the resonator is positioned within the range of the evanescent field of the angle-cut fiber. The angle is chosen to fulfill the phasematching requirement (Equation 3.11). Generally, the system is equivalent to a prism coupler with the focusing optics eliminated. The applicability of this technique is limited by the availability of fibers with high refractive index.

3.3.4 Fiber Taper

Tapered fiber couplers provide the most efficient coupling scheme [60–70]. Fiber taper is a single mode bare waveguide of optimized diameter (typically a few microns for the near infrared wavelength, see Figure 3.6). The taper is placed along the resonator perimeter

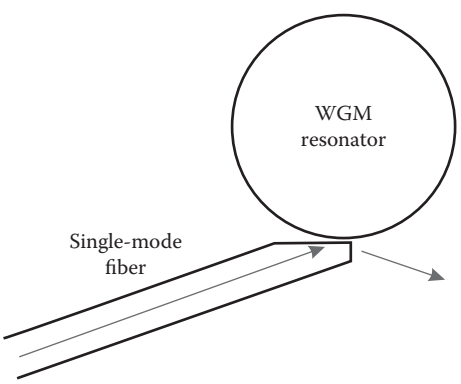

FIGURE 3.5
Angle-polished fiber coupler for WGMs.

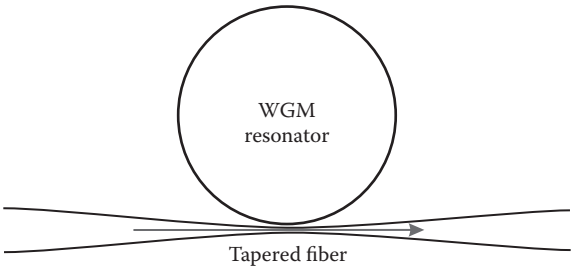

FIGURE 3.6
Tapered fiber coupler for WGMs.

allowing simple focusing and alignment of the input beam, as well as collecting the output beam. It saves the fundamental mode and filters other waveguide modes. The efficiency of tapered fiber couplers reaches 99.99% for coupling fused silica resonators [65]. Similar couplers were also used in photonic crystal resonators [66,68]. Unfortunately, fiber tapers are unsupported waveguides without cladding and are very fragile. They are only useful for resonators with refractive indices similar to silica (1.4–1.45), and cannot generally be used with higher index glass and crystalline resonators. A good coupling achieved with conventional fiber tapers, though, has been demonstrated with very small silicon resonators [71]. The coupling is possible in this case because phase matching is not very important if the size of the resonator is comparable with the wavelength.

The phase velocity depends on the taper's diameter and the refractive index. The diameter of the taper gradually decreases towards the tip, and so does the effective refractive index. By placing the resonator at a proper point of the taper, it is possible to achieve the ultimate phase matching and critical coupling. Practically speaking, this technique is limited by available fibers since the effective refractive index of the taper can be changed only between values of refractive index of the air/vacuum and the refractive index of the material the fiber is made of. When the resonator is made of lithium niobate or diamond, for example, it is not trivial to make a phase-matched taper, though the planarized silicon waveguide would likely do the trick.

3.3.5 Planar Coupling

For practical packaging of systems containing WGM resonators, the planar coupling is the most promising. Planar waveguides are generally used to couple to microring and microdisk WGM resonators [72–80]. Planar coupling to ultra-high Q crystalline WGM resonators is yet to be demonstrated.

The planar coupling technology to WGM resonators is under constant development. For example, strip-line pedestal antiresonant reflecting waveguides have been utilized for robust coupling to microsphere resonators and for microphotonic circuits [81–83]. The waveguides are highly wavelength dependent because they rely on the resonant nature of reflections from multiple dielectric layers in the cladding. A recently proposed gold-clad pedestal planar waveguide structure solves this problem and provides wide band coupling for WGM resonators [84].

An analytical method for calculation of coupling between a microdisk WGM resonator and a straight waveguide was presented elsewhere [61,85]. This problem has also been solved numerically [86,87].

3.4 Modal Structure and Spectrum Engineering

Properties of open dielectric resonators and conventional mirrored optical resonators have several significant differences. We discuss two such differences in this section. One is related to the density of the WGM spectra, and the other is related to the geometrical dispersion of the WGM resonators. Spherical WGM resonators as originally proposed are overmoded. Their spectra have a complex quasi-periodic structure with unequal mode spacings, which result from both material and geometrical dispersion.

The spectral properties of WGM resonators can be modified by changing their morphology. For example, a significant reduction in the modal spectral density is achieved in highly oblate spheroidal microresonators [88,89]. In the most extreme, but theoretically possible case, the resonator can be fabricated from a single mode fiber. Such a resonator would have only a single mode family.

The spacing of WGMs can also be modified. The problem of nonequidistant modes is rooted in the fact that radial distribution of WGMs is frequency dependent. Higher frequency modes propagate on paths that are slightly closer to the surface than those of lower frequency modes. Thus, higher frequency modes travel in trajectories of slightly larger radius and slightly longer optical path lengths. Within the current technology based on fabrication of microspherical resonators out of a uniform material, the smaller the resonator size, the more the geometrical dispersion is manifested in the unequal separation between adjacent modes. Again, a proper shaping allows fabrication of a WGM resonator with an equidistant spectrum. For example, prolate spheroidal microcavities have a nearly equidistant spectrum [90]. Fabrication of a resonator out of a single mode fiber would remove the geometrical dispersion because the paths of the modes would be restricted geometrically.

Geometrical dispersion can be mediated using properties of the refractive index of the resonator host material. The optical path length is a function of both the physical distance and the index of refraction. The dispersion can be reduced if resonators are made out of a cylindrically symmetric material whose index $n(r)$ decreases in the radial direction. With a proper choice of the gradient for the refractive index, circular trajectories corresponding to WGMs at different frequencies will have identical optical path lengths. This results in an equidistant WGM spectrum [91].

Except for the azimuthal dispersion compensation, a graded material resonator demonstrates radial dispersion compensation. This happens because modes do not encounter resonator boundaries for large refractive index gradients, but only the potential dip created due to the gradient. As a consequence, radial profiles of cavity modes are nearly symmetrical, much in the same way as with harmonic oscillator wave functions [91].

This conclusion follows from complex angular momentum theory [92], where an analogy between optics and mechanics is utilized and the resonator modes are described as eigenvalues of an effective potential U. For a WGM with index m this potential may be written as the sum of an attractive well of depth $(n^2(r)-1)k^2$ and the centrifugal potential $m(m+1)/r^2$.

The potential is asymmetric when n does not depend on radius r inside the sphere. For spheres possessing dielectric susceptibilities that increase with a decreasing radius, the shape of the potential function broadens with its apex shifting into the resonator, and its parabolic shape becoming more symmetrical; the minimum of the potential is still on the sphere surface. For some critical value of the susceptibility gradient, the potential resembles half of the oscillatory potential $U \sim (r-R)^2|_{r\to R-0}$. For gradients beyond the critical value

the minimum the potential moves into the cavity [91,93]. The deeper the minimum, the better the potential can be described by the oscillatory function.

Both methods of spectral engineering mentioned above can be applied to crystalline WGM resonators. The index of refraction of resonators can be modified by doping of the host material. This, however, is a complex task, and the modification of the resonator shape to obtain a desired WGM spectrum appears much simpler. In what follows we provide several examples of how shaping the WGM resonators changes their spectra.

3.4.1 The Spectrum and the Shape of the Resonator

A modification of the shape of a WGM resonator allows modification of its spectrum. To explain this statement let us start with the usual wave equation for a plain wave

$$\nabla\times(\nabla\times\mathbf{E})-k^2\,\varepsilon(\mathbf{r})\mathbf{E}=0, \tag{3.16}$$

where $k=\omega/c$ is the wave number, $\varepsilon(\mathbf{r})$ is the coordinate dependent dielectric susceptibility, E is the electric field of the mode, and $\mathbf{r}=(z, r, \phi)$ is the radius vector.

We assume that the resonator is axially symmetric and that its radius $R(z)$ weakly depends on z, the axis of symmetry. Using the adiabatic approximation along the z axis we present the scalar solution of Equation 3.16

$$\Psi(\mathbf{r})\sim e^{\pm i\left[\int k_z dz+m\phi\right]}\Phi\left[\frac{r}{R(z)}\right], \tag{3.17}$$

where

$$k_z^2(z)=k^2n^2-k_{m,q}^2(z), \tag{3.18}$$

n is the index of refraction of the resonator host material,

$$k_{m,q}\simeq\frac{1}{nR(z)}\left[m+\alpha_q\left(\frac{m}{2}\right)^{1/3}\right] \tag{3.19}$$

is the radial wave number defined by the equation for the radial field distribution Φ

$$\frac{\partial^2\Phi}{\partial^2 x}+\frac{1}{x}\frac{\partial\Phi}{\partial x}+\left[k_{m,q}^2-\left(\frac{m}{x}\right)^2\right]\Phi=0. \tag{3.20}$$

The light is confined along the z axis if the corresponding component of the wave vector (k_z) has two zeros, z_1 and z_2 (turning points), and is positive in the interval $z_2>z>z_1$. Then the Wentzel–Kramers–Brillouin (WKB) quantization along the z axis leads to the equation that defines the eigenvalues $k_{m,q,p}$ (see e.g. [90])

$$\int_{z_1}^{z_2}\left[k_{m,q,p}^2-k_{m,q}^2\right]^{1/2}=\pi\left[p+\frac{1}{2}\right]. \tag{3.21}$$

Such separation of variables as well as the expression for the resonator spectrum ($k_{m,q,p}$) is generally valid if [90,94]

$$k_z R \frac{dR}{dz} \ll 1, \quad z_2 > z > z_1. \tag{3.22}$$

Condition 3.22 restricts the class of resonators that can be analyzed with this technique. However, we can claim that for that class of resonators a selection of the shape of the surface *R(z)* allows modification of the resonator spectrum. For instance, it helps to evaluate the shape of a WGM resonator with an equidistant spectrum [90].

The originally proposed spherical WGM resonators are "over-moded", with a complex quasi-periodic spectrum and unequal mode spacings. A significant reduction in the mode spectral density is achieved in highly oblate spheroidal microresonator (microtorus) [88,89]. Our experiments also show that changing the shape of a millimeter-sized crystalline dielectric resonator results in the rarefication of the observed WGM spectrum without destroying the quality factor.

As an example, we have measured [95] WGM spectra of disc resonators possessing spherically (Figure 3.7a), toroidally (Figure 3.7b), and conically shaped rims (Figure 3.7c). The toroidal geometry, with its transverse curvature diameter nearly equal to the thickness of the disk, resulted in a significant rarefaction of the spectrum compared to a spherical layer (separate modes are visible in Figure 3.7b as opposed to conglomerates in Figure 3.7a). However, with this geometry it was difficult to further increase the transverse curvature to eliminate all but one WGM per free spectral range (FSR): disks smaller than 100 μm in thickness were hard to polish into the toroidal shape. As an alternative to further improving the spectral regularity, we produced a conical resonator that was subsequently polished at the rim into a very sharp bend toroid with osculating curvature diameter of ~20 μm (Figure 3.8). The spectrum proved to contain only one major mode (distinct successive peaks) (Figure 3.7c). A high Q of 5×10^7 was obtained with this resonator.

It is useful to present here an analytical expression for the spectrum of an arbitrary spheroid found in [96]

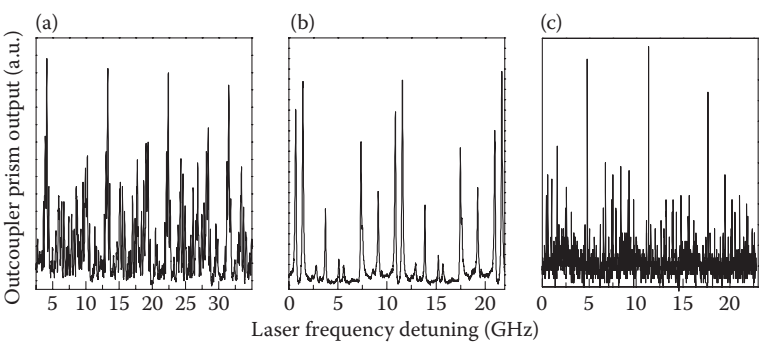

FIGURE 3.7
Spectrum of a disk $LiNbO_3$ resonator with (a) spherically shaped rim, (b) with torridally shaped rim, (c) with conically shaped rim.

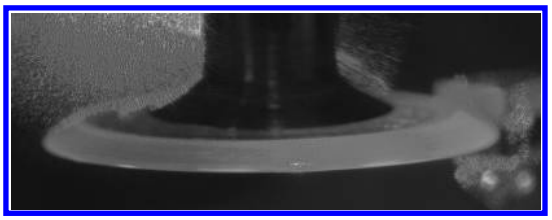

FIGURE 3.8
Conically shaped resonator spectrum of which is shown in Figure 3.7c. (From Savchenkov, A.A., Matsko, A.B. and Maleki, L., "White-light whispering gallery mode resonators", *Opt. Lett*. 31, 92–94 (2006)).

$$nk_{p,q,l}R \simeq l + \alpha_q\left(\frac{l}{2}\right)^{1/3} + \frac{2p(R-r)+R}{2r} - \frac{\chi n}{\sqrt{n^2-1}} + \frac{3\alpha_q^2}{20}\left(\frac{l}{2}\right)^{-1/3} + \frac{\alpha_q}{12}\left[\frac{2p(R^3-r^3)+R^3}{r^3} + \frac{2n\chi(2\chi^2-3n^2)}{(n^2-1)^{3/2}}\right]\left(\frac{l}{2}\right)^{-2/3}, \tag{3.23}$$

where R and r are equatorial and polar radiuses, $k_{p,q,l}$ is the wavenumber, $p=l-|m|=0,1,2,\ldots$ and $q=1, 2, 3,\ldots$ are integer mode indices, and $\chi=1$ for quasi-TE and $\chi=1/n^2$ for quasi-TM modes. The basic sequence of WGMs is given by $p=0$ and $q=1$.

Equation 3.23 does not show any actual rarefaction of the spectrum of a spheroidal resonator. It shows rather the removal of degeneracy by quantum numbers m and l. Hence, the results reported in Figure 3.7 come from the selectivity of coupling in a particular resonator, not from the real spectrum rarefaction. An additional reason for the clean spectrum of oblate spheroids is the reduction of the quality factors of the high-order modes. In what follows we discuss possible ways for obtaining real "single-mode" resonators beginning with a description of their opposite counterparts, "white light" resonators.

3.4.2 White Light Resonators

Not all applications of WGM resonators require a rare spectrum. Some applications are particularly burdened with rare and/or inhomogeneous spectra. These include coherent cavity ring-down spectroscopy [97] and electro-optical modulation with WGM resonators [98]. In the first case, narrow absorption features of a substance under study might fall between the resonator modes and would then be undetected unless the cavity modes are tunable. The spectrum also could be hard to reproduce in separate runs if the resonator is not stabilized. In the second case, the laser radiation that is modulated with a WGM-based electro-optic modulator requires a linewidth that is much narrower than the spectral width of a particular mode. The laser must also be locked to the mode of the resonator, or the resonator should be locked to the laser, which is not always feasible. A resonator with a continuum spectra, or a "white light" resonator, is extremely useful because it does not need to be locked to the laser, since there will always be modes that coincide with the laser frequency.

There are several methods for producing a continuum spectrum in a resonator and for keeping its ring-down time constant. It was suggested that a nonconfocal FP cavity would produce essentially a continuum excitation spectrum [97]. By exciting both the longitudinal and the transverse modes, one guarantees that there always are several modes at each frequency point and that light from an unstabilized narrowband laser will always be efficiently coupled into the resonator. This idea was widely used in coherent cavity ring-down spectroscopy. As another method, it was proposed to place a suitably prepared medium

in between the resonator mirrors to cancel the variation of wavelength with frequency [99,100]. This would make the resonator simultaneously resonant for all frequencies, i.e. result in "whitening" the spectrum of the resonator. Such resonators were suggested for improving the sensitivity for gravitational wave detection.

The total achievable spectral width of the existing white light resonators is restricted by the spectral characteristics of the resonator mirrors. Usually the mirrors have good reflectivity within several nanometers of a selected optical frequency.

We theoretically proposed and experimentally demonstrated essentially "white light" WGM resonators in a frequency range exceeding a full octave [101]. The basic characteristics of the resonator are (i) power build-up at virtually any frequency inside the transparency window of the material it is made of; (ii) nearly the same Q-factor (ring-down time) at any frequency in the transparency window, and (iii) nearly critical coupling with cleaved fibers at any frequency in that window. These resonators can be used in cavity ring-down spectroscopy as an alternative for FP white-light cavities. The white light WGM resonators made of photorefractive materials also can be used in electro-optical modulators.

Let us explain the basic idea of the fabrication of the white light WGM resonator. The spectrum of WGMs in a finite cylinder of radius R can be approximated by Equation 3.21. The frequency distance between modes in any selected radial mode family is characterized with the FSR divided by the ratio of the resonator thickness and wavelength. The spectrum $k_{m,q,p}$ of a thick enough WGM resonator is very dense because changing the quantum number P does not change the mode frequency significantly. The Q-factors of various modes generally do not depend on the mode numbers, so all the modes have nearly identical Qs. Hence, a thick cylindrical or a prolate toroidal resonator can be considered as a white-light cavity.

We fabricated a high-Q CaF_2 WGM resonator ($Q > 10^9$) and loaded it heavily. The resonator had 0.5 mm thickness and 0.5 cm diameter. A proper coupling technique, e.g. a cleaved fiber (seen in Figure 3.9) readily results in the excitation of majority of the modes. The coupling efficiency was better than 40% for all frequencies at which the lasers could be tuned. The resonator was tested with 1320 nm (4 kHz linewidth), 780 nm (10 kHz linewidth) lasers, and 532 nm (incoherent) light. The spectrum of the resonator is essentially

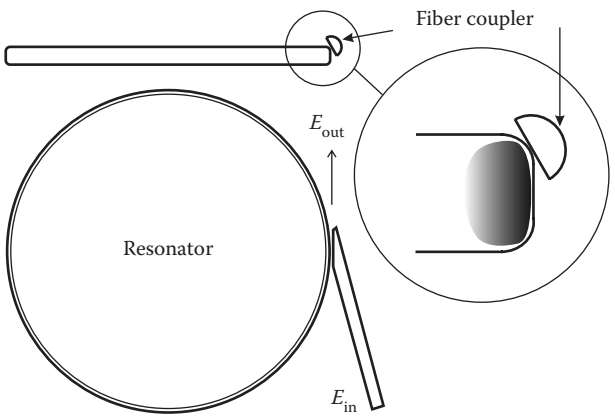

FIGURE 3.9
White light fiber coupled whispering gallery mode resonator. The resonator is thick (500 μm) which results in the coexistence of various mode families in the same geometrical volume in the vicinity of the rim of the resonator. The continuous spectrum of the resonator is achieved because the fiber coupler is slightly tilted with respect to the center of the rim of the resonator to maximize interaction with all the modes. (Reprinted from Savchenkov, A. A., Matsko, A. B., and Maleki, L., *Opt. Lett.* 31, 92–94, 2006. With permission from The Optical Society of America (OSA).)

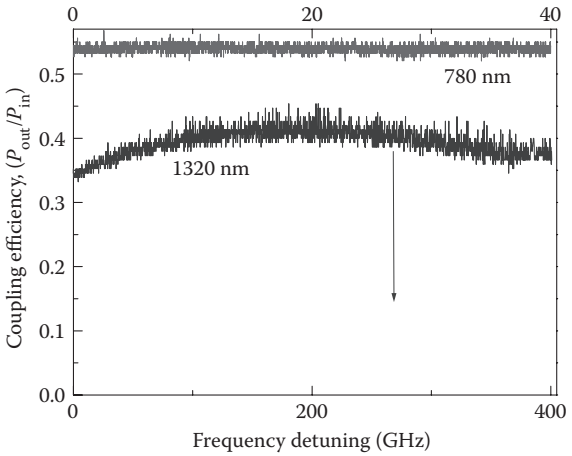

FIGURE 3.10
Spectra of the white light resonator at 1320 nm and 780 nm. Critical coupling corresponds to $P_{out}/P_{in}=0$, no coupling – to $P_{out}/P_{in}=1$. (Reprinted from Savchenkov, A. A., Matsko, A. B., and Maleki, L., *Opt. Lett.* 31, 92–94, 2006. With permission from OSA.)

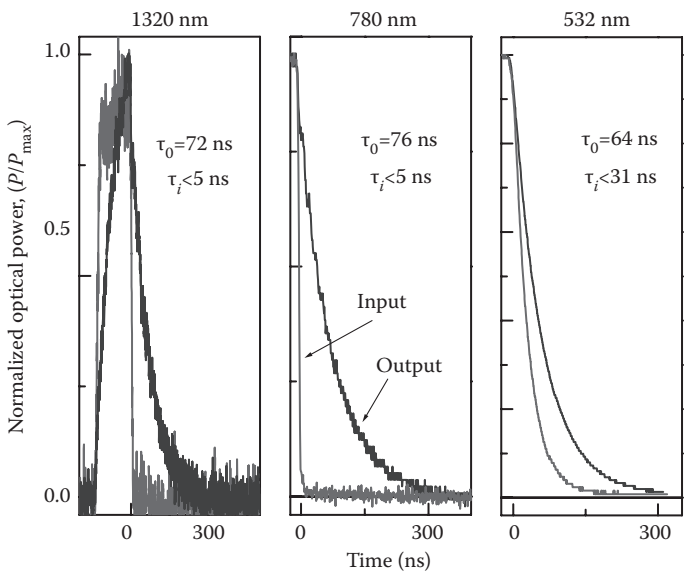

FIGURE 3.11
Normalized power of the input and output pulses of light taken at various carrier frequencies. (Reprinted from Savchenkov, A. A., Matsko, A. B., and Maleki, L., *Opt. Lett.* 31, 92–94, 2006. With permission from OSA.)

continuous if the frequency difference between modes is much smaller than their spectral width (Figure 3.10). The average distance between modes in a radial mode family was less than 20 MHz. We simultaneously excited several radial mode families.

To measure the quality factor at 1320 and 780 nm we used a ring-down technique with a $\tau_1=5$ ns shutter. For the green light we used an acousto-optic shutter with $\tau_1=31$ ns response time. Characteristic response times of the photodiode and circuits were less than 1 ns. The shape of the light pulse on the entrance and exit of the resonator are shown in Figure 3.11. The average ring-down time was $\tau_0=65$ ns, which corresponds to $Q\sim10^8$.

Variations of the Q-factor with the carrier frequency of the lasers were less than 50%. Therefore, the resonator has all the necessary "white light" properties in a frequency interval larger than an octave.

Ring-down tails in Figure 3.11 have a small amplitude modulation. The modulation results from a slight loss of orthogonality between the modes of the resonator resulting from the coupling technique, and the beating between the modes. Changing the shape of the resonator allows suppression of the beats. Mode beats also disappear if the coupling with the resonator increases (Q-factor decreases).

Let us now discuss possible applications of this white light resonator. One application is a wide bandwidth electro-optic modulator. An approach to implement coupling between light and microwave fields in a WGM resonator was recently proposed. In that study, an efficient resonant interaction of several optical WGMs and a microwave mode was achieved by engineering the shape of a microwave resonator coupled to a micro-toroidal optical cavity. Based on this interaction a new kind of electro-optic modulator (as well as photonic microwave receiver) was suggested and realized [31,98]. The modulation frequency in the modulator is determined by the FSR of the resonator.

The problem of the application is in the necessity of lasers with very narrow linewidth, much smaller than the spectral width of the WGMs in the electro-optic resonator. The laser must be locked to a selected WGM to ensure continuous modulation. Application of white-light cavities would relax those requirements, as mentioned above. As an example, let us consider two lasers with different properties used in WGM electro-optical modulators: (i) a laser with a narrow linewidth but large frequency drift and (ii) a laser with a large linewidth.

Narrow linewidth lasers interact with essentially a single WGM mode at each instant of time. The modes naturally belonging to different mode families change with time, depending on the drift of the laser. The microwave field is applied to the WGM cavity using a proper strip-line microwave resonator placed along the rim of the cavity. The microwave field couples WGMs of the same mode family, and does not couple modes from different families. For instance, if the carrier frequency of the laser light coincides with a WGM characterized with wave vector $k_{m,q,p}$, the microwave radiation can excite modes with $k_{m-m1,q,p}$ and $k_{m+m_1,q,p}$ only, where m_1 is an integer number. Those modes, irrespective of which family, are nearly equidistant and their volumes and Q-factors are nearly equal, especially if the WGM resonator is large enough. Therefore, at each instant of time the WGM resonator can be considered as being "single mode", and the modulator operates unaffected by the frequency drift of the laser. There is no need to lock the laser to a mode of the resonator.

In the second case, a laser with a large linewidth simultaneously interacts with several modes belonging to different mode families in the white-light cavity EOM. Again, the modulation process "shifts" the photons from the carrier frequency to the frequency of the sidebands based on the same mode family interaction. If the different mode families were not equidistant, or they had different Q-factors, the noise in the sidebands would increase. However since the modes have identical properties, we expect no deterioration of the modulation.

Another application of the white light WGM resonators is in cavity ring-down spectroscopy, as mentioned above. WGM resonator-based chemical and biosensors were previously proposed and widely discussed [102–115]. Measurement of the material absorption as a function of frequency is one of the ways to detect specific chemical or biological substances. If the resonator surface is covered with a layer of the material to be studied, the quality factor decreases, and the ring-down time of the resonator τ changes as

$$\tau = \tau_0 \left(1 + \frac{V_{\text{ef}}}{V_{\text{r}}} \frac{\xi}{\xi_{\text{r}}} \right)^{-1} \tag{3.24}$$

where τ_0 is the ring-down time of the resonator in vacuum, V_{ef} is the effective volume in the added substance, V_r is the volume of the mode in the resonator, ξ is linear absorption per round trip of the material under study, and ξ_r is absorption of the material of the resonator per round trip. We neglected scattering in this expression.

White light WGM resonators, in the same way as white light FP resonators, can be useful for spectroscopy purposes. White light resonators allow tuning the laser interacting with the resonator instead of tuning the resonator, which can significantly simplify the experiments and the requirements for the laser characteristics could also be relaxed.

3.4.3 Single-Mode Resonators

Many practical applications of WGM resonators require their spectrum to be sparse, originating from a single mode family, and uncontaminated by the presence of other modes. The spectrum of a nonideal microsphere, the most common WGM resonator, is usually dense and special techniques are devised to clean it up [116]. Changing the resonator shape can reduce the density of high-Q modes which are effectively excited by the chosen coupler. Nearly single-mode operation of a microdisc WGM resonator was demonstrated in such a way (see the discussion at the beginning of this section and [88,89]).

Two general approaches exist for engineering optical modes. The most common approach is to use optical waveguides to confine and guide light. The waveguide is based on the refractive index contrast between its material and the surroundings to support light confinement and guiding. In the other approach, a photonic band-gap crystal provides confinement and guiding of photons using the morphology of the structure. This is achieved by placing defects in otherwise periodic arrays of a dielectric material. We have recently proposed a new approach that relies on generating an effective refractive index contrast produced by shaping the geometry of a WGM resonator [38,53]. With this technique single and multiply coupled WGM resonators can be designed for a wide variety of applications. We have found recently that a similar technique was proposed to clean the spectrum of FP resonators [117].

The utility of WGM-based devices and the efficiency of nonlinear optical interactions of WGMs depend on accurate engineering of the cavity mode structure. Specifically, this means producing cavities with extremely rarified (single-mode-family) spectra. Achieving the required level of control over the mode spectrum has eluded scientists working on WGM resonators. Thus, WGM resonators have as yet neither entered the mainstream of photonic device engineering nor have they been embraced by the mainstream of optical physics.

Researchers working on optical waveguides faced a similar set of problems in designing the single mode fiber. Single mode fiber has revolutionized the world of optics by enabling long-distance telecommunications and multichannel television broadcast systems, functions that would be impossible with multimode fibers. This is because the single mode fiber can retain the fidelity of a light signal over long distances. It exhibits no dispersion due to multiple modes and is characterized by lower attenuation than a multimode fiber.

A homogeneous dielectric waveguide becomes single-mode when the frequency of the propagating light is close to its cut-off frequency. This means that the thickness of the waveguide approaches the half-wavelength of light in the host material of the waveguide. It is impractical to fabricate a single-mode optical fiber by decreasing the fiber diameter. Instead, the single mode operation is ensured by the specially selected radial profile

of the refractive index of the fiber material. The core of the fiber has a larger index of refraction than the cladding material that surrounds it. The difference of the indices is small, so only one mode propagates inside the core, while the others decay into the cladding (Figure 3.12A). For instance, the condition for the single mode operation of a planar waveguide is [118]

$$d_{co} < \frac{\lambda}{2\sqrt{\Delta\varepsilon}}, \tag{3.25}$$

where d_{co} is thickness of the core, λ is wavelength of light in vacuum, and $\Delta\varepsilon$ is the difference between the susceptibilities of the core and the cladding material, respectively. As a result, the core may have a reasonably large diameter. Note that the core of a single-mode fiber is a multi-mode fiber if the cladding is removed.

Let us consider the WGM resonator as a multi-mode gradient waveguide (Figure 3.12B) [119]. The resonator becomes an ideal single-mode-family resonator only if the waveguide is thin enough. Following this trivial approach the WGM resonator should be designed as an approximately half-wavelength-thick torus to support a single mode family. Recent experiments confirmed this conclusion and nearly single-mode resonators have been demonstrated [89].

There is another, nontrivial, approach to the problem based on the analogy with single-mode optical fiber. A WGM resonator made of any transparent material with any size can be transformed into a single-mode resonator if the appropriate geometrically defined "core and cladding" are developed (Figure 3.12C).

To show that WGM modes can be described using a waveguide formalism, we start with the usual wave equation (Equation 3.16). Higher-order WGMs (i.e. those with the wavelength much smaller than the resonator size) of both TE and TM modes are localized in

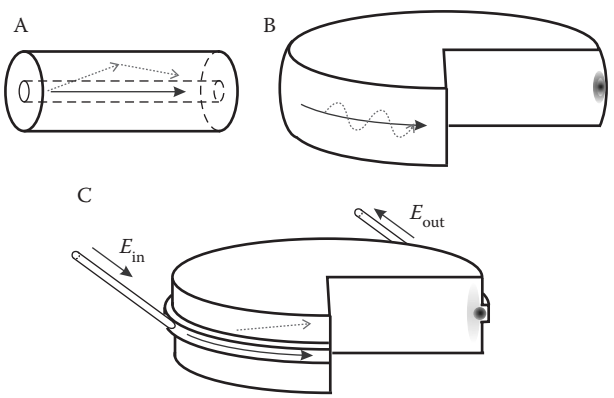

FIGURE 3.12
(A) A structure and mode localization in the optical fiber. Only one propagating mode, shown by the solid line, survives in the core of the fiber, while others (dotted line) penetrate into the cladding and dissipate. (B) Mode localization in the whispering gallery mode resonator. The resonator corresponds to a multimode gradient fiber where the index of refraction is set by the resonator shape, not by the change of the refractive index of the resonator host material, which is constant. Both the fundamental and auxiliary modes survive. (C) Mode localization in a low-contrast whispering gallery mode resonator. Only a single-mode family survives. The other modes penetrate into the cylinder rod and dissipate. The coupling to the single mode family is achieved with, e.g. a cleaved fiber coupler. (Reprinted from Savchenkov, A., Grudinin, I. S., Matsko, A. B., Strekalov, D., Mohageg, M., Ilchenko, V. S., and Maleki, L., *Opt. Lett*. 31, 1313–1315, 2006. With permission from OSA.)

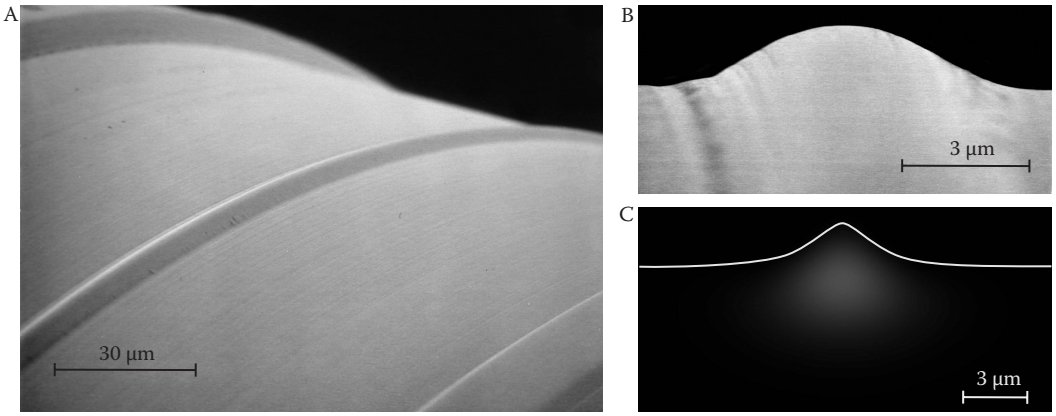

FIGURE 3.13
(A) Scanning electron microscope image of the resonator whose spectrum is shown in Figure 3.14. The resonator has nearly Gaussian shape with 2.5 μm height and 5 μm full width at the half maximum. (B) The image of the profile of the resonator shown in (A). (C) Intensity map of the field in the resonator shown in (A) simulated by numerical solution of Equation 3.26. (Reprinted from Savchenkov, A., Grudinin, I. S., Matsko, A. B., Strekalov, D., Mohageg, M., Ilchenko, V. S., and Maleki, L., *Opt. Lett*. 31, 1313–1315, 2006. With permission from OSA.)

the vicinity of the equator of the resonator. For this problem, cylindrical coordinates can be conveniently used. Applying the technique of separation of variables, and assuming that the resonator radius changes as $R=R_0+L(z)$ ($R_0 \gg |L(z)|$) in the vicinity of the equator, we transform Equation 3.16, for TE mode family, to

$$\frac{\partial^2 E}{\partial r^2}+\frac{\partial^2 E}{\partial z^2}+\left[k^2\varepsilon\left(1+2\frac{L(z)}{R_0}\right)-\frac{m^2}{r^2}\right]E=0, \tag{3.26}$$

where m is the angular momentum number of the mode (we assumed that $m \gg 1$), $E(r,z)$ is the scalar field amplitude, ε is the susceptibility of the resonator host material. This equation is similar to the gradient waveguide equation. It is easy to see that, for instance, modes of a spherical WGM resonator coincide with modes of a gradient waveguide with parabolic distribution of refractive index in the z direction. Hence, it is the geometry of the surface that should be modified to produce an ideal single-mode WGM resonator. A "core" for the WGM "waveguide" can be realized by the proper design of the resonator surface in the vicinity of the equator. The rest of the resonator body plays the role of the "cladding" (Figure 3.1C).

Consider a resonator consisting of a cylindrical drum and a small, ring like protrusion, $L(z)=L_0$ for $d \geq z \geq 0$, on its surface. The drum's effective susceptibility does not depend on the z coordinate and is equal to ε. The effective susceptibility of the ring, $\varepsilon(1+2L_0/R_0)$ (see Equation 3.26), is slightly larger. Therefore, the ring is the core that confines the light in the z direction, while the drum is the cladding. The condition for "single mode" operation of the resonator using Equation 3.25 is:

$$1>\frac{d}{\lambda}\sqrt{\frac{2L_0\varepsilon}{R_0}}>\frac{1}{2}. \tag{3.27}$$

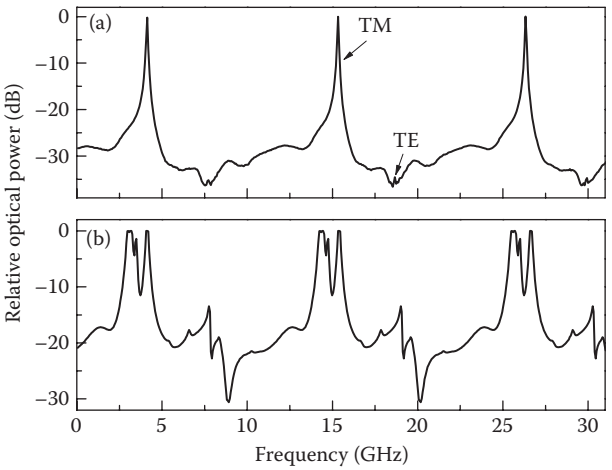

FIGURE 3.14
(A) The spectrum of a nearly ideal single-mode resonator obtained using a 980 nm laser as well as the cleaved fiber couplers (Figure 3.12C). The mode number is approximately $m=3\times10^4$. The low-Q modes on the spectrum background belongs to the drum. (B) The spectrum of the multimode resonator made on the same drum (2.5 μm height and 15 μm width) and detected using the same coupling technique. The resonator is partially visible in the lower right corner of Figure 3.13A. (Reprinted from Savchenkov, A., Grudinin, I. S., Matsko, A. B., Strekalov, D., Mohageg, M., Ilchenko, V. S., and Maleki, L., *Opt. Lett*. 31, 1313–1315, 2006. With permission from OSA.)

This condition (Equation 3.27) stays valid for a resonator with an arbitrary large radius. Both the width and the height of the ring can be much larger than the wavelength of light. The ratio L_0/R_0 plays the same role as the ratio $\Delta\epsilon/\epsilon$ in an optical fiber.

To demonstrate the single-mode operation experimentally, we built such a resonator by using a two-step fabrication process that is described in one of the previous sections of this chapter. We fabricated a CaF_2 rod of 5 mm in diameter. WGMs in such a rod have extremely dense spectra. After that we fabricated a small ring with dimensions of the order of several microns on the surface (Figure 3.2).

We used an angle-polished fibers to couple light into the resonator. The spectrum shown was obtained with two angle-polished fiber couplers, one for the input and one for the output. The fiber couplers were made with standard single mode fiber with cladding diameter of about 150 μm and core of about 5 μm. The photodetector signal represents transmission of the resonator. The two families of modes shifted by a few GHz were observed, one for each polarization. One of such families is shown in Figure 3.14A. Logarithmic detector measurements have shown that there were no other modes down to –30 dB level, only the two mode families. It should be noted that, given the geometrical parameters of the resonator and the couplers, the single mode regime of this resonator is not a function of coupling but an intrinsic property. Moreover, the logarithmic measurements were performed in a loaded configuration, that is, when the couplers are in contact with the resonator. We also confirmed that this was a single-mode resonator by performing numerical simulation of its parameters which clearly demonstrated that only the fundamental modes survive. Intrinsic Q factors of both families of modes shown in Figure 3.14A are on the order of 10^7 (loaded Q is 2×10^6, Figure 3.15). The particular resonator's Q-factor was limited by residual surface roughness.

With this approach, one can make a single-mode optical WGM resonator of any size. A resonator the size of an apple requires a ring with dimension of tens of microns for single

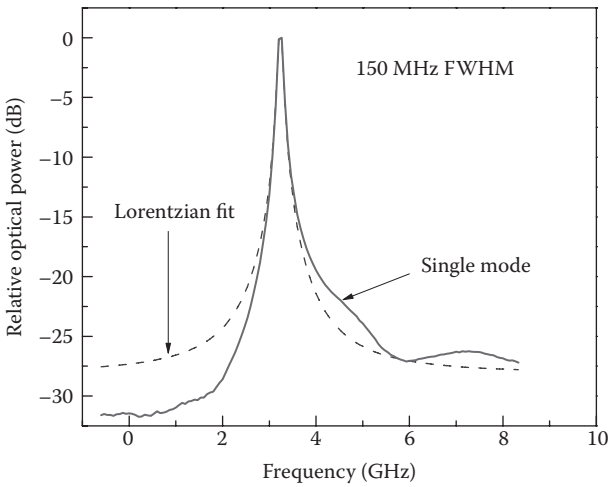

FIGURE 3.15
A Lorentzian fit of a WGM spectrum of which is shown in Figure 3.14A.

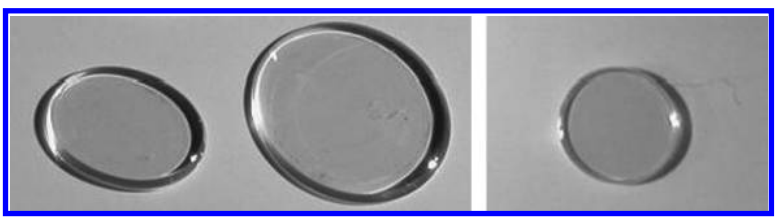

FIGURE 3.16
Elliptical $LiNbO_3$ resonators. (Reprinted from Mohageg, M., Savchenkov, A., and Maleki, L. *Opt. Express*. 15, 4869–4875, 2007. With permission from OSA.)

mode propagation of one micron wavelength light. This is counter-intuitive because the size of the single-mode channel is much larger than the wavelength. This type of experiment may be interesting as a fundamental research investigation. For practical applications small resonators are of more interest. In this context, our approach leads to a novel means for engineering of microcavity spectra.

The type of the dielectric media used for the proposed resonators is not important, as long as it is solid and transparent. Generally, since the behavior of the system is defined only by its geometry, it is not even important for what kind of waves the structures is a resonator. Microwave, acoustical or mechanical chains of resonators of this type have the same features and basis of design as these optical counterparts.

3.4.4 Elliptical Resonators

Mechanical fabrication that allows engineering the shape of the rim of a toroidal resonator, also enables producing elliptical and other kinds of geometrically shaped symmetric resonators. These resonators can retain high-Q WGMs, and also can possess unstable low-Q modes. Elliptical high-Q lithium niobate WGM resonators (see Figure 3.16) were studied elsewhere [52]. It was shown that the elliptical geometry of the resonator rim simplifies the coupling procedure. Coupling efficiency exceeding 97% was demonstrated.

Unlike modes in race track resonators, WGMs in elliptical resonators are stable. Their approximate spectrum can be found by means of the eikonal method [52]. Assuming a closed resonator we find for the high-order modes

$$2knRE(1,\varepsilon)=\pi m, \tag{3.28}$$

where $E(1,\varepsilon)$ is the complete elliptic integral of the second kind. Equation 3.28 has two parameters that define the geometry of the ellipse: eccentricity ε and semimajor axis length R.

Obtaining a rigorous expression for the modal spectra of elliptical resonators is rather involved. The determination of WGM spectrum in a spherical resonator is an easy task because the Helmholtz equation can be solved exactly by separation of variables. This is not the case for an elliptical resonator. A detailed mathematical analysis of the WGMs in elliptical resonators with large size compared to the resonant wavelength can be found in [121,122]. Waveguide coupling to elliptical WGM resonators were studied numerically [123]. It is worth noting that laser emission from ellipsoidal resonators was studied experimentally [124].

The fabrication procedure of the crystalline elliptical resonators is straightforward. A piece of crystal in the shape of a baseball diamond was cut from a Z-cut wafer of congruent $LiNbO_3$. The lengths of the axes of the diamond were selected to be slightly larger than the target dimensions of the desired ellipse. The edges of this structure were mechanically ground until the sharp edges of the diamond shape were smooth in a continuous curve resembling an ellipse. At this point, mechanical polishing techniques were applied to shape the edge curvature and polish the edge surfaces.

Three optical resonant cavities of elliptical cross section are shown in Figure 3.16. The eccentricity of the first cavity is 0.57. The lengths of the semimajor and semiminor axes are 4.4 and 3.6 mm, respectively. The second cavity has an eccentricity of 0.71, with semimajor and semiminor axis lengths of 4.6 and 6.5 mm, respectively. The thickness of both resonators is 0.5 mm. The third cavity has an eccentricity of 0.32, with semimajor and semiminor axis lengths of 3.4 and 3.6 mm, respectively.

Design of the resonator geometries is impacted by the coupling mechanism. Evanescent coupling of light into dielectric resonators requires phase matching between the wavenumber in the coupling medium and the wavenumber of the resonant mode. As is shown above, it means that the refractive index of the coupling medium should be larger than the refractive index of the resonator host material to couple to WGMs. Further, the coupling material should have a comparable optical transparency window to that of the host material to avoid additional round trip losses.

$LiNbO_3$ is a birefringent dielectric, and the coupling conditions for TE and TM modes in this material are slightly different. For example, to couple to TE modes of the resonator, the free space beam should have an incidence angle of 22° with respect to the plane tangent to the prism–resonator interface. A circular symmetric beam entering the prism at this angle will be elliptical in cross section at the interface plane. For TE modes, the spot size along the polar axis of the resonator is larger than the spot size measured along the azimuthal axis of the resonator by a factor of 2.7. There will be a drop in the overall coupling efficiency when the ratio achieved during fabrication is not equal to this value.

The ratio is fixed for resonators with circular symmetry, and is subject to the precision of the fabrication apparatus, knowledge of the refractive indices of the resonator and coupler materials, and knowledge of the wavelength of light being used. Realization of a critical curvature ratio at some point along the perimeter of the resonator is more probable for an

elliptical resonator. The curvature ratio varies along the perimeter as the radius of curvature changes in those resonators.

Experiments with elliptical lithium niobate resonators were performed with 1550 nm light evanescently coupled to the resonators by means of a diamond prism [52]. The laser light was scanned over several FSRs of the resonators. Light reflected from the cavity-prism interface was collected by a 3 mm diameter light pipe and sent to an InGaAs photodetector. One of the assumptions of the approximation used to model WGMs in elliptical resonators is that the modes of the same modal indices travel the same optical path regardless of the input positions. That is, the FSR of the resonator is constant as the input position is varied. The position of the incident beam, governed by the location of the diamond prism along the cavity perimeter was varied between semimajor axes in 30° steps. It was found that throughout the various input angles, the same frequencies of light are resonant with the cavity and the same FSR was observed [52]. This observation confirms the theoretical assumption.

The FWHM of the mode was measured, and the value was used to calculate the Q-factor of this mode, yielding 1.5×10^8, which corresponds to the highest quality factor measured with congruent lithium niobate resonators (see next section). The measured FSR agrees well with the calculated values from Equation 3.28.

A coupling efficiency of 97.3% into the third resonator (Figure 3.16) was achieved. It was found that the coupling efficiency varied when the contact position between the prism and resonator was changed. The coupling efficiency refers to the fraction of light transmitted from within the coupling medium to a specific resonator mode and out through an output path symmetric with the input path. Light that couples from the mode to a different output channel, i.e. another WGM, is accounted for as additional loss. Fresnel losses at the air–prism interface are also present in the system. They could be mitigated by an appropriate antireflection coating of the prism. Taking Fresnel losses and loss associated with instrumentation into account we found that the best laser-to-detector transmission efficiency through the resonator remains in excess of 91%.

3.5 Quality Factor and Finesse of Crystalline Resonators

In this section, we discuss achievable values for quality factors that can be realized in crystalline WGM resonators [34]. Resonators are usually characterized with two partially dependent parameters—finesse (F) and quality factor (Q). The finesse of an empty FP resonator is defined solely by the reflectivity of its mirrors and is calculated as $F=\pi\sqrt{R}/(1-R)$. The maximum reported value of reflectivity $R\simeq 1-1.6\times10^{-6}$ is achieved with dielectric mirrors [125,126]. A FP resonator made with these mirrors has finesse $F=1.9\times10^6$. Further practical increase of the finesse of FP resonators is problematic because of the absorption and scattering of light in the mirror material [127,128], though the fundamental limit on the reflection losses given by the internal material losses and by thermodynamic density fluctuations is of the order of parts in 10^9 [127]. The quality factor of a resonator depends both on its finesse and its geometrical size. The one-dimensional FP resonator has $Q=2FL/\lambda$, where L is the distance between the mirrors, and λ is the wavelength. It is easy to see that the quality factor of the resonator is essentially unlimited because L is unlimited.

Finesse and Q are typically equally important in the majority of applications. In some cases, though, finesse is technically more valuable than the quality factor. For instance, the

buildup of optical power inside the resonator and the Purcell factor [129] are proportional to finesse. Sometimes quality factor is more important. For example, the inverse threshold power of intracavity hyperparametric oscillation is proportional to Q^2 [130], and efficiency of parametric frequency mixing is proportional to Q^3 [131]. Therefore, it is important to know both the maximally achievable finesse and quality factor values of a resonator.

The knowledge of the resonator quality factor is important for the applications in material science. Not much data is available for the optical absorption coefficients, since there is no technique capable of measuring this coefficient with high precision when absorption becomes very weak. Interestingly, the WGM resonators may be used to measure internal absorption with good precision if the Q factor is only limited by the internal absorption. For example, the absorption coefficient reported by CaF_2 crystal producer is 2×10^{-5} cm^{-1}. According to the expression for the internal absorption limited Q factor, this corresponds to $Q=4.2\times10^9$ at wavelength of 1064 nm. On the other hand, with this piece of crystal we have measured $Q=5.3\times10^{10}$, which gives a more accurate upper estimate for the absorption coefficient 1.6×10^{-6} cm^{-1}.

WGM resonators can have larger finesse compared with FP resonators. For instance, fused silica resonators with finesse 2.3×10^6 [132] and 2.8×10^6 [133] have been demonstrated. Crystalline WGM resonators reveal even larger finesse values, $F=6.3\times10^6$ [134], because of low attenuation of light in the transparent optical crystals. The large values of F and Q result in the enhancement of various nonlinear processes. Low threshold Raman lasing [135,136], opto-mechanical oscillations [137], frequency doubling [131], and hyperparametric oscillations [138,139] based on these resonators have been recently demonstrated. Theory predicts the possibility of achieving nearly 10^{14} for Q-factors of optical crystalline WGM resonators at room temperature [131,134], which correspond to a finesse level higher than 10^9.

Experiments, thus far, have shown numbers that are a thousand times lower. The difference between the theoretical prediction and the experimental values is due to material imperfections. To bridge this gap, a technique to substantially reduce the optical losses caused by the imperfections was developed [34]. A specific multi-step asymptotic process was utilized for removing imperfections in the host material of the resonator. This technique was previously used to reduce microwave absorption in dielectric resonators [24]. One step of the process consists of mechanical polishing performed after high temperature annealing. Several repeated subsequent steps lead to a significant reduction of the optical attenuation and, as a result, the increase of Q-factor and finesse of the resonator. With this approach we demonstrated a CaF_2 WGM resonator with $F>10^7$ and $Q>10^{11}$.

There are several practical issues related to the study of properties of ultra-high-Q resonators. The study is challenging because the spectral width of the corresponding WGM is expected to be less than a kHz. Direct observation of such a narrow line could be done with a narrowband tunable laser with a high level of frequency stability. Such lasers are not available in many laboratories. Another problem is related to the parasitic contributions from nonlinear effects. Because the threshold of stimulated Raman scattering (SRS) is very low in high-Q resonators [136] the direct observation of the intrinsic spectral width of a WGM with a continuous wave laser radiation is a problem. Thermal oscillations and drifts of the position of the optical resonance also make a time-averaged observation problematic.

A nonlinear ring-down technique that was recently demonstrated [140] helps avoiding these limitations. In this approach, the laser frequency is swept rapidly across the resonance line. A part of the light is accumulated in the mode during the sweep and is reemitted in the direction of the detector. The reemitted radiation interferes with the laser light,

and beatnote signals can subsequently be observed. The power of the laser light is generally much larger than the power of the reemitted light. Hence, the envelope of the decaying oscillations follows the decay of the amplitude of the reemitted light. This decay is twice as long as the intensity decay. The optical Q-factor of the cavity is expressed as $Q=\omega\tau/2$.

We selected a fluorite WGM resonator with optical loss limited by the material attenuation, not by the surface scattering [141]. The resonator was 4.5 mm in diameter, had 0.5 mm in thickness, and 32 μm in diameter of sidewall curvature. The resonator was placed into the center of a 3-feet long air-filled transparent tube made of annealed fused silica. The tube was installed into a 20 cm long horizontal tube furnace. The heated furnace core had approximately one inch in diameter and three inches in length. We increased the temperature of the furnace core from room temperature to 650°C during a 3 hour period, and kept the temperature stabilized for 1 day. The core was then cooled back during 3 hours, and the fluorite resonator was subsequently repolished. We repeated this process three times keeping the same annealing duration but gradually decreasing the size of the grain of the diamond slurry used for polishing. This approach resulted in a significant increase of the ringdown time at the end of the process.

The measured ringdown spectrum did not change substantially after the first annealing stage. However, the ringdown time increased significantly after the third stage. The measured ringdown signals are shown in Figure 3.17. A five-fold increase of the optical ringdown time is clearly observed. It is also worth noting that the measured quality factor is several times larger when compared with the quality factor of calcium fluoride resonators observed previously at 1.55 μm (see [134,141]).

The power in the mode of the annealed resonator was clearly above the threshold of the nonlinear loss related to SRS [140]. The measurement method used in the experiment has a low dynamic range, so it was not possible to observe the nonlinear decay with the high-amplitude signals. For that reason the ringdown time was measured using a smaller optical power. In such a measurement two major precautions must be taken: (i) the laser wavelength must interact with only one mode, which means that no WGM doublets are

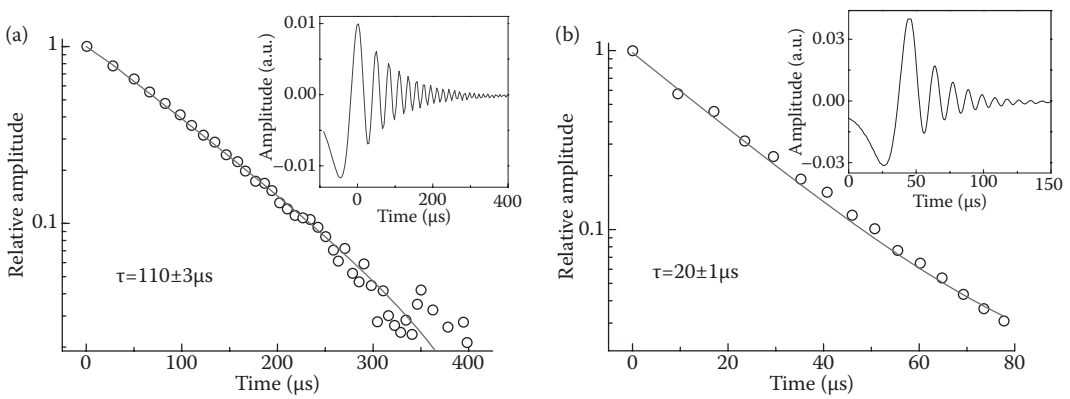

FIGURE 3.17
(a) Ring-down signal after one annealing step. (b) Ring-down signal after three annealing steps. The exponential fit (solid curve) is nonlinear in the logarithmic scale because the exponents have constant offsets. Keeping in mind that $Q=\omega\tau/2$, and $\omega=2\pi c/\lambda$, $\lambda=1.55\mu m$, we find that the values of the quality factors after the first and third annealing steps are $Q=1.2\times10^{10}$ and $Q=6.7\times10^{10}$, respectively. It is important to note that the initial value of the Q-factor corresponds to the earlier observations [134], while the final value is the apparent improvement at the given wavelength. (Reprinted from Savchenkov, A. A., Matsko, A. B., Ilchenko, V. S., and Maleki, L., *Opt. Express* 15, 6768–6773, 2007. With permission from OSA.)

allowed within the investigated frequency span. (ii) the sweep of the frequency of the laser must be controlled and the local frequency of the beatnote signal must never increase; such an increase can occur if the laser is swept back to the starting frequency rapidly. In this way the single excitation of a single WGM is ensured.

The best ringdown signal measured with all the precautions is shown in Figure 3.18, left. The oscillation period of the beatnote was evaluated in order to ensure that the measured line is not a result of several consecutive excitations of the optical mode caused by dithering of the laser frequency (Figure 3.18, right). This shows that the carrier frequency indeed moves gradually from the resonance and the WGM is not excited twice.

Let us discuss the fitting procedure to the theoretical curve in more detail. The positions of the maxima and minima of the beatnote peaks, as well as the zero crossings of the beatnote signal, were identified for the evaluation of the oscillator period. The time coordinate of each peak was subtracted from the coordinate of the adjacent peak and the averaged time for the two adjacent peaks was obtained. The same procedure was repeated for the zero-crossing points. In this way the time dependence of the period of the beat note signal, shown in Figure 3.18 right, was deduced. The dependence is linear at the tail of the curve. The initial period has a different time dependence because the frequency of the WGM changes much faster immediately after the frequency of the pump laser is tuned away from the WGM. The change is determined by multiple nonlinear processes, e.g. WGM frequency shift due to after-interaction cooling of the resonator.

Using linear approximation for the beatnote period we found the period of the waveform to fit the experimental data. We solved the equation $\phi(t+\text{Period}(t)/2)-\phi(t)=\pi$ approximating it by a linear differential equation $\dot{\phi}(t)=2\pi/\text{Period}(t)$. Using the experimental results the $\text{Period}(t)=\xi-\zeta t$ is obtained, where $\xi=71.1$ μs, and $\zeta=0.11$ (time t is measured in microseconds). As a result, the expression

$$\phi(t)=\text{Const}-(2\pi/\zeta)\ln(1-\zeta t/\xi) \tag{3.29}$$

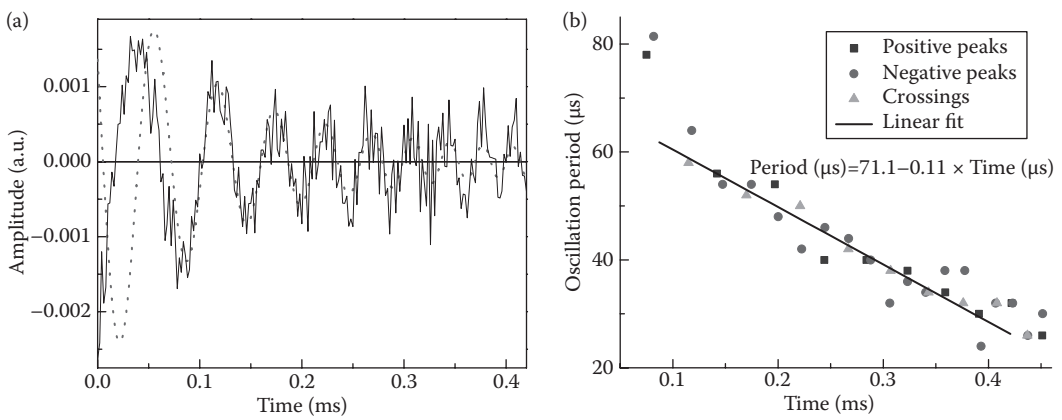

FIGURE 3.18
(a) Ringdown signal after the third annealing step taken with low-power laser radiation (solid line). The theoretical fit of the signal is shown by the dotted line. (b): Evaluated change of the period of the signal. The solid line stands for the linear fit of the time dependence of the period of the ringdown signal. (Reprinted from Savchenkov, A. A., Matsko, A. B., Ilchenko, V. S., and Maleki, L., *Opt. Express* 15, 6768–6773, 2007. With permission from OSA.)

follows for the phase. The final oscillation waveform presented in Figure 3.18, right is given by $\cos[\phi(t)]$.

The time dependence of the beatnote amplitude was extracted in the following way. The amplitude of a minimum of the oscillating beatnote signal was subtracted from the adjacent maximum. The value shows the relative oscillation amplitude. This value was related to the moment of time equally separated from the maximum and the minimum time coordinates. The result of the evaluation is shown in Figure 3.19. Using the first three points of the dependence the initial decay time $\tau_1 = 130$ μs was found. Using the part of the signal in the interval between 0.15 and 0.35 ms the final decay time, $\tau_2 = 510$ μs was found. Finally, we used the expression for the nonlinear decay rate discussed by Matsko et al. [142] to fit the amplitude decay rate. The resultant fit of the beatnote waveform is shown in Figure 3.18, left. In this way, we can conclude that the intrinsic linear quality factor of the CaF_2 WGM resonator approaches 3×10^{11} at 1.55 μm (20-fold improvement compared with the initial quality factor).

Let us calculate the finesse of such a resonator. The expression for the finesse, as well as the quality factor, of WGM resonators naturally includes index of refraction of the resonator host material, unlike the case of an empty FP resonator: $Q = 2\pi a F n_0/\lambda$, and $F = c/[2an_0(\gamma_0 + \gamma_c)]$. Here a is the radius of the resonator, n_0 is the index of refraction of the resonator host material, γ_0 and γ_c are the intrinsic and coupling amplitude decay rates, respectively. The values of light intensity inside I_{in} and outside I_0 the resonator are related as $I_{in}/I_0 = 2\gamma_c F/[\pi(\gamma_0 + \gamma_c)]$. Using the experimental data ($2a = 0.45$ cm, $n_0 = 1.42$) the finesse of the resonator is found to be $F = (2.1 \pm 0.6)\times10^7$.

The annealing process discussed above improves the transparency of the material because an increased temperature results in the enhancement of the mobility of defects induced by the fabrication process, and also reduces any residual stress birefringence [143]. The increased mobility leads to the recombination of defects and their migration to the surface [24]. It is worth noting that this annealing technique is similar to the previously developed procedures [144,145].

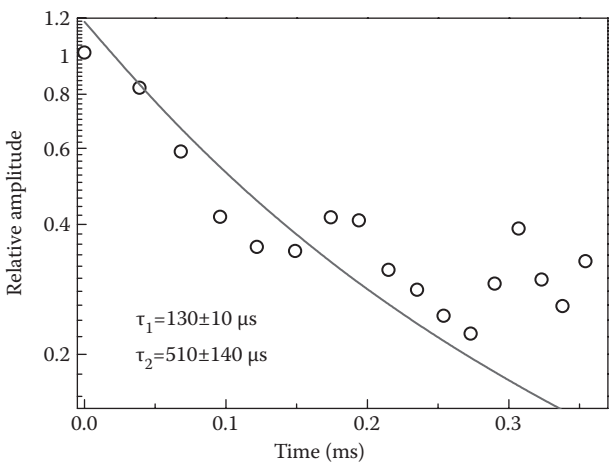

FIGURE 3.19
Change of the signal amplitude shown in Figure 3.18 left, with time. Initial and final quality factors are $Q = (7.9 \pm 0.5)\times10^{10}$ and $Q = (3 \pm 1)\times10^{11}$, respectively. Solid line stands for the theoretical fit of the ringdown signal found using formalism presented by Matsko et al. [142]. A small oscillation of the decaying signal may result from the residual scattering in the material becoming observable at the given value of quality factor.

The significant improvement of the Q-factor and finesse of a fluorite WGM resonator discussed above does not reach the fundamental limit. The straightforward annealing of a WGM resonator leads to $Q > 10^{11}$ at 1.55 μm while our earlier theoretical prediction gives $Q \simeq 10^{13}$ at this wavelength [141]. To improve the quality of annealing we suggest using a larger furnace with much lower thermal gradients. Thermal gradients within a sample play the leading role in the defect redistribution [143]. The amplitude of the gradient can be reduced not only by increasing the volume of the oven but also by increasing the thermal conductivity and optimizing the shape of the container the resonator is placed into during the annealing procedure. A fluorite container is the best choice for annealing fluorite WGM resonators.

In this section, we demonstrated that a proper thermal annealing procedure combined with mechanical polishing allows producing WGM resonators with vastly improved finesse and quality factors. We expect that the technique described here will help to improve quality factors and finesses of WGM resonators made of other transparent crystalline materials.

3.5.1 Fundamental Limits

Mechanical polishing techniques discussed above significantly suppress surface scattering and surface absorption as loss mechanisms [38] in crystalline resonators. The linear and nonlinear attenuation in the crystalline dielectric material is the remaining physical mechanisms limiting the ultimate achievable Q. We discuss such a fundamental attenuation in this section [146].

Optical transparency of ideal dielectric crystals is restricted by the fundamental blue and red wings of single photon absorption. The blue wing is defined by optically allowed transitions between valence and conduction electron bands. The red wing results from the interaction between light and phonons in the crystalline medium. Both absorption mechanisms have a strong frequency dependence, so the absorption of a dielectric within the transparency band can be extremely low. The question is how low the attenuation could be in reality, and is there any other mechanism that restricts the transparency of dielectrics. The question regarding the minimum attenuation of light propagating in a solid dielectric has been discussed for optical fibers by Lines [147]. It was shown that the scattering loss mechanisms such as Rayleigh, Brillouin and Raman scattering determine the extent of optical attenuation. These mechanisms also present in ideal optical crystals and limit their transparency.

We have analyzed [146] the minimum light attenuation achievable with ideal crystals at room and cryogenic temperatures. We used a real, nearly perfect, fluorite crystal as an example. It was shown previously that at room temperature the attenuation of UV light in artificially grown CaF_2 is nearly completely limited by Brillouin and thermodynamic Rayleigh scattering [148]. We have shown that the spontaneous Raman scattering is primarily responsible for attenuation in an ideal crystal at low temperatures. Applying this result to the crystalline WGM resonators we have found the limits to the quality factor. We also have shown that, in contrast to the low temperature regime, spontaneous Brillouin scattering as well as SRS determine the Q factor of a WGM resonator under realistic experimental conditions at room temperature. We have measured the influence of SRS on the Q factor of a millimeter-sized resonator using a ring-down technique and shown that this scattering becomes important at input power levels as low as a few microwatt.

Let us consider Rayleigh, Brillouin and Raman scattering in a perfect crystal. Thermodynamically limited Rayleigh scattering is small in an ideal crystal, and Brillouin

scattering dominates. The quantitative ratio of Rayleigh and Brillouin scattering can be estimated using the Landau–Plachek relationship (see e.g. [149]):

$$\frac{\alpha_{Ri}}{\alpha_B} \simeq \frac{\beta_T}{\beta_S} - 1 \tag{3.30}$$

where β_T and β_s are the isothermal and isobaric compressibilities, respectively. This ratio is generally less than unity in crystals and is proportional to temperature in the low temperature limit [150]

$$\frac{\beta_T}{\beta_S} - 1 = \frac{C_P}{C_V} - 1 \sim T^4\Big|_{T\to 0}, \tag{3.31}$$

where C_p and C_v are the specific heat capacities at constant pressure and constant volume, respectively. Rayleigh scattering can be neglected in a perfect crystal at low temperature, as a result of Equation 3.31).

Temperature dependence of spontaneous Raman and Brillouin scattering mechanisms is determined by the number of participating phonons, given by a Bose population factor [151]. The corresponding light attenuation coefficient accounting for both Stokes and anti Stokes components in a transparent solid may be estimated as follows (see also [149])

$$\alpha_{B,R} \approx \alpha_{B0,R0}\left(\frac{\lambda_0}{\lambda}\right)^4\left[\left(\exp\frac{\hbar\Omega_{B,R}}{k_BT} - 1\right)^{-1} + \frac{1}{2}\right] \tag{3.32}$$

where λ is the wavelength of light, $\alpha_{B0,R0}$ are the scattering parameters given by the properties of a particular crystal corresponding to λ_0, Ω_B is the Brillouin frequency shift for 90° scattering and Ω_R is the Raman frequency shift.

We assume that the crystal has a single phonon branch. Using data evaluated for CaF_2 at $T=300$ K in [148]: $\hbar\Omega_B/k_BT \simeq 1/300$, $\hbar\Omega_R/k_BT \simeq 1/4$, $\lambda_0 = 0.532$ μm, $\alpha_B = 2.411\times10^{-7}$ cm^{-1}, $\alpha_R \simeq 4.34\times10^{-8}$cm^{-1} we obtain $\alpha_{B0} \simeq 8\times10^{-10}$ cm^{-1}, $\alpha_{R0} \simeq 1.1\times10^{-8}$ cm^{-1}. It is easy to see that Brillouin scattering is significantly suppressed at low temperature and the attenuation of light in a perfect crystal is determined by the spontaneous Raman scattering. The room temperature attenuation, on the other hand, is given by spontaneous Brillouin scattering.

It is shown by Logunov and Kuchinsky [148] that the existing calcium fluoride crystals have transparency close to the fundamental limit (Equation 3.32) in the UV. However, such a low attenuation is yet to be demonstrated in experiments with visible and infrared light. The measured transparency is two to three orders of magnitude lower than the fundamental limit in those frequency bands [38,141,134] because of the extrinsic and intrinsic impurities of the material.

We now discuss the optical properties of fluorite WGM resonators. The maximum quality factor of the resonator is given by $Q_{\max} = 2\pi n(\lambda)/[\lambda\alpha(\lambda)]$, where $n(\lambda)$ is the refractive index of the material, λ is the wavelength of light in vacuum, and $\alpha(\lambda)$ is the total loss coefficient of the bulk dielectric material. The corresponding wavelength dependence of the attenuation as well as Q factor for CaF_2 are shown in Figure 3.20. The approximation of the maximum quality factor of CaF_2 WGM resonators found elswhere [141,134] using existing experimental results nearly coincides with the fundamental limit presented in Figure 3.20.

The wavelength dependence of the index of refraction of the material at $T=300$ K was found using the four-term Sellmeier equation [152]. Blue and red absorption wings may

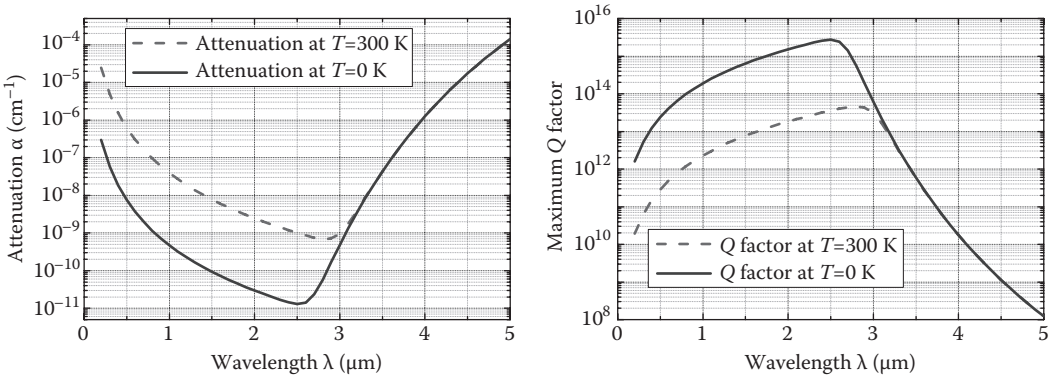

FIGURE 3.20
Attenuation in ideal CaF_2 and Q factor of ideal crystalline WGM resonators at room and nearly absolute zero temperature. Contributions from spontaneous Brillouin, Rayleigh and Raman scattering as well as blue and red wing absorption are added. (Reprinted from Grudinin, I. S., Matsko, A. B., and Maleki, L., *Opt. Express* 15, 3390–3395, 2007. With permission from OSA.)

generally be approximated by a simple exponential dependence [153,154]. Parameters for the blue wing were derived from Laufer et al. [155]; red wing parameters were obtained from Boyer et al. [156] and the experimental data publicly available for Corning CaF_2. For our analysis we assume both wings to be temperature independent, given that the actual temperature dependence is weak.

Not only spontaneous, but also stimulated scattering is important in macroscopic WGM resonators. Stimulated Rayleigh scattering is not experimentally observable in high-Q WGM resonators as it is suppressed by a mismatch of modal structure of a typical cavity and the gain profile for this process [149]. Stimulated Brillouin scattering is generally suppressed because of the absence of phase matching in the WGM resonators. The resonantly enhanced SRS is always possible if the frequency difference between subsequent modes of the same mode family (FSR) is less than the spectral width Γ of the optical phonons. In fluorite at room temperature $\Gamma = 450$ GHz [157]. Hence, any resonator with radius $R \geq c/(2\pi n(\lambda)\Gamma) \simeq 75\ \mu\text{m}$ is not immune to SRS. The properties of the stimulated scattering processes are discussed in the other chapter available in this volume.

3.5.2 Technical Limits

The optical Q factor of a resonator after polishing is limited by contributions from two main technical sources: (i) absorption and scattering due to accumulation of dust on the resonator surface, (ii) absorption and scattering in the resonator material due to intrinsic and extrinsic impurities.

Absorption due to dust particles would be the main restriction on the quality factor if a clean room environment is not provided. Once inside the clean room environment or vacuum, the Q factor can be preserved on a very high level for an indefinite length of time. Aside from dust accumulation, optical polishing leaves some amount of nanoparticles embedded into the resonator surface. It is known that water is detrimental for Q factors of fused silica devices due to the formation of irregular adsorption layers. Fortunately, crystals such as CaF_2 and MgF_2 have chemical properties that reduce accumulation of water on the surface. Diffusion of water into crystalline lattice is inhibited, while water monolayer (a one molecule thick layer) is always present on the surface.

The intrinsic absorption of the resonator material is the second important effect restricting the value of the measured Q factor. The absorption is a function of crystal growing process and is defined by the optical properties of a crystal at a given wavelength. This parameter is particularly small in crystalline materials, since they can be produced with high purity (see previous section). Recent developments in UV lithography have stimulated the production of extremely pure CaF_2 monocrystals. However, even in those purest crystals the "reference-sheet" absorption rarely falls below 10 ppm/cm, which corresponds to quality factors on the order of 10^{10}.

The surface roughness is made small by the polishing technique, as confirmed by measurements with an AFM. In its contribution to surface scattering factor, the surface roughness is accompanied by the subsurface material damage. This damage is represented by the microfractures and embedded particles and is usually confined to within a shallow surface layer of the material. The thickness of this layer is determined by the polishing and grinding process. Studies with atomic force microscope (AFM) have shown the small amount of diamond particles embedded into the resonator surface. This could be useful in quantum optics, since quantum dots containing diamonds or other nanoparticles can be embedded in this way to create a coupled system without noticeable degradation of the Q factor.

For example, we have fabricated a calcium fluoride resonator with 100 μm in diameter and optical Q factor of 4×10^8. The surface roughness does not restrict the value of the quality factor. The measurements performed with an AFM showed that the surface roughness in small resonators is about the same as in the large disks with Q factor of about 10^9 and is practically negligible ($\sigma=0.33$ nm) [38]. Let us estimate the maximum Q factor that could be achieved in a resonator with measured surface roughness. We will use the expression derived by Gorodetsky [21]

$$Q \approx \frac{3\lambda^3 R}{8n\pi^2 B^2 \sigma^2} \tag{3.33}$$

where λ is the wavelength, R is the radius of the resonator, n is the refraction index of the resonator material, B is the correlation length, and σ is the roughness. The formula was obtained as an approximation which takes the correlation length to be much smaller than the wavelength of light ($\sigma B^2 \ll \lambda^3$). It was found that $Q=4\times10^{12}$ for $\lambda=1$ μm, $R=50$ μm, $n=1.43$, $B=2$ nm (was not calculated), and $\sigma=0.33$ nm [38]. The estimated value of the Rayleigh scattering limited Q factor scales proportionally to the radius for smaller resonators and is still much larger than any Q factor observed in WGM resonators.

More rigorous studies of the surface quality of ultra-high Q WGM resonators were performed in [134]. It was taken into account that the noise introduced by AFM is small (the AFM empty image standard deviation was 0.07 nm). The surface roughness was measured to be 0.19 nm and 0.15 nm in two different samples. Calculations were made with a standard expression for the unbiased variance. These values are significantly smaller than those typical of fused silica resonators, and demonstrate the capability of the fabrication technique. It is possible to achieve even better results if advanced polishing techniques are used.

In order to use the analysis, the correlation length B also has been carefully evaluated. The correlation length is defined as the decay length of the exponential autocorrelation function. We are interested in the correlation length along the direction of light propagation, which in our case is coincident with the direction of polishing traces. Computer

algorithms of the image rotation generally alter the correlation function. In addition, the autocorrelation function depends on the direction of computation for the type of the surface discussed here. In order to overcome these problems, a two-dimensional correlation function may be computed with the use of a Wiener–Khinchin theorem and fast Fourier transform algorithms. It was found that $B \simeq 40$ nm, 20 times larger than the value assumed in [38]. The maximum corresponding Q is on the order of 7×10^{11} and is still higher that the quality factors measured experimentally.

It was also found that when an excimer grade CaF_2 is used, it is possible to achieve a Q factor higher than in any other open resonator and any other WGM resonator without annealing. The 5.5 mm in diameter CaF_2 WGM resonator was fabricated with Q factor of $(5.31\pm0.04)\times10^{10}$ measured with a Nd:YAG laser at wavelength of 1064 nm. This is probably due to specific impurity content of the resonator host material.

To conclude this section, we note that a record high optical Q factor of a fluorite WGM resonators fabricated with a diamond grinding technique was demonstrated. Even higher Qs for WGM resonators made out of this and other materials were predicted after an analysis of possible loss mechanisms in crystals and the influence of nonlinear processes.

The extreme Q factors of crystalline resonators open new opportunities for optical filtering and spectroscopy. A single mode cavity made with lithium niobate could operate as a tunable fiber coupled etalon, more compact and with a higher finesse than a FP resonator. We discuss such filters in the following section.

3.6 Filters and Their Applications

Photonic filters based on optical WGM resonators are currently among the highest developed devices that utilise WGMs. For optical telecommunication purposes, the main task of the filters is to select channels, as in wavelength division multiplexing schemes. In this domain, where channel spacing is usually no less than 10 GHz, planar ring resonators with WGM and similar devices with $Q<1\times10^5$ are adequate [163–168].

Ultra-high-Q WGM resonators with MHz range resonance bandwidths offer a unique opportunity for realization of photonic microwave filters in which optical-domain selection is used for separating the RF channels imprinted as sidebands on a stable optical carrier. Photonics filters based on optical resonators address the shortcomings of microwave filters. Multi-pole, high-Q filters based on cascaded WGM resonators fabricated with silica have been demonstrated allowing compact packages and robust performance. These filters provide passbands with a flat-top and sharp skirts, suitable for high performance applications. Since microwave signals in photonic systems are sidebands of an optical carrier, these filters can be used at any microwave frequency, providing the same characteristics throughout the band, from 1 to 100 GHz, and higher.

While delivering high optical Qs and desirable passband spectra, optical WGM filters based on silica ring resonators are limited in their microwave Q, and are not tunable. Crystalline WGM filters overcome this problem. Fabrication of optical WGM resonators with lithium niobate and tantalate [159] has led to the demonstration of high-Q tunable filters with linewidth of about 1 MHz and wider. A crystalline WGM resonators was used as a Lorentzian microwave filter with a tuning range in excess of tens of gigahertz [160]. A miniature resonant electro-optically tunable third-order Butterworth filter based on cascaded lithium niobate WGM resonators has also been demonstrated

[161]. Fabrication of a fifth-order narrow band tunable WGM filter was reported in Savchenkov et al. [162].

Existing WGM filters still do not solve all the problems of the microwave photonics. For example, a recently demonstrated lithium niobate WGM filter [161] has a third-order filter function, 30 MHz linewidth, and is tunable over a wider range of frequency (>20 GHz). Agile tunability accompanied by the third-order filter function, narrow linewidth, and low loss, make this filter exceptionally useful for various microwave photonics applications. However, the comparatively low-order filter function represents a limitation for the application of these filters in microwave systems that require efficient sidemode rejection, and high transmission/rejection contrast. While increasing the number of coupled WGRs theoretically yields the required high-order high-contrast filter function, the technical problems associated with the device fabrication pile up exponentially. Some of these problems were analyzed and solutions were proposed in Savchenkov et al. [162]. In what follows we review recent achievements in fabrication of filters using crystalline WGM resonators.

3.6.1 First-Order Filters

The simplest resonator-based filter includes a WGM resonator and an optical coupler, e.g. a prism or an angle-polished fiber coupler (Figure 3.21). Transmission of a monochromatic electromagnetic wave of frequency ω by an optical WGM resonator in a single prism configuration may be characterized by Equation 3.4.

The filter described by Equation 3.4 is a stop-band filter because it is characterized by the absorption resonance. A WGM resonator with two, input and output, couplers is characterized by a transmission resonance (Figure 3.21). This is a passband filter. An example of a packaged passband filter consisting of a single WGR is shown in Figure 3.22. The transmission and reflection coefficients through the resonator are given by Equations 3.8 and 3.9.

An example of the tunability of a stop-band $LiNbO_3$ WGM filter is shown in Figure 3.23. The maximum frequency shift of TE and TM modes may be found from [158]

$$\Delta v_{TE} = v_0 \frac{n_e^2}{2} r_{33} E_Z, \quad \Delta v_{TM} = v_0 \frac{n_o^2}{2} r_{13} E_Z, \tag{3.34}$$

where $v_0 = 2 \times 10^{14}$ Hz is the carrier frequency of the laser, $r_{33} = 31$ pm/V and $r_{13} = 10$ pm/V are the electro-optic constants, $n_e = 2.28$ and $n_o = 2.2$ are the refractive indexes of $LiNbO_3$, E_Z is the amplitude of the electric field applied along the cavity axis. We worked with TM modes because they have larger quality factors than TE modes. If the quality factor is not

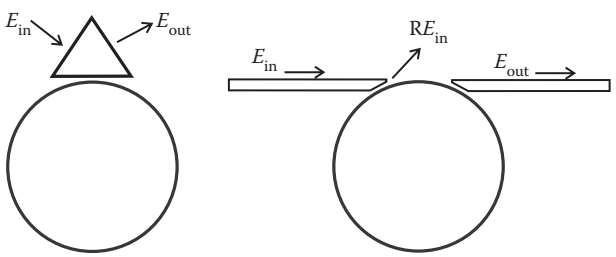

FIGURE 3.21
Scheme of single resonator filters with different coupling elements. The resonator with prism coupling element is a stop-band filter. The resonator with two angle-polished fiber couplers is a pass-band filter.

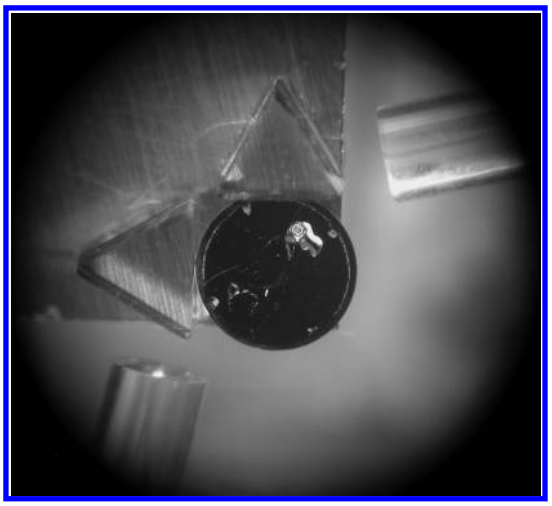

FIGURE 3.22
Filter setup with two prism couplers (passband configuration). The lithium niobate disc resonator is coated with metal.

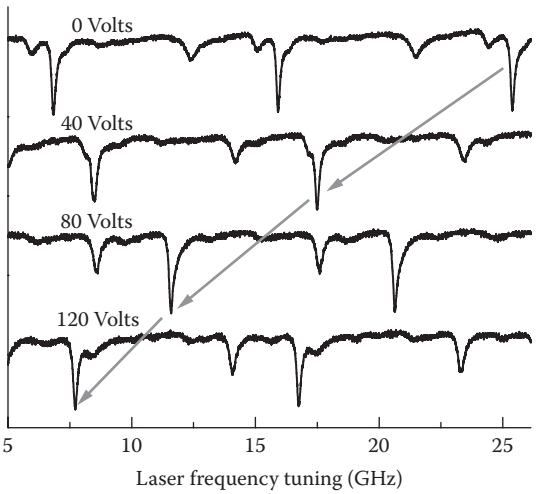

FIGURE 3.23
Tunability of the resonator spectrum, 14.7 GHz spectral shift per 100 V of applied voltage. Resonator FSR is 9.5 GHz.

very important, it is better to work with TE modes because their electro-optic shifts are three times as much as those of TM modes for the same value of the applied voltage.

Theoretically, Δv_{TE} and Δv_{TM} do not depend on the resonator properties and are related to the fundamental limitations of optical resonator-based high speed electro-optic modulators [169]. The results for different resonators measured in our experiment are not completely identical, a result that stems from the imperfections of the cavity metal coatings as well as a partial destruction of the coating during the polishing procedure.

The measured insertion loss for the pass band filter shown in Figure 3.22 was less than 5 dB (Figure 3.24). The insertion loss occurs primarily due to inefficient coupling to the

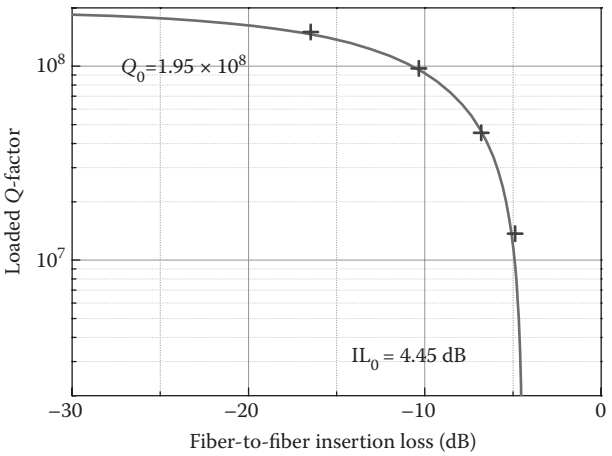

FIGURE 3.24
Insertion loss versus quality factor for a single resonator filter. The loading determined by the distance between the coupling prisms and the resonator was changed by temperature. The crosses stand for the experimental point and the line is the theoretical fit of the experimental results.

mode. We believe that antireflection coating of the coupling prisms or use of special gratings placed on high-index fibers may reduce the losses significantly.

For the pass band filter shown in Figure 3.22, we analyzed the operation of the filter in the switching regime. We sent microwave pulses to the filter and observed a change in light transmission as the microwave pulses entered the filter. An example of such a measurement is shown in Figure 3.25.

3.6.2 Periodical Poling and Reconfigurable Filters

Absolute tunability of optical resonator-based photonic filters is characterized by the ratio of their FSR and their linear tunability range. Tuning the filters does not change the FSR but only shifts the comb of the optical modes, making it to overlap with itself for each frequency shift proportional to the FSR. Hence, the filter can be tuned at any prescribed single frequency if the linear tunability exceeds the FSR.

Some photonic applications call for narrowband filters passing simultaneously both the carrier and the sidebands. For example, this is important for generation of spectrally pure microwave signals in opto-electronic oscillators, where beating of the optical sidebands and the carrier on a fast photodiode generates microwaves. Tunability of the microwave frequency of the oscillator requires a controlled change of the frequency difference between the filter passbands. This feature is lacking in existing tunable filters where the entire filter spectrum shifts as a whole as the tuning voltage is applied.

A filter with electro-optically reconfigurable spectrum was recently demonstrated [173]. The filter is based on a WGM resonator fabricated from a commercially available lithium niobate wafer. The crystalline resonator was fabricated with a special domain structure that results in controllable shift of the frequency of a single mode or a group of modes with respect to the other modes, as a DC bias voltage is applied across the resonator. This provides the possibility of tuning one resonance mode while keeping the rest of the spectra stationary. The filter may be characterized along the same lines as a FP filter with a tunable FSR. The proposed method has the potential for fabrication of resonant photonic filters with arbitrary passband spectrum.

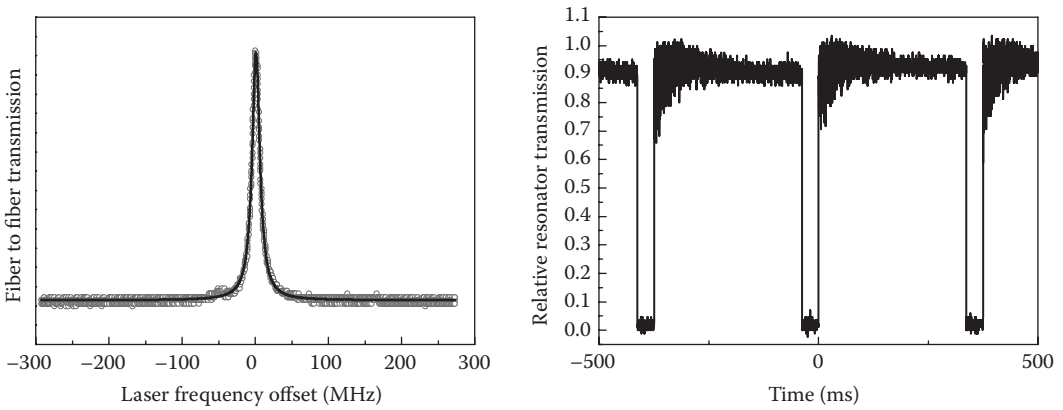

FIGURE 3.25
Left: the transmission resonance of the filter. The filter has 13.8 MHz FWHM and 4.3 dB insertion loss at the resonance. Right: 200 ns pulse front response in the switching regime. .

The filter operates at 1.55 μm wavelength, though the wavelength of operation is limited only by the absorption loss of lithium niobate and can be anywhere from about 1.0 to 1.7 μm. The reproducible value of the finesse of the filter (F) exceeds $F=300$, but in some experiments finesse $F=1000$ was achieved.

The filter is a circular resonator made from electro-optic material (Figure 3.26). As discussed above, a homogeneous change of an applied electric field results in a homogeneous change of the refractive index for a single-domain crystalline resonator and, as a consequence, in a frequency shift of the whole resonator spectrum. We propose to manipulate the domain structure in the material to produce an inhomogeneous electro-optic effect in the resonator in such a way that targetted mode families experience frequency shifts with respect to other mode families.

The maximum frequency shift of the TE and TM mode can be found from

$$\Delta\omega_{\mathrm{TE}} = \omega_0 \frac{n_e^2}{2}\left(\int_V r_{33} \mid E_{\mathrm{TE}} \mid^2 E_Z d\mathbf{r}\right)\left(\int_V \mid E_{\mathrm{TE}} \mid^2 d\mathbf{r}\right)^{-1}, \tag{3.35}$$

$$\Delta\omega_{\mathrm{TM}} = \omega_0 \frac{n_o^2}{2}\left(\int_V r_{13} \mid E_{\mathrm{TM}} \mid^2 E_Z d\mathbf{r}\right)\left(\int_V \mid E_{\mathrm{TM}} \mid^2 d\mathbf{r}\right)^{-1}, \tag{3.36}$$

where ω_0 is the carrier frequency of the laser, r_{33} and r_{13} are the electro-optic coefficients, sign of which is determined by the direction of the domain of the crystal, which could be either $+z$ or $-z$, with respect to the homogeneous DC bias electric field E_z; n_o and n_e are the refractive indices of lithium niobate, E_{TE} and E_{TM} are the amplitudes of the electric fields of the modes. The integration is taken over the resonator volume V.

Various modes of a WGM resonator have various spatial dependences (Figure 3.26b). The tunability of the modes can be changed in different ways by choosing spatial dependence of the electro-optic coefficients in a correct manner through poling the crystal.

A schematic diagram of the filter configuration is shown in Figure 3.26. Several 2.6 mm diameter disk-shaped resonators of $LiNbO_3$ were fabricated, at 120 μm thickness. The rims

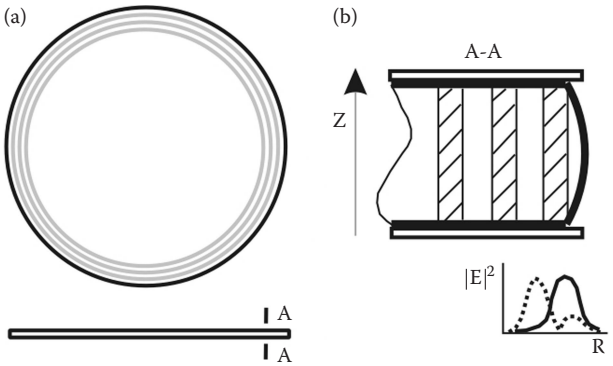

FIGURE 3.26
Schematic of the metalized disc resonator used in the reconfigurable filter. The resonator is made from a periodically poled lithium niobate wafer. (a) Picture of the disc resonator. The inverted domain structure is shown with gray circles. (b) Crossection of the resonator close to the disc rim. Inverted domain structure is shown by striped areas. Two geometrical structures of electro-magnetic modes of the resonator (radius dependence of the mode power distribution) are shown under the resonator crossection. The mode depicted by solid line is barely shifted by the applied voltage, while the mode shown by dotted line moves. (Reprinted from Mohageg, M., Savchenkov, A., Strekalov, D., Matsko, A., Ilchenko, V., and Maleki, L., *Electron. Lett.* 41, 91–92, 2005. With permission from Institute of Electrical Engineers (IEE).)

of the cylindrical disks were polished to resemble the surface of a sphere. A ferroelectric domain structure reminiscent of a set of rings concentric with the axis of the disk resonator was generated by dragging a 1 μm diameter electrode across the surface of the crystal while applying a 2.5 kV bias between the electrode and the bottom of the crystal, causing a permanent change in the structure of the material polarization. The poling process took place at room temperature and was visualized in situ by reflecting light from the bottom surface of the crystal. Domain walls, that is, barriers between polarizations parallel to $+z$ and $-z$ directions, are clearly visualized as dark bands in the reflected light.

The top and bottom surfaces of the polished and poled disk resonator were placed into contact with metal electrodes. These electrodes were connected to a 0–150 V regulated DC power supply. A probe beam of 1.55 μm scanned over 20 GHz was coupled into the resonator through a diamond prism. This allowed observing the absorption spectrum of the poled disk resonator and the motion of the modes as the voltage bias across the resonator axis was increased.

The first disk was poled with a ring-shaped domain pattern 5 μm edge-to-edge at the disk rim and a 35 μm thick ring-shaped domain 20 μm away. The probe was coupled into the WGMs of the resonator with quality factor of 10^7. When the probe beam was coupled into the high-Q modes of the first disk and voltage was applied, the radical mode was observed to change frequency with respect to the rest of the spectra at a rate of 21 MHz/V (Figure 3.27). The Q-factor of the resonance was maintained constant through the most of the motion. The mode motion was observed over 10 V of bias change.

3.6.3 Third-Order Filters

We made several miniature resonant electro-optically tunable third-order Butterworth filters. The filters are based on three metal coated WGM resonators fabricated from a commercially available lithium niobate wafer. The filters, operating at 1550 nm wavelength, have less than 30 MHz bandwidth and can be tuned in the range of ~±12 GHz by applying

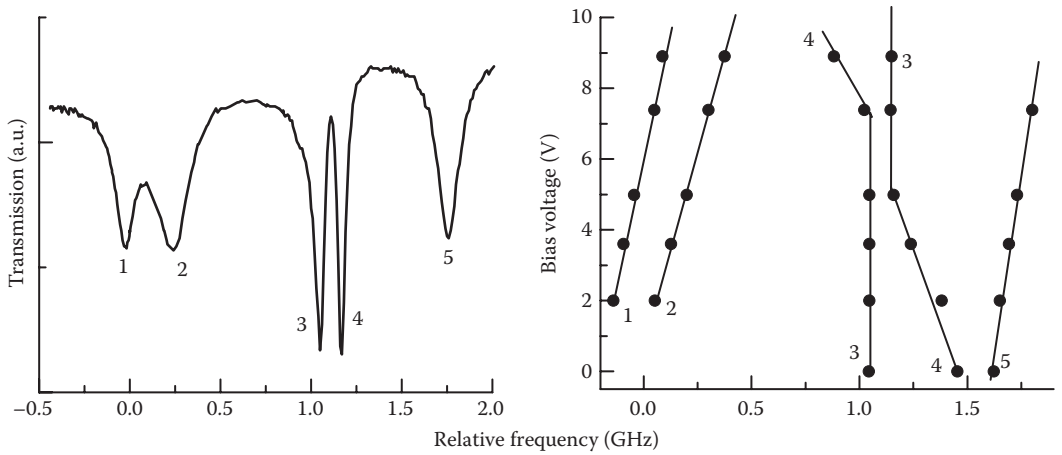

FIGURE 3.27
Spectrum of the WGM resonator and its tunability. The resonances 3 and 4 move through each other with bias voltage change. When the frequencies of the modes coincide, the mode interact due to residual light scattering in the disc resonator. Relative frequency shift between modes 3 and 4 versus applied bias voltage. (Reprinted from Mohageg, M., Savchenkov, A., Strekalov, D., Matsko, A., Ilchenko, V., and Maleki, L., *Electron. Lett*. 41, 91–92, 2005. With permission from IEE.)

a DC voltage of ~±150 V to an electrode. The basic operation principles of the filter are discussed in Savchenkov et al. [161].

The FSR of each resonator is approximately 10 GHz, and, therefore, the filter can be tuned practically at any optical frequency in the transparency window of lithium niobate. To clarify this statement, let us consider a single resonator first. If we are able to tune its spectrum by the FSR frequency, the resonator spectrum would overlap with itself, which means that it is always possible to find and to shift a resonator mode to coincide with an arbitrary external signal frequency. We do not need to use the same mode for filtering. Now, if we consider several interacting resonators, and tune the frequency of a mode of the smallest resonator (the largest FSR) by the FSR value, and hence the modes of the other resonators by values exceeding their FSR, then a high-order filter passband may be constructed at any desired frequency.

We note the following distinctive features/advantages of this type of filter over conventional filters: (i) agile tunability accompanied by a high-order filter function, (ii) narrow linewidth, and (iii) low fiber-to-fiber loss. Combination of these three features makes this a unique filter for a wide range of applications in optics and microwave photonics.

Tunable single-resonator filters are characterized by their finesse which is equal to the ratio of the filter's FSR and the bandwidth. The three-resonator filter has a significantly more sparse spectrum as compared with a stand alone WGM resonator. This feature is due to the so called Vernier effect [170] and is similar to the coupled fiber-ring resonators [171,172] which are noted for a rare spectrum due to a single sequence of modes. Finesse of the system is very large as the FSR exceeds 1 THz, though we were unable to measure it accurately because of the limited tuning range of the laser. The tuning speed of the filter is limited by the wiring layout and is approximately equal to 10 ns, while the actual shifting time of the spectrum is determined by the filter's bandwidth and does not exceed 30 ns.

The resonators were cut out from Z-cut metalized crystalline preforms. Each resonator perimeter edge was hand polished to a toroidal shape. The repeatable value of the loaded quality factor of the main sequence of the resonator modes was $Q \simeq 1.6 \times 10^7$, which

corresponds to 15 MHz bandwidth of the mode. We studied several disks with nearly identical characteristics.

The resonators were arranged in the horizontal direction with home-made flex manipulators (Figure 3.28). There was no need in a vertical adjustment because the surface of the stage the resonators were placed on was optically polished and all resonators had the same thickness (with nanometer accuracy). The gaps between the resonators and between the prisms and the resonators were 50–100 nm, which corresponds to the evanescent field scale. We did not measure the gaps directly but adjusted them to have the appropriate system response.

Light was sent into, and retrieved out of, the first and last resonators in the array of the filter via coupling prisms. The repeatable value of fiber-to-fiber insertion loss, primarily due to inefficient coupling to the resonator modes, was less than 6 dB across the entire cascaded structure. The maximum transmission was obtained when light was resonant with the resonators modes. The antireflection coating of the coupling prisms or use of special gratings placed on high-index fibers may reduce the losses significantly. Tuning the filter was realized by applying a voltage to the top and bottom electrodes fabricated with gold. The gold coating is absent on the resonator perimeter edge where WGMs are localized.

The differences in the size of the resonators is important in the fabrication of the multiresonator filter. Our aim was to produce spectral lines in all three resonators with a similar width to allow the realization of a complex line structure. If the interacting modes of resonators have different widths, then as they are tuned to approach each other, the height of the narrower resonance will simply track the shape of the wider ones, which is of no use for the filter application. The size of each resonator is important since cavities of similar size have similar optical coupling and similar FSRs. So similar optical modes with the same efficiency can be excited in each of them. The performance of the filter demonstrates that indeed similar resonators with approximately the same parameters were fabricated.

Figure 3.29 depicts the spectrum obtained in the experiment with three cascaded $LiNbO_3$ resonators. To highlight the filter performance the theoretical third-order Butterworth fit of the curve is also plotted. Obviously, the three-cavity filter has much faster roll off compared with the Lorentzian line of the same full width at half maximum. On the other

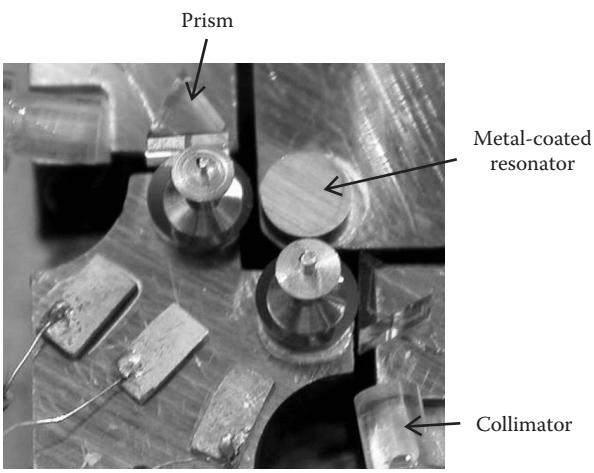

FIGURE 3.28
A packaged assembly of the three resonator filter.

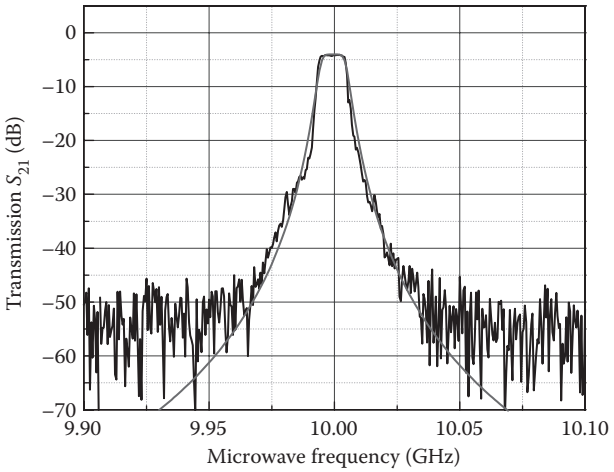

FIGURE 3.29
Transmission curve of the filter and its fit with Butterworth profile function $\gamma^6/[(\upsilon-\upsilon_0)^6+\gamma^6]$, where γ=5.5 MHz, υ_0 determines the center of the filter function and primarily depends on the resonators' geometrical dimensions. Voltages applied to the resonators vary from near zero to 10 V to properly adjust modes of each individual resonator and construct the collective filter function as shown.

hand, the filter function does not look exactly like a third-order bandpass because of small differences between the cavity Q-factors and dimensions of the resonators.

The experimentally measured electro-optic tuning of the filter's spectral response, and tuning of its center frequency with an applied voltage, is shown in Figure 3.30. The filter exhibits a linear voltage dependence in the ±150 V tuning range, i.e. the total tuning span exceeds the FSR of the resonator. Changing the tuning voltage from 0 to 10 V shifted the spectrum of the filter by 1.3–0.8 GHz for TM mode polarization.

3.6.4 Fifth-Order Filters

We have also realized a five-WGR filter [162]. The filter (Figure 3.31), operating at the 1550 nm wavelength, has approximately 10 MHz bandwidth and can be tuned in the range of 10 GHz by applying a DC voltage of approximately 100 V to the graphite electrodes. The FSR of each resonator is approximately 10 GHz, and the filter may be tuned practically at any optical frequency in the transparency window of lithium niobate. This filter exhibits 12 dB of fiber-to-fiber insertion loss with.

For the five pole filter, the resonators were cut out from congruent Z-cut crystalline wafers and had approximately 4 mm in diameter and 100 μm thickness. Each resonator's rim was polished in the toroidal shape with a 50 μm curvature radius. The repeatable value of the loaded quality factor of the main sequence of the resonator modes was $Q=3\times10^7$ (the unloaded maximum was $Q=1.5\times10^8$). Resonators were arranged in the horizontal plane using flex manipulators. The gaps between the resonators, and between the coupling prisms and the resonators, were less than 100 nm, and were adjusted to maintain the appropriate system response.

3.6.5 Sixth-Order Filters

We also fabricated six-pole filters using metalized WGM resonators. Naturally, these filters had higher insertion loss compared with the lower order filters. It was also difficult to keep

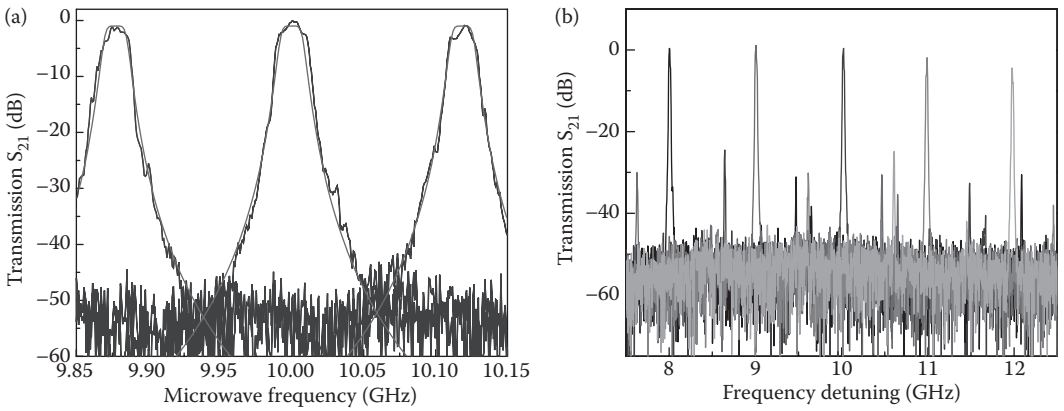

FIGURE 3.30
Demonstration of the tunability of the three-resonator filter. Left: Tuning of the filter and its Butterworth fit with 16.6 MHz pass band. Right: Broadband tuning of the filter. It is possible to see spurious pass bands not completely suppressed with the Vernier effect.

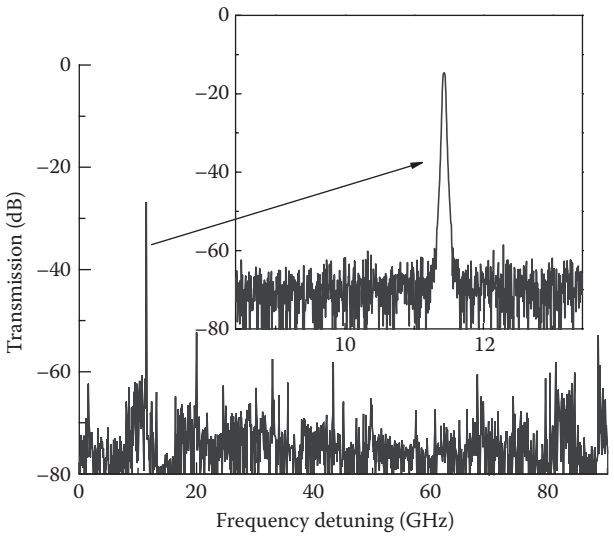

FIGURE 3.31
Demonstration of the five-resonator filter. (Reprinted from Savchenkov, A. A., Matsko, A. B., Ilchenko, V. S., Yu, N., Maleki, L., Millimeter and Submillimeter Waves and Workshop on Terahertz Technologies, 2007. The Sixth International Kharkov Symposium, 1, 79–84. With permission from Institute of Electrical and Electronics Engineers (IEEE).)

a stable the shape for the passband. An example of the six-pole filter function with 13 MHz pass band is shown in (Figure 3.32).

3.6.6 Tuning of the Multi-Resonator Filter

We now discuss in more detail considerations regarding tuning requirements of multi-resonator filters. A multiresonator filter has the required flat-top Butterworth shape of the order corresponding to the number of the resonators, if selected modes of the resonators have approximately the same frequency and loaded Q-factors, as discussed above. Generally it is not feasible to fabricate a pair of high-Q WGM resonators with coinciding

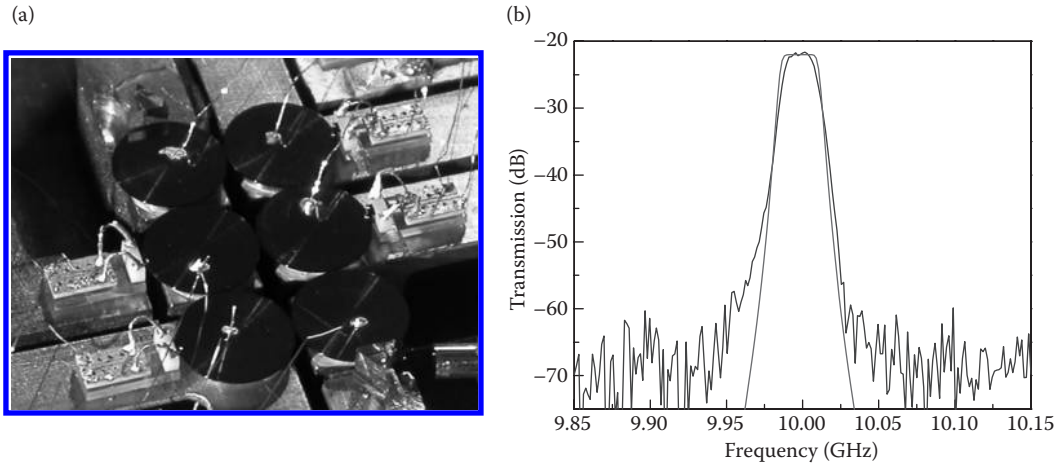

FIGURE 3.32
Demonstration of the sixth-order filter.

optical modes. For instance, the resonators have identical spectra if the error in their radius is much less than $\Delta R = R/Q$. This is approximately 0.01 nm for a $Q = 10^8$ resonator of 0.2 cm in diameter. Moreover, even if such resonators are fabricated, their relative temperature should be stabilized to better than $T = n/\kappa Q = 2$ mK to avoid relative drift of their spectra, where $\kappa \sim 10^{-5}$ K^{-1} and $n = 2.3$ are the combined thermal expansion/thermorefractive coefficient and the extraordinary index of refraction of the lithium niobate, respectively. Such a thermal stabilization is generally not convenient. Aside from these stringent requirements the Q-factors of the resonators must also be identical within a few percent margins to realize a proper filter function.

A partial solution to this is provided by the electro-optical properties of the material. It is possible to trim frequencies of each (nonidentical) resonator with a DC electric bias, or voltage, applied to the resonator. The value of the bias should follow the changes of the frequencies of the resonator and the laser. This scheme works well for a single WGM filter that requires only one bias [160]. The case of the three-WGR filter [161] is more challenging because it requires three independent biases; it is difficult to independently track frequencies of the three WGMs involved, especially the frequency of the central resonator. The growing complexity associated with filters having even a higher order makes their realization quite challenging.

We propose two schemes that simplify tuning the independent resonator frequencies. For the three-WGR filter the method involves optical probing the frequencies of two end resonators when the coupling between the resonators is small (tunable gaps are large, see Figure 3.33A). The frequency of the central resonator is selected by subsequently reducing the gaps between the resonators, and ramping the bias of the central resonator until the proper transmission function is realized. A similar technique works with the five-resonator filter (Figure 3.33B). In the first step a required second-order transmission function is realized with two uncoupled end pairs of the resonators. The central resonator is then tuned after the coupling is restored.

Nonetheless, this technique has several disadvantages: (i) it requires dark periods in the operation of the filter, (ii) it does not work with filters having higher order than five, and (iii) it requires a mechanical change of the shape of the filter (tuning the gaps between the WGM resonators). We have found a more efficient and robust technique to address these

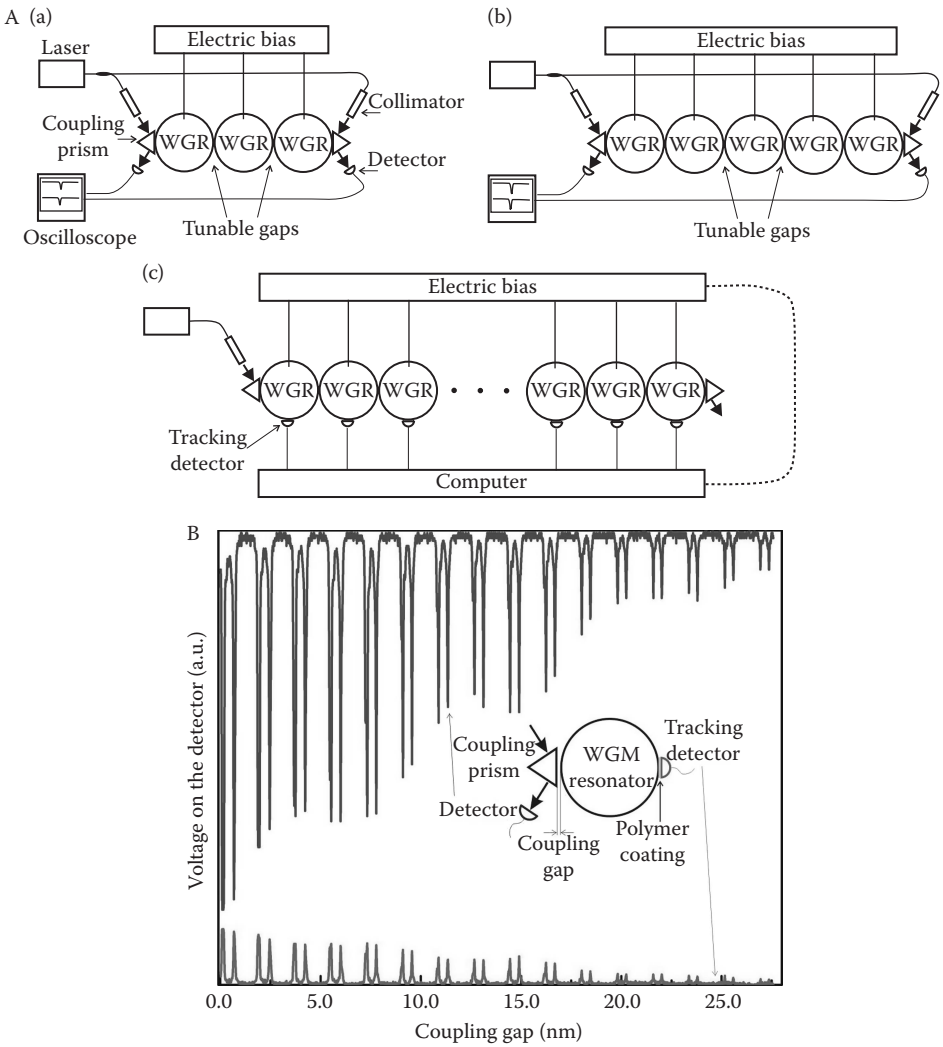

FIGURE 3.33
(A) Possible configurations for tuning the multiresonator WGM filters: (a) three resonator filters, (b) five resonator filters, and (c) multiple resonator filters. Scheme (c) involves tracking photodiodes. (B) Demonstration of the efficiency of the tracking photodiode method. The visibility of a WGM doublet as a function of the resonator load, regulated by the gap between the coupling prism and the resonator surface. This was observed by means of direct detection of light transmission through the resonator as well as by measurement with the tracking photodiode. (Reprinted from Savchenkov, A. A., Matsko, A. B., Ilchenko, V. S., Yu, N., Maleki, L., Millimeter and Submillimeter Waves and Workshop on Terahertz Technologies, 2007. The Sixth International Kharkov Symposium, 1, 79–84. With permission from IEEE.)

shortcomings. Fortunately, a slow photodiode coated with a hundred nanometer transparent polymer film and attached to the rim of a WGM resonator does not reduce its Q-factor significantly. The decrease is less than a couple of percents if the resonator's loaded quality factor is $Q=10^8$. To demonstrate the operation of the "tracking detector" we recorded a segment of a WGM spectrum, monitoring the transmitted light and the photocurrent while decreasing the resonator loading. It is easy to see from Figure 3.33 that the detector operates satisfactorily. With this approach it is possible to design a computer controlled

multipole filter (see, e.g. Figure 3.33C). The spectrum of each resonator in the chain is tracked by a photodiode, and is actively controlled by the microprocessor with feedback of the bias voltage applied to each resonator. There is practically no limitation on the number of WGRs in the filter with such a computer controlled scheme.

3.6.7 Resonator Coating Technique

Even when the problem of trimming of WGM frequencies is solved, the unequal Q-factors of the WGRs can hinder the desired response of the filter. Our mechanical polishing technique allows for fabricating resonator with quality factors determined exclusively by the intrinsic absorption of the material. Therefore, if all the resonators are made of the same material they will have the same Q-factors. The subsequent coating of the resonators with gold or any other conductor to form electrodes changes the Q-factor. The fabrication procedure is based either on repolishing the resonators after the coating process or on producing the resonators from gold-coated crystalline wafers. However, both solutions are difficult to realize. The resonator radius changes uncontrollably in the first case and the coating deteriorates in the second.

We have found that coating of the WGM resonators with colloidal graphite addresses these problems. Graphite has sufficient conductivity and is not expensive. It is easily removable from the resonator surface close to the rim where the electromagnetic field is localized. The graphite film can be literally wiped clean from the area without destruction of the quality of the polishing. These properties make the method advantageous for in-lab use.

We studied two possible ways of producing graphite coatings. One is more efficient from the point of view of tunability. The coating is removed only from the region where the WGM electromagnetic field is localized (Figure 3.34A). In this case the smallest distance between the electrodes (h), rather than the thickness of the resonator (H), determines the maximum tuning rate of the WGM spectrum per Volt. This allows fabrication of several-hundred micron thick resonators with tunability as if the resonator thickness is tens of microns. The method, nevertheless, has a disadvantage when applied to high-order filters. The coating in the vicinity of a WGM localization changes its Q-factor, which is undesirable. For this reason we analyzed a second approach for coating that does not influence the Q-factor (Figure 3.34B), though it has a lower efficiency compared with the first one. We found that it is not necessary to place the electrodes on the top and bottom of the WGM area. The DC electric field curves close to the resonator rim because of the large dielectric permittivity of the material, so the tuning efficiency does not change significantly if the electrodes are comparatively far from the rim. The Q-factor stays intact and the resonators can be placed in the chain.

3.6.8 Insertion Loss

Let us understand the nature of the insertion loss of the multiresonator filter. Using the formalism presented by Madsen and Zhao [174] we describe the field accumulated in each resonator with complex coefficients of transmission (T_j) and reflection (R_j). The coupling between resonators and between resonators and prism couplers is described by constants k_j (Figure 3. 35). The transmission and reflection coefficients are connected by a recurrent relation

$$\begin{bmatrix} T_{j+1}(37) \\ R_{j+1} \end{bmatrix} = \frac{1}{i\sqrt{k_j \exp\left[-(i\delta_j + \alpha_j)\right]}} \Phi_j \begin{bmatrix} T_j \\ R_j \end{bmatrix}, \tag{3.37}$$

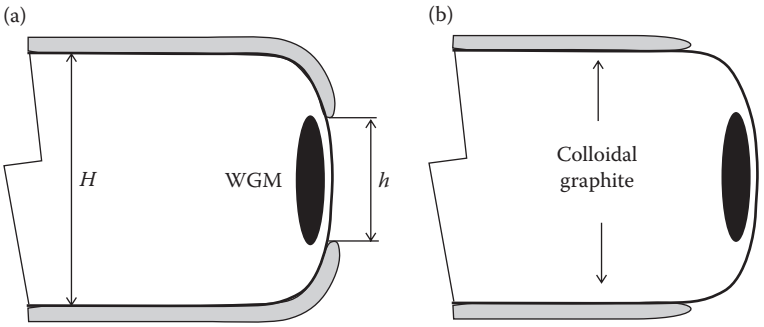

FIGURE 3.34
Application of the colloidal graphite for fabrication of DC electrodes mounted on crystalline WGM filters. (Reprinted from Savchenkov, A. A., Matsko, A. B., Ilchenko, V. S., Yu, N., Maleki, L., Millimeter and Submillimeter Waves and Workshop on Terahertz Technologies, 2007. The Sixth International Kharkov Symposium, 1, 79–84. With permission from IEEE.)

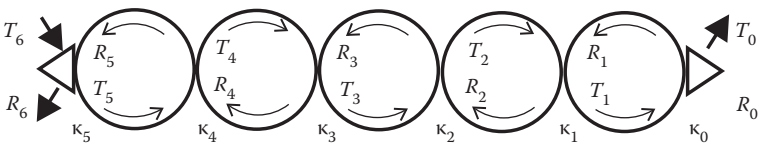

FIGURE 3.35
Parameters used to describe the resonator chain. (Reprinted from Savchenkov, A. A., Matsko, A. B., Ilchenko, V. S., Yu, N., Maleki, L., Millimeter and Submillimeter Waves and Workshop on Terahertz Technologies, 2007. The Sixth International Kharkov Symposium, 1, 79–84. With permission from IEEE.)

where δ_j and α_j represent the phase build-up and absorption per round trip in the resonator. For the sake of simplicity we assume that $\delta_j=\delta$ and $\alpha_j=0$. Then the transfer function for the five-resonator chain is

$$H_{11}=\frac{T_0}{T_6}e^{(i\delta+\alpha)/2},\quad H_{21}=\frac{R_6}{T_6}e^{(i\delta+\alpha)}. \tag{3.38}$$

It is easy to find that $P_r/P_{in}=|H_{21}|^2$ and $P_{out}/P_{in}=|H_{11}|^2$. The relative power in resonator #1 is given by $P_1/P_{in}=|T_5/T_6|^2$, in resonator #2 is $P_2/P_{in}=|T_4/T_6|^2$, etc.

To further simplify the problem we assume that $k_0=k_5=k_a$, $k_1=k_4=k_b$, and $k_2=k_3=k_c$. The resonator chain becomes a fifth-order Butterworth filter with power transfer function

$$|H_{11}|^2\simeq\frac{1}{1+\left(2^{7/5}\delta/\kappa_a\right)^{10}},\ \text{if}\ \kappa_b\simeq\frac{\kappa_a^2}{8},\ \kappa_c\simeq\frac{\kappa_a^2}{16}(1-\kappa_a),\ \text{and}\ \kappa_a\ \text{is arbitrary}. \tag{3.39}$$

Finally, it is worth noting that

$$\gamma_a=\frac{\alpha}{2\pi a}\frac{c}{n},\quad \gamma_c=\frac{\kappa_a}{2\pi a}\frac{c}{n},\quad \delta=\Delta\omega\frac{2\pi an}{c},$$

where a is the radius of each resonator, and n is the refractive index of the material.

In reality $\alpha \neq 0$ and the filter is always absorptive ($|H_{11}|^2 < 1$ for $\delta = 0$). We calculate $|H_{11}(\delta = 0)|^2$ keeping the relative coupling between the resonators the same as when evaluated for the lossless case. The resultant absorption increases approximately exponentially with the increase of relative intrinsic absorption Figure 3.36. The resonators must be overcoupled to obtain small losses. In our experiment with the five-pole filter $\gamma_a/\gamma_c \sim 0.25$. The observed 12 dB fiber-to-fiber insertion loss results from the absorption in the chain as well as other miscellaneous losses (reflection from the prism surface, not perfect phase matching, etc).

3.6.9 Vertically Coupled Resonators

In this section we discuss a chain of one dimensional ring-like WGM resonators [175,176], as a configuration for coupled resonator optical waveguides (CROWs) [177] and other resonator-based waveguides [178]. We show that the basic features of the chain can be adjusted by changing the shape of the resonators as well as the distance between them. Unlike ordinary CROWs, where coupled resonators are considered as "lumped element" objects, our structure is amenable to tuning its photon density of states and thus , e.g. slowing light down, similar to such "distributed" systems as photonic crystals. This resonator chain is similar to the vertically stacked multi ring resonator (VMR) [179].

Let us consider a resonator waveguide shown in Figure 3.37. The linearly polarized narrow band laser light is coupled to a mode of one of the resonators using a prism or an optical fiber coupler. Light propagates due to the coupling between adjacent resonators, which occurs via the evanescent field inside the rod from that the resonators are made of, not through the air [38,53], as is the case with conventional CROWs. To understand the difference, note that the dimension of the evanescent field in the air outside a resonator scales as $l_e \sim \lambda/\pi(\varepsilon_0 - 1)^{1/2}$, where ε_0 is the electric susceptibility of the resonator material and λ is the wavelength of the light in vacuum. This value is usually equal to several hundreds of nanometers. In contrast, in this system coupling is efficiently realized between

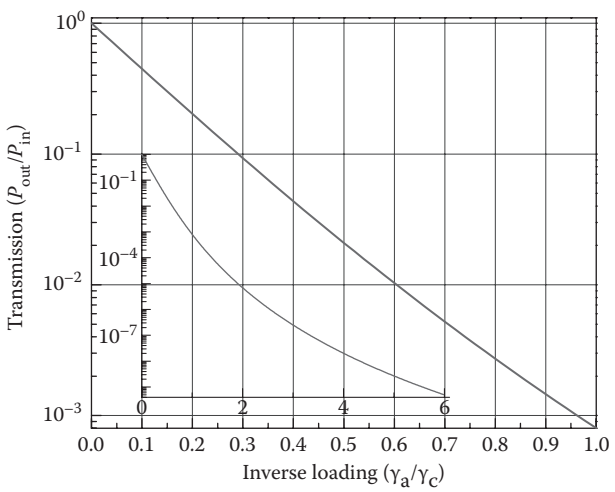

FIGURE 3.36
Dependence of the transmission coefficient of the filter on the resonator loading. (Reprinted from Savchenkov, A. A., Matsko, A. B., Ilchenko, V. S., Yu, N., Maleki, L., Millimeter and Submillimeter Waves and Workshop on Terahertz Technologies, 2007. The Sixth International Kharkov Symposium, 1, 79–84. With permission from IEEE.)

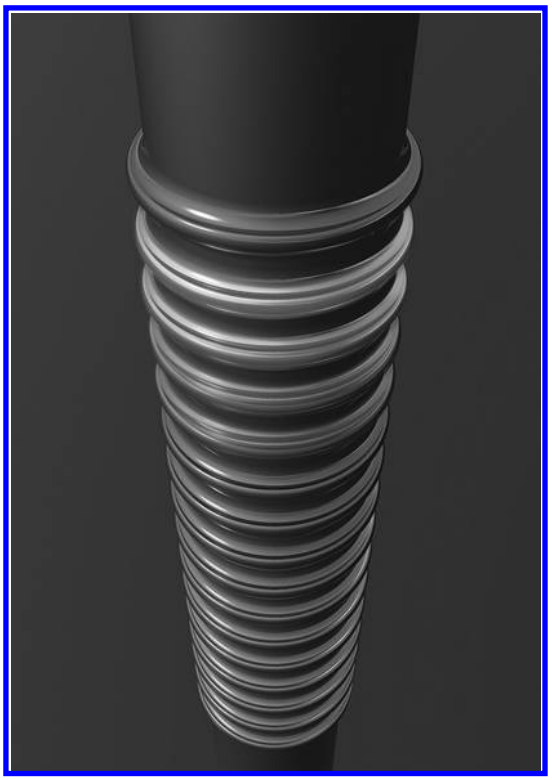

FIGURE 3.37
Schematic of the resonator waveguide. (Reprinted from Matsko, A. B., Savchenkov, A. A., and Maleki, L., *Opt. Lett*. 30, 3066–3068, 2005. With permission from OSA.)

the resonators that are within several microns of each other. The evanescent field of a resonator in the chain can be studied from the results of simulations made for the single-mode resonator (see Figure 3.13). The dimensions of the evanescent field inside the post exceed several micron. If several such resonators are placed close together on the same post, they will communicate through the "intrapost" evanescent field.

The propagation of light in the waveguide can be described with the usual wave Equation 3.16. We are interested in the case of high-order WGMs localized in the vicinity of the equator of the resonator. For the sake of simplicity we consider the TE mode family and change variables in Equation 3.16 as $E=\Psi e^{\pm im\phi}/\sqrt{r}$, m is the angular momentum number of the mode. We consider a low contrast structure, assuming that the resonator radius changes as $R=R_0+L(z)$ and $R_0 \gg |L(z)|$. Then Equation 3.16 is transformed to

$$\frac{\partial^2\Psi}{\partial r^2}+\frac{\partial^2\Psi}{\partial z^2}+\left[k^2\varepsilon\left(1+2\frac{L(z)}{R_0}\right)-\frac{m^2}{r^2}\right]\Psi=0, \tag{3.40}$$

where expressions $m \gg 1$ and $m^2 \simeq R_0^2 k^2 \varepsilon$ are used.

Considering an infinite waveguide, we separate variables and introduce $\Psi=\Psi_r\Psi_z$:

$$\frac{\partial^2\Psi_z}{\partial z^2}+2k^2\varepsilon\frac{L(z)}{R_0}\Psi_z=-k_z^2\Psi_z, \tag{3.41}$$

$$\frac{\partial^2 \Psi_r}{\partial r^2} + \left(k^2 \varepsilon - k_z^2 - \frac{m^2}{r^2} \right) \Psi_r = 0, \tag{3.42}$$

where k_z^2 is the separation parameter.

Equations 3.41 and 3.42 can be solved analytically if $L(z)$ is a periodic function with some period l. The solution is $\Psi = \Psi_0 e^{i,\beta z} \varphi(k_z z) J_v(k_{v,q} r)$, where β is a propagation constant, $J_v(k_{v,q} r)$ is a Bessel function, $\Psi_z = \exp(i\beta z)\varphi(k_z z)$ is the Bloch function $[\Psi_z(z+l) = \exp(i\beta l)\Psi_z(z)]$, $k_{v,q}$ is the radial wave number, and q describes radial quantization of the WGMs.

Parameters β and k_z are to be derived from Equation 3.41. They stand for wave number and a counterpart of frequency of the wave propagating in the resonator chain (the frequency is determined by eigenvalues of both Equations 3.41 and 3.42). The parameters are connected by a dispersion relation which, in the simplest case of periodic grating of cylindrical WGM resonators with gaps between them characterized by depth L_0 and length $l_g (l_g < l)$, can be presented as

$$\cos(\beta l) = \cosh\left[l_g \sqrt{2k^2 \varepsilon L_0 / R_0 - k_z^2} \right] \cos\left[k_z (l - l_g) \right] \tag{3.43}$$

$$+ \frac{k^2 \varepsilon L_0 / R_0 k_z}{\sqrt{2k^2 \varepsilon L_0 / R_0 - k_z^2}} \sinh\left[l_g \sqrt{2k^2 \varepsilon L_0 / R_0 - k_z^2} \right] \sin\left[k_z (l - l_g) \right],$$

where we assumed that $k(2\varepsilon L_0/R_0)^{1/2} > k_z$ (this assumption comes from the condition that a single localized WGM resonator has at least one confined mode). As follows from Equation 3.43 k_z is determined in allowed bands separated by forbidden band gaps (see in Figure 3.38).

Let us characterize the frequency spectrum of the entire system. We start from the expression for the frequency of WGMs derived from Equation 3.44.

$$\frac{\omega^2}{c^2} \varepsilon = k_{m,q}^2 + k_z^2. \tag{3.44}$$

In the case of small interaction between the resonators, when $k(2\varepsilon L_0/R_0)^{1/2} \gg k_z$ and $kl_g(2\varepsilon L_0/R_0)^{1/2} \gg 1$ we estimate from Equations 3.45 and 3.46 that each WGM mode in the resonator chain transforms to a frequency band with center.

$$\frac{\omega_c}{c} \sqrt{\varepsilon} \simeq k_{v,q} + \frac{1}{2k_{m,q}} \left[\frac{\pi p}{l - l_g} \right]^2 \tag{3.45}$$

and width

$$\frac{\Delta\omega}{c} \sqrt{\varepsilon} \simeq \frac{4\pi^2 p^2}{k_{m,q}^2 (l - l_g)^3} \sqrt{\frac{R_0}{2L_0}} \exp\left(-l_g k_{m,q} \sqrt{\frac{2L_0}{R_0}} \right). \tag{3.46}$$

The spectrum of the modes due to their radial confinement, being eigenvalues of Equation 3.42, is described by

$$k_{m,q} \simeq \frac{1}{R_0} \left[m + \alpha_q \left(\frac{m}{2} \right)^{1/3} - \sqrt{\frac{\varepsilon}{\varepsilon - 1}} \right], \tag{3.47}$$

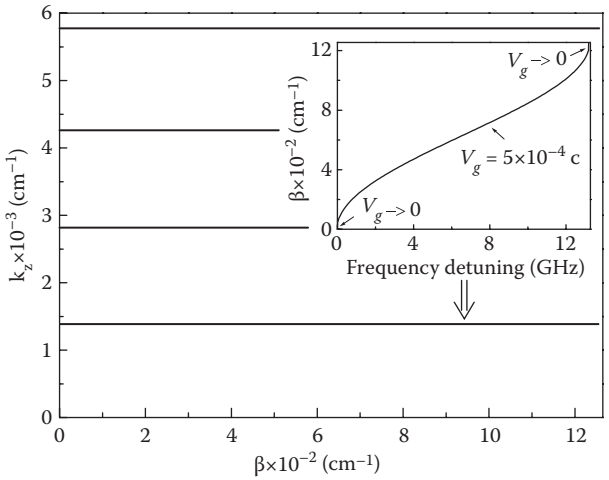

FIGURE 3.38
A solution of Equation 3.45 for period $l = 25$ μm ($l_g = 5$ μm), wavelength $\lambda = 1.5$ μm, radius $R_0 = 0.3$ cm, bump height $L_0 = 30$ μm, and $\varepsilon_0 = 2.2$. Inset: Structure of the first band evaluated using Equation 3.46. (Reprinted from Matsko, A. B., Savchenkov, A. A., and Maleki, L., *Opt. Lett.* 30, 3066–3068, 2005. With permission from OSA.)

where α_q is the q^{th} root of the Airy function, $Ai(-z)$ (q is a natural number). This is, in fact, a spectrum of high-order WGMs of an infinite cylinder with radius R_0. We now have all the necessary elements to describe the waveguide.

One of its parameters is the group velocity, which can be evaluated using wave number β(1.43) and frequency ω(1.44). First of all, even without calculation and using the analogy with photonic band-gap structures, it is clear that the group velocity of light propagating in the system, determined as $V_g = d\omega/d\beta$, approaches zero if light is tuned to the band edge. However, at that point the dispersion of the group velocity is also large, so such a tuning is impractical. The dispersion is nearly linear in the center of the band-gap and group velocity there can be estimated as

$$\frac{V_g\sqrt{\varepsilon}}{c} \approx \frac{\Delta\omega\sqrt{\varepsilon}l}{2\pi c} = \frac{2\pi p^2 l}{k_{m,q}^2 (l - l_g)^3}\sqrt{\frac{R_0}{2L_0}}\exp\left(-l_g k_{m,q}\sqrt{\frac{2M_0}{R_0}}\right). \tag{3.48}$$

It is easy to see that the group velocity decreases exponentially as the resonators are pulled apart, or the depth of trenches separating them increases. The result could be obtained even without analytically solving the problem. Indeed, because light propagates due to coupling between adjacent resonators, the smaller the coupling, the slower is the light propagation.

In reality, the resonator material possesses intrinsic losses due to scattering and surface inhomogeneities, as well as absorption. Because of these losses the modes have a finite ring-down time τ. The maximum group delay in the set of coupled resonators cannot exceed this ring-down time without a significant absorption of light. The minimum group velocity is then $V_{g\min} \approx l/2\pi\tau$, which corresponds to the propagation of light through a single uncoupled resonator. In the case of strong coupling between the resonators, when $\Delta\omega\pi \gg 2\pi$, light interacts with many resonators and its propagation can be studied using the formalism presented above.

Finally, we made numerical simulations of light propagation in a finite delay line made of WGM resonators and shown in (Figure 3.39, left). We assumed that initially light is confined in the bottom resonator. After that, we switch the interaction between the resonators and observe pulse propagation toward the top of the resonator stack, a subsequent reflection, and backwards propagation (Figure 3.39, right). The ring-down time τ was chosen to be 1 ms, which is theoretically achievable in calcium fluoride WGM resonators [159].

Comparing group velocity of light in this waveguide with that of CROWs [177], we conclude that, under equivalent conditions, our waveguide always results in a group velocity lower than the group velocity in CROWs. The ratio of the group velocities, approximately equal to the ratio of thickness and diameter of the resonator, can easily give an order of magnitude of difference.

3.6.10 Microwave Photonics Applications

Optical WGM resonators have successfully been used in microwave photonics. The resonators exhibit bandwidth in the hundred kilohertz to gigahertz range. In microwave photonics applications, this bandwidth corresponds to a wide range of equivalent radio-frequency Q-factors (between 10 and 10^6 for the X-band). This unique flexibility, in combination with a proper choice of highly transparent and/or nonlinear resonator material, allows development of a number of high performance microwave photonic devices: tunable and multi-pole filters, resonant electro-optic modulators, photonic microwave receivers, and opto-electronic microwave oscillators. In this section we focus on the applications of linear WGM resonators in an opto-electronic oscillator as well as in a photonic microwave receiver.

3.6.10.1 Opto-Electronic Oscillator

The opto-electronic oscillator (OEO) produces microwave signals using optical techniques [180]. The generic scheme of the OEO is shown in Figure 3.40a. The conventional OEO consists of a laser as the source of light energy. The laser radiation propagates through an electro-optical modulator and an optical energy storage element, before it is converted to the electrical energy with a photodetector. The electrical signal at the output of the photodetector is amplified and filtered before it is fed back to the modulator, thereby completing a feedback loop with gain that generates sustained oscillation at a frequency determined by the filter. An OEO with a high-Q optical resonator in place of the electronic filter was

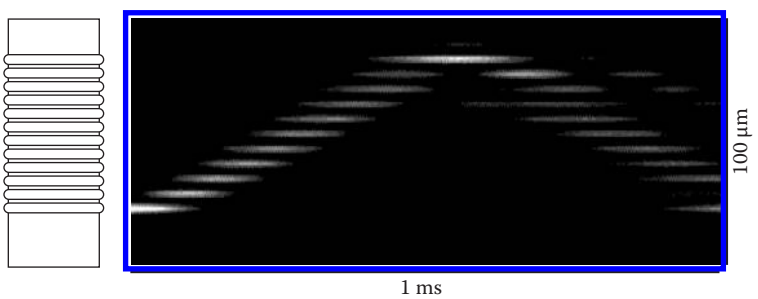

FIGURE 3.39
Left: A set of coupled WGM rings placed on a single rod. Right: A map obtained with 2D numerical simulations describing ultra-slow propagation of an optical pulse. The group velocity is less than 20 cm/s. (Reprinted from Matsko, A. B., Savchenkov, A. A., and Maleki, L., *Opt. Lett.* 30, 3066–3068, 2005. With permission from OSA.)

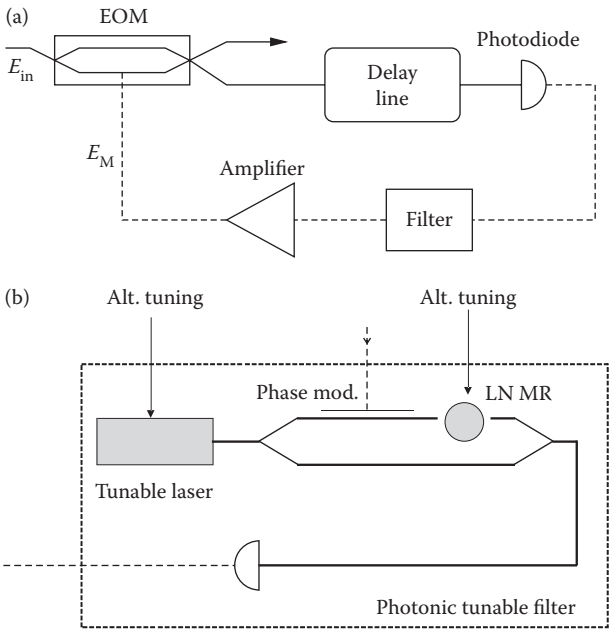

FIGURE 3.40
(a) Generalized scheme of an OEO. (b) A tunable microwave photonic filter that includes a lithium niobate WGM resonator.

studied theoretically by Strekalov et al. [181]. An OEO with a lithium niobate WGM modulator was demonstrated by Matsko et al. [182].

The fundamental noise performance of an OEO is determined by the energy storage time, or quality factor Q, of the optical storage element. Q-factor can be very large. A long fiber delay can easily have several microsecond long storage times, corresponding to the equivalent microwave Q of about a million at 10 GHz frequency. This is a high value compared to conventional dielectric microwave resonators used in oscillators. A high-Q optical resonator can play the role of the optical storage element, in addition to the role of the electronic filter. While an optical fiber is a true time delay and introduces group as well as phase delays. An optical resonator produces group delay only, and phase delay of the microwave signals due to these resonant elements is negligibly small.

We have made an OEO with a tunable microwave photonic filter as shown in Figure 3.40b. The OEO includes a DFB laser and 130 m delay line. The photonic filter has a tunable first-order pass band shown in Figure 3.41, left. As a result of the filter tunability we have achieved a smooth tuning of the oscillation frequency in the 8–9 GHz range, without degradation of the performance of the device Figure 3.41, right.

We also demonstrated an OEO with a lithium niobate WGM filter inserted into the optical loop Figure 3.42, left. The filter is used to suppress generation of spurious modes in the OEO loop. The noise power spectrum of the oscillator is shown in Figure 3.42, right.

3.6.10.2 Microwave Photonic Receivers

To demonstrate the filter performance in a photonic microwave receiver, we configured it for transmission of a video signal [160]. This type of narrowband signal link may be important for the development of portable navigation and communication devices

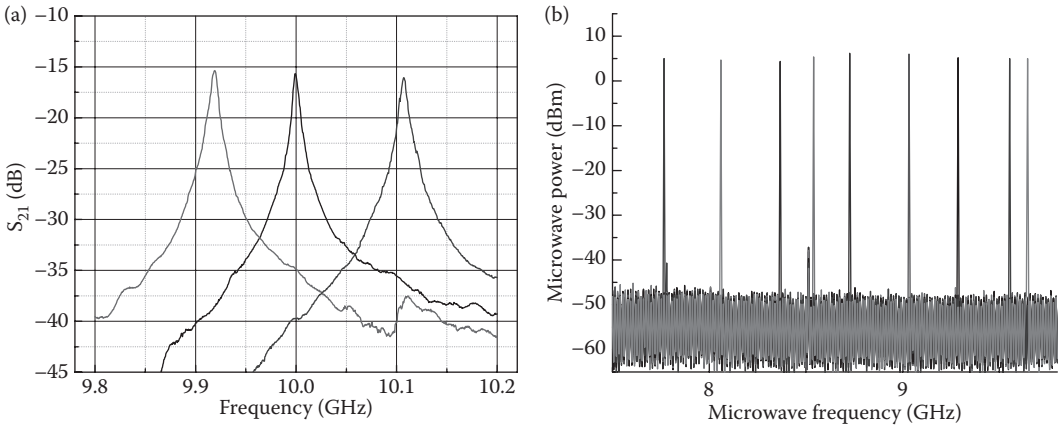

FIGURE 3.41
Left: Tunable 11 MHz photonic filter. Right: Demonstration of the frequency shift of the OEO.

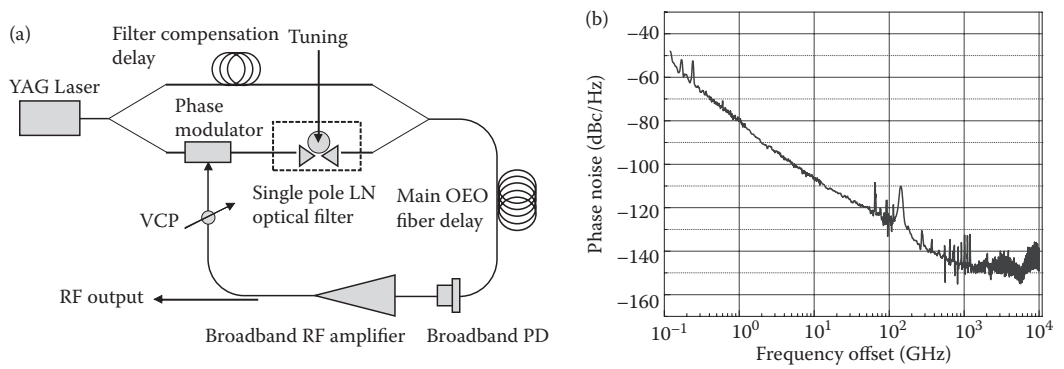

FIGURE 3.42
Left: Scheme of the OEO with optical WGM filter in the optical part of the oscillator. Right: Phase noise of the photonic oscillator with optical power −6 dBm and WGM resonator quality factor 2×10^8.

at microwave and millimeter-wave frequencies. For example, such a photonic architecture allows architecting a single platform for systems requiring operation in RF through millimeter-wave. These systems currently require multiple sets of hardware if implemented using all electronics schemes.

The scheme of the transmission experiment is shown in Figure 3.43. A video signal with approximately 20 MHz FWHM bandwidth and zero carrier frequency was sent from a CCD camera to a mixer, where it was mixed with a 10 GHz microwave carrier. The resultant modulated microwave signal was transmitted to a microwave receiver, filtered to suppress higher harmonics, amplified, and upconverted into light using a Mach-Zehnder electro-optic modulator. The modulated signal was then sent through the photonic filter, heterodyned and detected with a fast photodiode. The microwave signal from the photodiode output was mixed with a microwave carrier to restore the initial signal.

A high-Q WGM cavity may mix the amplitude and phase fluctuations of the light. The amplitude of the transmitted light through the filter may be presented as

$$E_{\text{out}}(t) \approx \frac{\tilde{E}_{\text{in}}(t-\tau_d)e^{-i\omega t}\gamma}{\gamma + i(\omega - \omega_0 + \dot{\phi}_{\text{in}}(t))}, \tag{3.49}$$

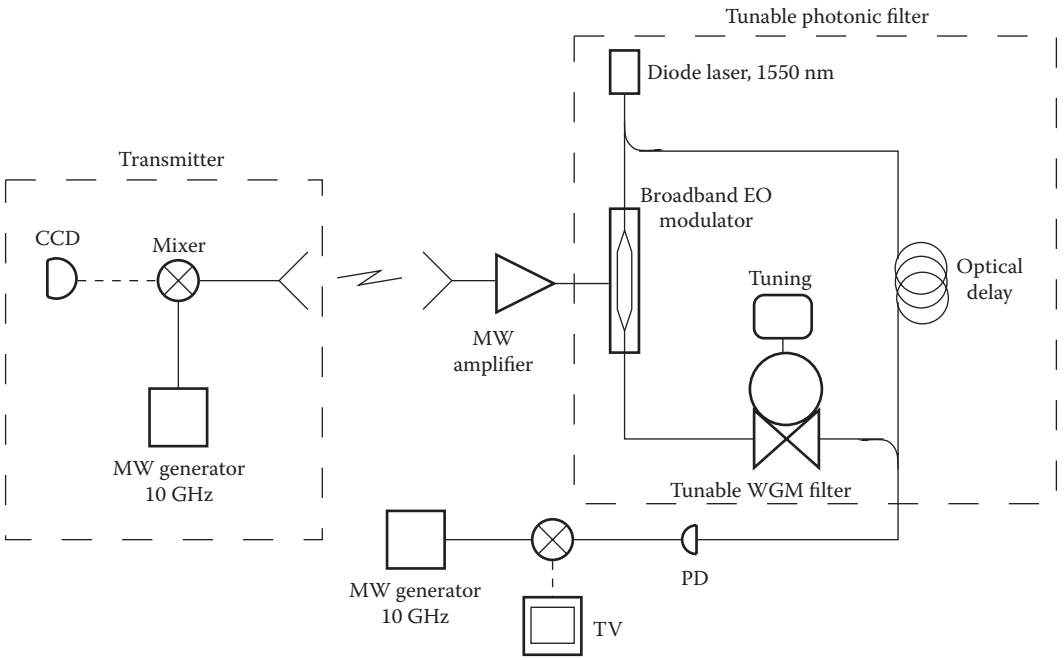

FIGURE 3.43
Schematic diagram of the video signal transmission experiment. The solid thin line corresponds to optical fibers, solid thick lines to microwave waveguides, and dashed lines to electric circuits. (Reprinted from Ilchenko, V. S., Savchenkov, A. A., Matsko, A. B., and Maleki, L., *Proc. SPIE* 4969, 195–206, 2003. With permission from Society of Optical Engineers (SPIE).)

where $\widetilde{E_{\text{in}}}(t-\tau_d)$ is the slow field amplitude, τ_d stands for the group delay, $\dot{\phi}_{\text{in}}(t)$ results from the phase diffusion of the pump laser. The filter works well when the phase diffusion of the pump laser is small $\gamma \gg \dot{\phi}_{\text{in}}(t)$; it transforms the phase fluctuations of the laser into the amplitude fluctuations for large phase diffusion.

It is important to note that to characterize and retrieve encoded information, the filter output should be mixed with a monochromatic light on a photodetector. The filter contains a high-Q cavity that introduces group delay τ_d into the signal. This group delay results in an additional source of frequency-to-amplitude noise conversion when the output signal from the filter is mixed with the light that did not pass through the filter. This happens unless the scheme is balanced. We inserted the filter into a Mach-Zehnder configuration with a fiber delay line L_f to compensate for the group delay. The delay line length was equal to $L_f = n_o dF/2n_f = 1.2$ m , where $n_f \simeq 1.5$ is the refractive index of the fiber material and $F = 300$ is the cavity finesse. Such a compensation is not required if the laser linewidth is much smaller than the width of the cavity resonance. In our case optical characterization of the filter was achieved using a semiconductor diode laser with a 30 MHz FWHM line, which is quite large. The laser power in the fiber was approximately 2.5 mW.

3.7 Frequency Stability of WGM Resonators

Ultrastable optical resonators play an important role in both classical and quantum optics, and generally are of FP type. They are fabricated from materials having ultra low thermal

expansion coefficients, and are both thermally and mechanically isolated to achieve stability. The geometrical dimensions of this type of resonator is typically about 10 cm or larger. Lasers locked to these resonators demonstrate Hertz and even subHertz linewidth, with frequency stabilities as high as $\sim 10^{-15}$ at 1 s.

WGM resonators can also be used as frequency etalons [183,184]. The basic advantages of WGM resonators compared with FP ones are: (i) the small size; (ii) a large wavelength range in which WGM resonators have high Q-factor; and (iii) the low sensitivity of WGM resonators to external mechanical noise. This latter property is the result of the unique orthogonality relations between optical and acoustical WGM modes, in addition to high-Q factors and low density of the WGM spectra. All these features make utilization of the WGM resonators attractive in place of FP resonators for a laser stabilization applications.

On the other hand, WGM resonators also have several disadvantages compared with FP resonators. (i) Reference FP resonators contain a specific mirror spacer material which has a low thermal expansion coefficient. WGM resonators cannot contain such a material. The polished rim surface of the WGM resonator plays the role of the resonator mirrors and the host material is the only resonator "mirror spacer" material possible. Such a material generally has a large thermal coefficient of expansion. This problem can be mediated by efficient thermal isolation of the resonator, which is simpler than the isolation of FP resonators because of the small size and structure rigidity of the WGM resonators. (ii) Reference FP resonators are empty, usually evacuated, and are comparably large. These properties reduce the fundamental thermodynamic fluctuations, which are important even if the resonator is kept at a constant temperature. WGM resonators are small and material-filled, and hence suffer more strongly from the thermodynamic fluctuations [185]. The fluctuations can be partially suppressed by passive and active frequency stabilization schemes. (iii) The optical nonlinearity of WGM resonators is much larger than the nonlinearity of FP resonators, because of the same reasons as indicated in the previous item. The circulating optical power level should be limited in a WGM resonator to mediate this problem. The power fluctuations of a laser interrogating the resonator should also be small.

The goal of this section, based on the materials published in [183,184], is elucidating the properties of WGM frequency fluctuations, resulting from the basic fundamental thermodynamic as well as quantum optic principles. We evaluate the frequency spectra of thermorefractive, thermal expansion, and thermoelastic fluctuations, together with the steady state WGM frequency uncertainty resulting from those fluctuations. We also study the photothermal and ponderomotive fluctuations originating from the measurement procedure and find their frequency spectra.

The stability of a passively stabilized millimeter-sized WGM resonator made of a certain class of crystalline materials is primarily determined by thermorefractive fluctuations [183]. Those fluctuations have been predicted and successfully observed in fused silica microspheres [185]. The frequency stability limit of a cylindrical WGM resonator having a thickness of one hundred microns and a diameter of several millimeters is on the order of one part in 10^{-12} at one second integration time [183]. Thermorefractive fluctuations increase inversely proportional to the mode volume, and the predicted stability is limited because of small volumes of the WGMs.

It was shown, however, that a proper selection of the resonator host material is essential for stabilization of the WGM frequency [184]. Photorefractive fluctuations can be suppressed in some materials like magnesium fluoride if the proper operation temperature is selected. But in those resonators thermal expansion fluctuations become dominant in the frequency stability limit. It is possible to design active schemes to further stabilize fluctuations that result from the residual thermal expansion, using specific thermal expansion

properties of some crystals that are not homogeneous along different crystal axes. In this way, the achieved frequency stability could be higher than the stability determined by the fundamental thermodynamic limit.

We also discuss some methods for achieving the desired frequency stability. The simple passive temperature stabilization is not practical because it must sustain fluctuations smaller than submicroKelvin level. To solve this problem we make use of methods similar to technologies developed for the stabilization of quartz crystalline rf oscillators [186]. The scheme includes (i) compensation of the temperature drifts of the resonator by connecting it with special elements having appropriate linear or nonlinear thermal expansion (c.f. oven controlled crystal radio frequency oscillator) and (ii) usage of two WGM families having different thermo-optical constants for measurement and compensation of the resonator temperature fluctuations. These methods can be very efficient. It will be argued that the relative stability of two modes in the same resonator separated by an octave can be better than one part in 10^{-14}, at one second integration time.

3.7.1 Fundamental Thermodynamic Limits

In this section, we consider two types of resonators. We initially assume that a WGM resonator can be considered as a small part of a much larger object, so the thermal spectrum is continuous. This assumption is valid, for instance, for a low contrast resonator [53] or for a resonator being in good contact with the heat bath. The validity of the assumption is even more general. It was shown by Gorodetsky and Grudinin [185] that it is possible to neglect the discreteness of the spectrum of the thermal waves in a sufficiently large spherical resonator (radius exceeding several tens of microns) because the mode volume is small compared with the volume of the resonator. To confirm that conclusion, we also consider a thin resonator, so the discrete thermal spectrum would be studied. We show that the resonators with both discrete and continuous thermal spectra possess equivalent frequency fluctuations.

As a general rule, the relative uncertainty of the eigen frequency of WGMs can be found from the expression

$$\frac{\delta\omega}{\omega} = \frac{\Delta R}{R} + \frac{\Delta n}{n}, \tag{3.50}$$

where ω is the mean value of the frequency of a selected mode, $\delta\omega$ is the fluctuation of the frequency, R and ΔR are the values of the radius of the resonator and its fluctuation, n and Δn are the values of the index of refraction of the material of the resonator and its fluctuation. Equation 3.50 is valid for a WGM resonator of any relevant shape if the radius of the resonator determines the largest dimension of the geometrical localization of the mode, i.e. where $\omega_{WGM} \simeq cm/(Rn)$, where $m \gg 1$ is the azimuthal mode number.

The terms $\Delta R/R$ and $\Delta n/n$ in Equation 3.50 are responsible for thermoelastic/thermal expansion and thermorefractive noise, respectively. Both terms are of the same order and they both should be taken into account in crystalline WGM resonators.

3.7.1.1 Thermorefractive Fluctuations: Steady State

Thermodynamic fluctuation of temperature in the WGM volume results in fluctuations of the index of refraction in the WGM channel

$$\left.\frac{\Delta n}{n}\right|_{(\Delta T)_m} = \alpha_n (\Delta T)_m, \tag{3.51}$$

where $\alpha_n=(1/n)(\partial n/\partial T)$ is the thermo-refractive coefficient of the resonator host material. The mean square value of the thermal fluctuation is

$$\langle(\Delta T)_m^2\rangle=\frac{k_BT^2}{C_pV_m\rho}, \tag{3.52}$$

where k_B is the Boltzmann's constant, T is the absolute temperature, ρ is the density of the resonator host material, V_m is the mode volume (assumed to be much less than the volume of the resonator), C_p is the specific heat capacity at constant pressure of the resonator host material. In what follows we assume that $C_p=C_V=C$ for a crystalline material. The mode volume of a WGM belonging to the basic mode sequence of a spherical resonator is

$$V_m=3.4\pi^{3/2}\left(\frac{\lambda}{2\pi n}\right)^{7/6}R^{11/6}, \tag{3.53}$$

The value of the mode volume of a toroidal/cylindrical WGM resonator varies depending on the resonator thickness and can exceed the value for the spherical resonator.

3.7.1.2 Thermorefractive Fluctuations: Spectrum

The frequency spectrum of thermorefractive fluctuations can be found following the path described by Gorodetsky and Grudinin [185]. The complex temperature distribution u in the resonator is given by the heat transport equation containing a distributed external fluctuational thermal source [187]

$$\frac{\partial u}{\partial t}-D\Delta u=F(\mathbf{r},t), \tag{3.54}$$

where $D=\kappa/(\rho C)$, κ is the thermal conductivity coefficient, and C is the specific heat capacity. The thermal source is normalized such that the quadratic deviation of the mode temperature coincides with Equation 3.52.

We are interested in the temperature fluctuations averaged over the mode volume

$$\bar{u}(t)=\int u(\mathbf{r},t)\,|\,\Psi(\mathbf{r})\,|^2\,d\mathbf{r}, \tag{3.55}$$

where $|\Psi(\mathbf{r})|^2$ is the normalized spatial power distribution for the light localized in a WGM, $\int|\Psi(\mathbf{r})|^2\,d\mathbf{r}=1$.

The spectral power density of the random process $\bar{u}(t)$ and the quadratic deviation of the average mode temperature $\langle\bar{u}(0)^2\rangle$ are given by

$$S_{\bar{u}}(\Omega)=\int_{-\infty}^{\infty}\langle\bar{u}^*(t)\bar{u}(t+\tau)\rangle e^{-i\Omega\tau}d\tau, \tag{3.56}$$

$$\left\langle(\Delta T)_m^2\right\rangle=\left\langle\bar{u}(0)^2\right\rangle=\int_{-\infty}^{\infty}S_{\bar{u}}(\Omega)\frac{d\Omega}{2\pi}. \tag{3.57}$$

Let us consider a resonator formed on the surface of an infinitely long cylinder of radius R by a cylindrical protrusion of radius $R+\Delta R$ ($R \gg \Delta R$) and thickness L. We solve Equation 3.54 and numerically evaluate the spectral density for a calcium fluoride resonator with $R=0.3$ cm and $L=0.01$ cm (see Figure 3.44, left)).

We also find the fluctuations for a thin cylindrical resonator of thickness L and radius R, $R \gg L$. A simple analytical approximation is possible in this case. We present the correlation of the fluctuation forces as

$$\langle F(\mathbf{r},t)F(\mathbf{r}',t')\rangle \simeq 16\pi \frac{k_B T^2 DL}{\rho C V_m}\delta(\mathbf{r}-\mathbf{r}')\delta(t-t'); \tag{3.58}$$

solving Equation 3.54, we derive an approximate expression for the spectral density of the thermorefractive noise

$$S_{\bar{u}}(\Omega) = \frac{k_B T^2}{\rho C V_m}\frac{R^2}{12D}\left[1+\left(\frac{R^2}{D}\frac{|\Omega|}{9\sqrt{3}}\right)^{3/2}+\frac{1}{6}\left(\frac{R^2}{D}\frac{\Omega}{8m^{1/3}}\right)^2\right]^{-1}. \tag{3.59}$$

The spectral density of the frequency noise, given by $S_{\delta\omega/\omega}(\Omega)=\alpha_n^2 S_{\bar{u}}(\Omega)$, is approximately the same for the case of a thin resonator and for a resonator being a part of an infinite cylinder (Figure 3.44 left).

We consider a calcium fluoride resonator of radius $R=0.3$ cm and thickness $L=0.01$ cm driven with $\lambda=1.55$ μm light. We find $m \simeq 2\pi Rn/\lambda \approx 2.7\times10^4$ and $R/m^{2/3} \simeq 1.1\times10^{-3}$. The thermal diffusivity for CaF_2 is equal to $D=3.6\times10^{-2}$ cm^2/s, hence characteristic frequencies for the process are $D/R^2=0.4$ s^{-1}, $Dm^{4/3}/R^2=3.2\times10^5$ s^{-1}, and $D/L^2=360$ s^{-1}. To find the factor $k_B\alpha_n^2T^2/\rho CV_m \simeq 4\times10^{-24}$ we have taken $\alpha_n=-0.8\times10^{-5}$ K^{-1}, and $V_m=2\pi RL\times R/m^{2/3}\simeq 6\times10^{-6}$ cm^3.

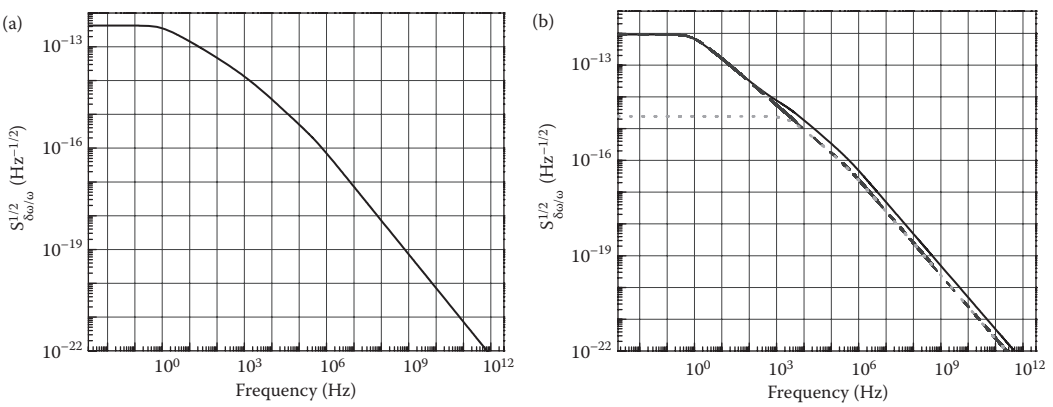

FIGURE 3.44
Left: Spectral density for a calcium fluoride resonator with $R=0.3$ cm and $L=0.01$ cm. The resonator is formed on the surface of an infinitely long cylinder of radius R by a cylindrical protrusion of radius $R+\Delta R$ ($R \gg \Delta R$) and thickness L. Right: The fluctuations for a thin cylindrical resonator of thickness L and radius R, $R \gg L$. (Reprinted from Matsko, A. B., Savchenkov, A. A., Yu, N., and Maleki, L., *J. Opt. Soc. Am. B* 24, 1324–1335, 2007. With permission from OSA.)

We find the Allan variance of the WGM frequency by integrating the evaluated spectral density of fluctuations using the expression from Audoin [188]

$$\sigma^2(\tau) = \frac{2}{\pi}\int_0^\infty S_{\delta\omega/\omega}(\Omega)\frac{\sin^4(\Omega\tau/2)}{(\Omega\tau/2)^2}d\Omega, \tag{3.60}$$

where we took into account that $S_{\delta\omega/\omega}(\Omega)$ is a double sided spectral density. The evaluated Allan variance for the resonator is shown in Figure 3.45. To understand the change of slope of the dependence shown in Figure 3.45 we note that integration (averaging) in Equation 3.60 occurs in the vicinity of $\Omega=0$ when $\tau\to\infty$, where spectral density is approximately constant and $\sigma^2(\tau)\sim 1/\tau$. In the case of $\tau\to 0$ the integration in Equation 3.60 occurs in a wide band centered at frequency $\Omega\to\infty$, so that $S_{\delta\omega/\omega}(\Omega)\sim 1/\Omega^2$ and $\sigma^2(\tau)\sim 1/\tau$. The monotonic function $\sigma^2(\tau)$ naturally has a maximum at some specific value of τ. The increase of Allan variance with time for small τ is not counterintuitive because the thermorefractive fluctuations result in thermal drift of the WGM frequency. The maximum value of the drift is restricted and longer integration results in averaging down of the fluctuations.

An advantage of crystalline WGM resonators compared with other solid state resonators is that WGM resonators can be made out of various materials with various thermorefractive constants. For instance, it is important to mention the unique properties of MgF_2. This crystal has vanishing extraordinary (at ~74°C) and ordinary (at ~176°C) thermorefractive coefficients [189]. Tuning the temperature of a MgF_2 WGM resonator to the vicinity of zero thermorefractive coefficient $\alpha_n=0$ allows suppression of the fundamental thermorefractive noise $\langle(\Delta\omega_{TR})^2\rangle^{1/2}/\omega\to 0$. Technical thermorefractive noise is also compensated because temperature stability on the order of 2 mK required to reach $\Delta n_e/n_e=10^{-14}$ is feasible.

The basic conclusion of this section is that the thermorefractive noise does not limit the stability of WGM resonators made out of certain materials, even with moderate temperature stabilization and no sophisticated compensation. However, the other noise sources have to be dealt with to reach higher stability.

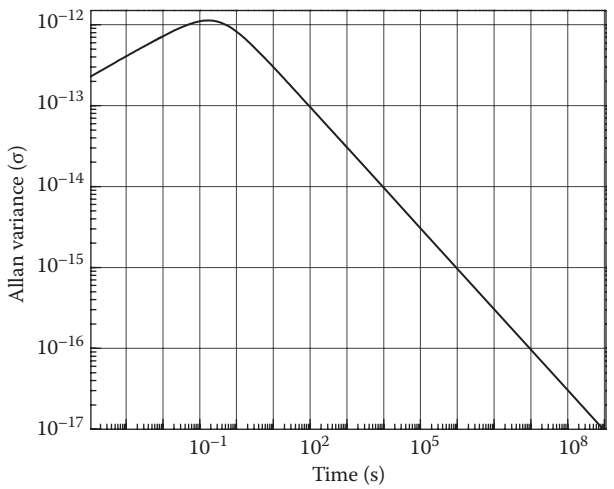

FIGURE 3.45
Thermorefractive Allan variance of the frequency of a mode of a cylindrical calcium fluoride WGM resonator with R = 0.3 cm and L = 0.01 cm. (Reprinted from Savchenkov, A. A., Matsko, A. B., Ilchenko, V. S., Yu, N., and Maleki, L., *J. Opt. Soc. Am. B* 24, 2988–2997, 2007. With permission from OSA.)

3.7.1.3 Thermoelastic and Thermal Expansion Fluctuations: Steady State

The variations of the mode volume of a WGM due to fundamental thermoelastic fluctuations do not change the WGM frequency. The frequency is given by the boundary conditions of the resonator and by the size of its radius. The fluctuation of the radius is determined by the fluctuation of the volume and the temperature of the entire resonator. To use the thermodynamic approach we assume that the resonator is a small part of a much larger sample. This is possible if the resonator is a thin disc cut on a solid state rod. Then the volume of the resonator V_r fluctuates as

$$\frac{\langle(\Delta V_r)^2\rangle}{V_r^2} = k_B T \frac{\beta_T}{V_r}, \tag{3.61}$$

and $\beta_T = -[(1/V)\,(\partial V/\partial p)]_T$ is the isothermal compressibility of the resonator host material. Fluctuation of the radius of a spherical resonator due to fluctuations of its volume is

$$\left.\frac{\Delta R}{R}\right|_{\Delta V} = \frac{\Delta V_r}{3V_r}. \tag{3.62}$$

Fluctuation of the average resonator temperature

$$\langle(\Delta T)_r^2\rangle = \frac{k_B T^2}{C_p V_r \rho}, \tag{3.63}$$

influences the radius as well:

$$\left.\frac{\Delta R}{R}\right|_{\Delta T} = \alpha_l (\Delta T)_r, \tag{3.64}$$

where $\alpha_l = (1/l)\,(\partial l/\partial T)$ is the linear thermal expansion coefficient.

Using the fact that fluctuations $(\Delta V)_r$ and $(\Delta T)_r$ are statistically independent, and that the correlation of fluctuations of the temperature of the whole resonator and the average temperature in the WGM localization, $(\Delta T)_r$ and $(\Delta T)_m$, respectively, is small (mode volume is much smaller than the volume of the resonator) we arrive at

$$\frac{\langle(\Delta R)^2\rangle}{R^2} = k_B T \frac{\beta_T}{9V_r} + \alpha_l^2 \frac{k_B T^2}{C_p V_r \rho}. \tag{3.65}$$

It is important to note that the noise depends on the shape of the resonator. For instance, the thermoelastic fluctuations of a thin cylindrical resonator mounted on a thin stem should be considered in a different way compared with the above derivation. The above estimate is valid only if there is at least one continuous (quasi-continuous) dimension in the system, for instance, if the resonator is formed by a small protrusion on a long cylindric rod.

3.7.1.4 Thermoelastic Fluctuations: Spectrum

Let us find the spectral density of the frequency noise determined by the thermoelastic fluctuations. For the sake of simplicity we consider only one effective 1D elastic mode of

the resonator of the lowest order. The contributions from other modes of higher order is comparably small. We assume that in the vicinity of the WGM localization the radius of the resonator changes in accordance with

$$\frac{\partial(\Delta R)}{\partial t} + (-i\Omega_0 + \Gamma_0)\Delta R = F_R(t), \tag{3.66}$$

where the oscillation frequency is taken to be equal to the eigenfrequency of the lowest order radial mode of a spherical liquid resonator of radius R

$$\Omega_0 = \frac{\pi v_s}{R}, \tag{3.67}$$

where v_s is the speed of sound. The decay rate of the acoustic mode can be very small. The minimal value of the rate is thermodynamically limited [190]

$$\Gamma_0 \geq \frac{\Omega_0^2 \kappa T \alpha_l^2 \rho}{9C^2}. \tag{3.68}$$

This is a very small value. The realistic value of the quality factor ($\Omega_0/2\Gamma_0$) of the acoustic mode is expected to exceed 5×10^4 [191].

We select the fluctuational force $F_R(t)$ such that it obeys

$$\langle F_R^*(t)F_R(t')\rangle = \Gamma_0 k_B T \frac{\beta_T R^2}{9V_r}\delta(t-t'); \tag{3.69}$$

and obtain an expression for the spectral density of the radius fluctuation:

$$S_{\Delta R/R} = k_B T \frac{\beta_T}{9V_r}\frac{\Gamma_0}{(\Omega-\Omega_0)^2+\Gamma_0^2}. \tag{3.70}$$

The density is peaked at Ω_0 and is significantly suppressed at higher frequencies. For example, for a cylindrical resonator with $R=0.3$ cm, $L=0.01$ cm, and $v_s=5\times10^5$ cm/s we have $\Omega_0=5\times10^6$ rad/s. Assuming that $\Gamma_0=100$ rad/s we obtain Figure 3.46. It is easy to see that the low frequency branch of the spectral power density of the frequency noise given by the thermoelastic fluctuations ($S_{\delta\omega/\omega}=S_{\Delta R/R}$) is much smaller than the one due to thermorefractive fluctuations.

3.7.1.5 Thermal Expansion Fluctuations: Spectrum

Thermodynamic temperature fluctuations of the resonator result in the modification of the resonator radius and thickness, leading to frequency noise. To estimate this noise we assume that the basic contribution comes from the lowest order eigenfunction of the thermal diffusion equation. Using the reasoning of [183] for the noise spectral density we derive

$$S_{\Delta R/R} = \frac{\langle(\Delta\omega_{TE1})^2\rangle}{\omega^2}\frac{2R^2/\pi^2 D}{1+(\Omega R^2/D\pi^2)^2}. \tag{3.71}$$

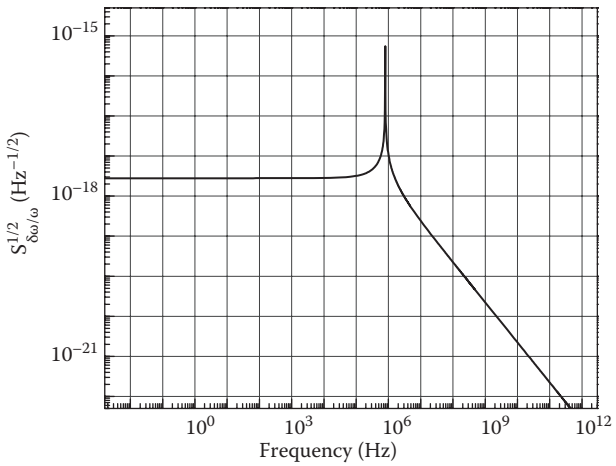

FIGURE 3.46
The spectral density of the frequency noise $S_{\delta\omega/\omega}(\Omega)=S_{\Delta R/R}(\Omega)$ due thermoelastic noise. (Reprinted from Matsko, A. B., Savchenkov, A. A., Yu, N., and Maleki, L., *J. Opt. Soc. Am. B* 24, 1324–1335, 2007. With permission from OSA.)

This expression basically tells us that the frequency dependence of the spectral density is determined by the slowest thermal diffusion time associated with the thermal diffusion along the radius of the resonator. Using Equation 3.60 we calculate the Allan variance of the frequency of the WGM resulting from the fundamental thermal expansion fluctuations of a z-cut magnesium fluoride resonator of radius $R=0.3$ cm and thickness $L=0.01$ cm (Figure 3.47). The thermal diffusivity for MgF_2 is equal to $D=7.2\times10^{-2}$ cm^2/s and the characteristic frequency for the process is $D/R^2=0.8$ s^{-1}. Equation 3.71 gives the top boundary of the low frequency spectral density.

In reality, the resonator can be placed on a metal plate possessing a high thermal conductivity, so eventually the time constant R^2/π^2D should be replaced with L^2/π^2D; this would reduce the value of the low frequency spectral density significantly. For example, the thermal diffusivity of aluminium is $D=0.97$ cm^2/s at 300 K. Copper has a bit larger value: $D=1.15$ cm^2/s at 300 K. Placing the resonator on a polished copper plate (or squeezing the resonator between two copper plates) would result in more than an order of magnitude reduction of phase noise at zero frequency, leading to a reduction of the corresponding Allan variance below one part in 10^{-14} at one second integration time. It is important to note that placing a resonator onto a copper plate will reduce the quality factor of the mechanical modes of the resonator. This reduction will lead to an enhancement of the influence of thermoelastic fluctuations on the frequency stability.

We find the solution to the problem in the optimal shaping of the resonator allowing to increase the resonator volume without changing the characteristic time constant of the process. The resonator should have a nearly spherical shape, or the shape of a cylinder with equal radius and height. The light should travel in a small protrusion [53] that does not influence the thermal and mechanical modes of the resonator. For instance, a nearly spherical single mode MgF_2 WGM resonator of radius $R=0.3$ cm will have an Allan variance less than one part per 10^{-14} at one second integration time. This improvement will not increase the thermoelastic fluctuations.

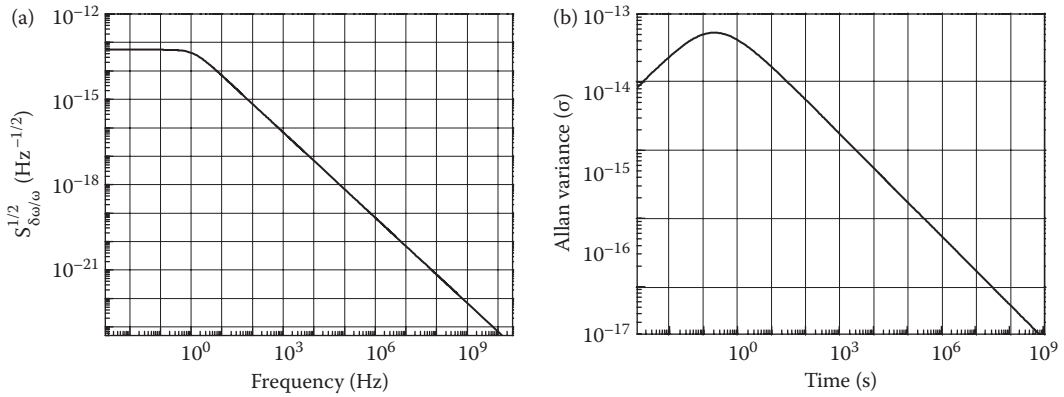

FIGURE 3.47
Power spectral density and Allan variance of the thermal expansion defined frequency fluctuations of a mode of a cylindrical magnesium fluoride WGM resonator with $R = 0.3$ cm and $L = 0.01$ cm. (Reprinted from Savchenkov, A. A., Matsko, A. B., Ilchenko, V. S., Yu, N., and Maleki, L., *J. Opt. Soc. Am. B* 24, 2988–2997, 2007. With permission from OSA.)

3.7.2 Fluctuations Originating from the Measurement Procedure

In this section, we consider fluctuations of the WGM frequency arising from the measurement procedure. The resonator is interrogated with laser radiation. Shot noise of the radiation causes two additional types of fluctuations: photothermal [187,192] and optoelastic [193].

3.7.2.1 Photothermal Fluctuations

These fluctuations appear as a result of the transfer of the shot noise of light absorbed in the resonator to the temperature fluctuations of the resonator host material, and to the subsequent fluctuations of the index of refraction of the resonator.

The temperature distribution in the resonator is described by the equation

$$\frac{\partial u}{\partial t} - D\Delta u = F_P(\mathbf{r}, t), \tag{3.72}$$

where $F_p(\mathbf{r}, t)$ is the fluctuational force describing noise due to the absorption of the photons in the resonator

$$\langle F_P(\mathbf{r},t)F_P(\mathbf{r}',t')\rangle = \frac{\hbar\omega_{m,q,p}}{\rho^2 C^2}\langle P_{\text{abs}}\rangle |\Psi(\mathbf{r})|^2\, \delta(\mathbf{r}-\mathbf{r}')\delta(t-t'), \tag{3.73}$$

$\omega_{m,q,p}$ is the angular frequency of the corresponding WGM, $\langle P_{\text{abs}}\rangle$ is the expectation value for the absorbed power, $|\Psi(\mathbf{r})|^2$ is the power distribution in a WGM ($\int |\Psi(\mathbf{r})|^2 d\mathbf{r} = 1$).

We find that the spectral density of the temperature fluctuations can be approximated by

$$S_{\bar{u}}(\Omega) \approx \frac{\hbar\omega_{m,q,p}}{\rho^2 C^2}\frac{\langle P_{\text{abs}}\rangle}{V_r^2}\frac{\pi^6 R^{3/2}/64L^{3/2}}{\Omega^2 + \pi^6 D^2/16L^3 R}. \tag{3.74}$$

A comparison of the exact numerical simulation and the approximation of the spectral density is presented in Figure 3.48.

3.7.2.2 Ponderomotive Fluctuations

Optoelastic ponderomotive fluctuations occur as a result of the fluctuations of the radiation pressure induced by light propagating inside the resonator [190,194]. The integral value of the pressure induced force is $F=2\pi P/c$, where P is the power of the light inside the resonator. The force changes the resonator radius as well as the index of refraction. The index of refraction is involved due to the mechanical strain of the resonator host material:

$$\frac{\delta\omega}{\omega}=\left[1+\frac{1}{2}K_{\varepsilon}\right]\frac{\Delta R}{R}, \tag{3.75}$$

where factor $K_{\varepsilon}=-E\varepsilon^{-1}\partial\varepsilon/\partial p$ ranges from 1 to 10 [190], E is Young's modulus of the material, and $\varepsilon=n^2$ is the electric susceptibility of the material.

For the sake of simplicity we take into account only one mechanical mode having the lowest mechanical frequency and assume that the probe light is resonant with the corresponding WGM. The last condition is required to avoid mechanical instability or additional rigidity added to the mechanical system by light. The mechanical oscillations of the resonator surface are described by the equation

$$\frac{\partial^2(\Delta R)}{\partial t^2}+\Gamma_0\frac{\partial(\Delta R)}{\partial t}+\Omega_0^2(\Delta R)=\frac{2\pi\delta P(t)}{m^* c}, \tag{3.76}$$

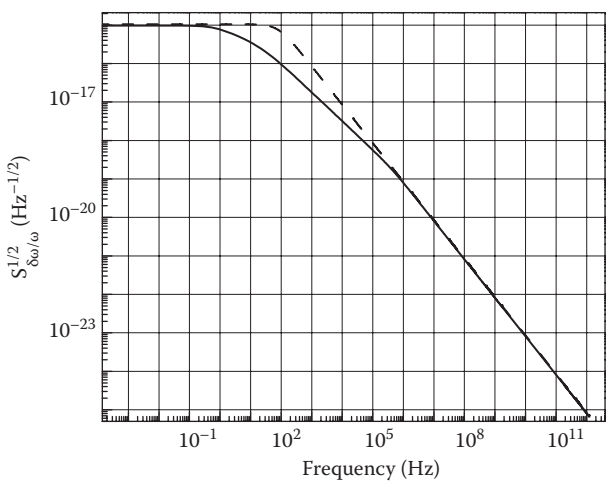

FIGURE 3.48
Spectral density of the photothermal fluctuations of a WGM frequency ($S^{1/2}_{\delta\omega/\omega}=\alpha_n S^{1/2}_{ti}$) calculated for a fluorite resonator with R=0.3 cm and L=0.01 cm interrogated with coherent 3.55 μm light of 1 mW power assuming that the light is absorbed in the resonator. Solid (dashed) line stands for the simulation (analytical calculations). (Reprinted from Matsko, A. B., Savchenkov, A. A., Yu, N., and Maleki, L., *J. Opt. Soc. Am. B* 24, 1324–1335, 2007. With permission from OSA.)

where $m^* \approx \rho V_r$ is the effective mass of the oscillator, $\delta P(t)$ is the variation of the optical power in the corresponding WGM. Calculating $\delta P(t)$ using general Langevin formalism we derive an expression for the spectral density of the fluctuations:

$$S_{\Delta R/R} = \left(\frac{2\pi}{m^* cR}\right)^2 \frac{\hbar \omega_{m,q,p} \langle P \rangle}{\tau_0} \frac{2\gamma_R}{\gamma_R^2 + \Omega^2} \frac{1}{(\Omega_0^2 - \Omega^2)^2 + \Gamma_0^2 \Omega^2}, \tag{3.77}$$

where γ_R is the spectral width of the mode. Because generally $\Omega_0 \gg \gamma_R, \Gamma_0$ we find an expression for the square deviation of the radius of the resonator resulting from the fluctuations of the radiation pressure:

$$\frac{\langle \Delta R^2(t) \rangle^{1/2}}{R} \simeq \frac{2\pi}{m^* cR} \left[\frac{\hbar \omega_{m,q,p} \langle P \rangle}{\tau_0 \Omega_0^4} \left(1 + \frac{\gamma_R}{\Gamma_0}\right)\right]^{1/2}. \tag{3.78}$$

Let us estimate the value for a fluorite resonator with $R = 0.3$ cm and $L = 0.01$ cm interrogated with coherent 1.55 μm light of 1 mW power. We also assume that $\gamma_R = 2\pi \times 10^4$ rad/s and $\Gamma_0 = 100$ rad/s. We find the averaged power inside the resonator $\langle P \rangle = 1 \text{ mW} / \tau_0 \gamma_R \simeq 250$ W, square deviation of the radius $(\langle \Delta R^2(t) \rangle / R^2)^{1/2} \simeq 5.5 \times 10^{-16}$, and low frequency spectral density $(S_{\Delta R/R}(0))^{1/2} = 3 \times 10^{-18}$ Hz$^{-1/2}$. The corresponding spectral density of frequency fluctuations for $K_\varepsilon = 4$ is shown in Figure 3.49.

Our calculations show that the radiation pressure fluctuations are comparably weak in a sufficiently large WGM resonator, and can be neglected in the majority of cases when the resonator is interrogated with low power light.

3.7.3 Stabilization Scheme: An Example

We have shown [184] that it is fundamentally possible to reach high frequency stability of WGMs by properly selecting the operating conditions along with the host material, as well as the morphology of the resonator. In what follows we discuss a triple-mode technique. This technique is purely photonic and it enables stabilization of the WGM frequency better than the fundamental thermodynamic limit.

We propose to use three WGMs to suppress both thermorefractive and thermal expansion noise. Let us consider a spherical magnesium fluoride resonator with crystalline axis corresponding to the Z axis of a coordinate frame. The resonator is kept at 176°C where modes polarized perpendicular to the Z axis have a negligible thermorefractive effect. We propose to excite the TM mode in the XY plane and the TE mode in the XZ plane. Both modes have identical vanishing thermorefraction. A comparison of the frequency difference between these modes ($\omega_{RF} + \Delta\tilde{\omega}_{RF2}$) with the frequency of an RF reference gives averaged resonator temperature because

$$\Delta\tilde{\omega}_{RF2} \sim \omega(\alpha_{lo} - \alpha_{le}) \Delta T_R, \tag{3.79}$$

where $\Delta\tilde{\omega}_{RF2}$ is the variation of the frequency difference between the two modes determined by the temperature fluctuations of the resonator, ω is the optical frequency, and α_{lo} (α_{le}) is the thermal expansion coefficient for X and Y (Z) directions. The third mode, TE, is excited in the XY plane. The frequency difference between this mode and the TM mode in the same plane contains information about the temperature in the WGM channel. Both modes are influenced by the thermal expansion in the same way. Using results of the

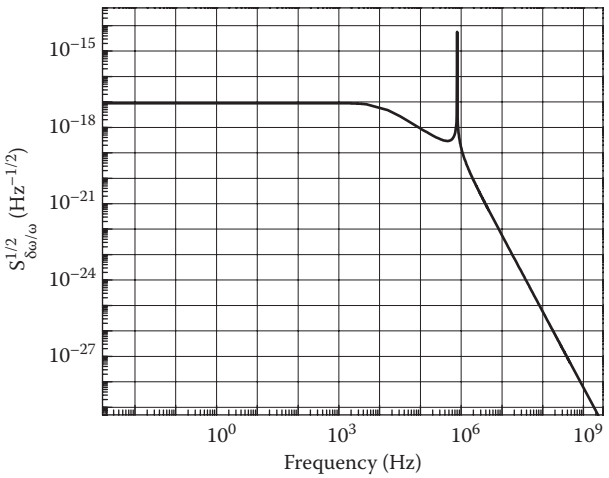

FIGURE 3.49
Spectral density of the ponderomotive backaction fluctuations of frequency ($S^{1/2}_{\delta\omega/\omega} = (1 + K_\varepsilon/2)S^{1/2}_{\Delta R/R}$) calculated for a fluorite resonator with $R = 0.3$ cm and $L = 0.01$ cm interrogated with 1 mW coherent light. (Reprinted from Matsko, A. B., Savchenkov, A. A., Yu, N., and Maleki, L., *J. Opt. Soc. Am. B* 24, 1324–1335, 2007. With permission from OSA.)

temperature measurements it is possible to design a proper feedback and/or compensation scheme that results in the suppression of both thermorefractive and thermal expansion fluctuations for the TM mode family in the XY plane. The relative stability of those modes is determined by expression

$$\frac{\Delta\omega_{\mathrm{TM}}}{\omega} \sim \frac{\alpha_{lo}}{\alpha_{lo} - \alpha_{le}} \frac{\Delta\tilde{\omega}_{\mathrm{RF2}}}{\omega}. \tag{3.80}$$

It is possible to achieve $\Delta\omega_{\mathrm{TM}} \sim \tilde{\omega}_{\mathrm{RF2}}$ if $\alpha_{lo} \neq \alpha_{le}$.

It is also possible to measure the resonator temperature with a sensitivity exceeding the fundamental thermodynamic limit. The measurement sensitivity is limited by $\Delta\tilde{\omega}_{\mathrm{RF2}}/(\omega(\alpha_{lo} - \alpha_{le}))$, which can be very small if $\Delta\tilde{\omega}_{\mathrm{RF2}}$ is small enough. Hence, the triple mode technique results in the possibility of compensation of the thermodynamic noise exceeding the fundamental thermodynamic limit. There is nothing special in the suppression of the fundamental thermorefractive frequency fluctuations of an optical mode, if one manages to lock this mode to an ultrastable optical frequency reference. The advantage of the proposed technique is in the possibility to stabilize an optical frequency beyond the thermodynamic limit using an RF reference. This feature will result in realization of stable UV, as well as FIR, lasers using crystalline WGM resonators.

3.7.4 Applications for Laser Stabilization

WGM resonators are naturally attractive for frequency stabilization of lasers as well as for fabrication of other kinds of frequency references. Preliminary experiments with stabilization of two diode lasers with a fused silica microsphere have been performed [58]. The result of that work was not very impressive compared with the best results of laser frequency stabilization using FP resonators since (i) the microsphere was not temperature stabilized, (ii) light coupling into and out of the microsphere was not stabilized, and

(iii) relative drift of the laser frequency resulting from the fluctuations of the driving currents was not stabilized.

Very recently, we have demonstrated injection locking of DFB lasers to crystalline WGM resonators. Initial measurements of the beat note of two lasers locked to calcium fluoride and lithium tantalate resonators show that the laser linewidth is less than 2 kHz (Figure 3.50). Further studies of the locking efficiency are required.

3.8 Conclusion

In this chapter, we have discussed the basic linear properties of crystalline optical WGM resonators. We have elucidated advantages of these resonators in practical application such as optical and microwave filtering. We have highlighted some important applications of the resonators in metrology for optical and microwave frequency stabilization, where a long photon storage time helps to suppress phase and frequency deviation of oscillators. The results of our R&D efforts clearly show the ample opportunities in applications of the resonators.

Because of the volume restrictions, we were unable to cover other applications of the microresonators, covered in the other chapters of the book. For instance, high-Q and long recirculation of light in compact WGM resonators offers interesting new capabilities in spectroscopy and sensing, where the change in Q or resonance frequency of WGMs can serve as a measure of absorption in the surrounding medium, or in a small (down to single molecule) quantity of deposited substance on resonator surface. The resonator can also be used for measurement of change in ambient parameters, such as temperature, pressure, motion, etc.

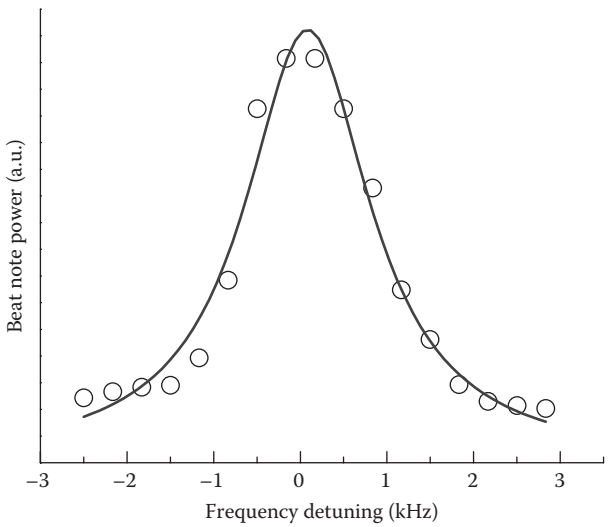

FIGURE 3.50
The beating signal of two lasers one of which is locked to a lithium tantalate resonator with loaded bandwidth approximately 3 MHz and calcium fluoride resonator with loaded bandwidth approximately 400 KHz. Laser power in the fiber at the exit of the resonator is 300 μW and 100 μW for $LiTaO_3$ and CaF_2 resonators, respectively. The resolution bandwidth of the measurement is 300 Hz and the video bandwidth is 30 kHz.

References

1. C. G. B. Garrett, W. Kaiser, and W. L. Bond. Stimulated emission into optical whispering gallery modes of spheres. *Phys. Rev*. 124, 1807–1809, 1961.
2. P. Walsh and G. Kemeny. Laser operation without spikes in a ruby ring. *J. Appl. Phys*. 34, 956–957, 1963.
3. A. Ashkin and J. M. Dziedzic. Observation of resonances in the radiation pressure on dielectric spheres. *Phys. Rev. Lett*. 38, 1351–1354, 1977.
4. P. Chylek, J. T. Kiehl, and M. K. W. Ko. Optical levitation and partial-wave resonances. *Phys. Rev. A* 18, 2229–2233, 1978.
5. A. Ashkin and J. M. Dziedzic. Observation of optical resonances of dielectric spheres by light scattering. *Appl. Opt*. 20, 1803–1814, 1981.
6. P. Chyek, V. Ramaswamy, A. Ashkin, and J. M. Dziedzic. Simultaneous determination of refractive index and size of spherical dielectric particles from light scattering data. *Appl. Opt*. 22, 2302–2307, 1983.
7. J. F. Owen, P. W. Barber, B. J. Messinger, and R. K. Chang. Determination of optical-fiber diameter from resonances in the elastic scattering spectrum. *Opt. Lett*. 6, 272–274, 1981.
8. R. E. Benner, P. W. Barber, J. F. Owen, and R. K. Chang. Observation of structure resonances in the fluorescence-spectra from microspheres. *Phys. Rev. Lett*. 44, 475–478, 1980.
9. S. C. Hill, R. E. Benner, C. K. Rushforth, and P. R. Conwell. Structural resonances observed in the fluorescence emission from small spheres on substrates. *Appl. Opt*. 23, 1680–1683, 1984.
10. S. C. Hill, R. E. Benner, C. K. Rushforth, and P. R. Conwell. Sizing dielectric spheres and cylinders by aligning measured and computed resonance locations: algorithm for multiple orders. *Appl. Opt*. 24, 2380–2390, 1985.
11. R. Thurn and W. Kiefer. Raman-microsampling technique applying optical levitation and radiation pressure. *Appl. Spectr*. 38, 78–83, 1984.
12. S.-X.Qian, J. B. Snow, and R. K. Chang. Coherent Raman mixing and coherent anti-Stokes Raman scattering from individual micrometer-size droplets. *Opt. Lett*. 10, 499–501, 1985.
13. J. B. Snow, S.-X.Qian, and R. K. Chang. Stimulated Raman scattering from individual water and ethanol droplets at morphody-dependent resonances. *Opt. Lett*. 10, 37–39, 1985.
14. H. M. Tzeng, K. F. Wall, M. B. Long, and R. K. Chang. Laser emission from individual droplets at wavelengths corresponding to morphology-dependent resonances. *Opt. Lett*. 9, 499–501, 1984.
15. H. B. Lin, A. L. Huston, B. J. Justus, and A. J. Campillo. Some characteristics of a droplet whispering-gallery-mode laser. *Opt. Lett*. 11, 614–616, 1986.
16. L. Collot, V. Lefevre-Seguin, M. Brune, J.-M. Raimond, and S. Haroshe. Very high-Q whispering-gallery mode resonances observed in fused silica microspheres. *Europhys. Lett*. 23, 327–334, 1993.
17. M. L. Gorodetsky, A. A. Savchenkov, and V. S. Ilchenko. Ultimate Q of optical microsphere resonators. *Opt. Lett*. 21, 453–455, 1996.
18. S. Shiller and R. L. Byer. High-resolution spectroscopy of whispering gallery modes in large dielectric spheres. *Opt. Lett*. 16, 130–132, 1991.
19. D. R. Rowland, and J. D. Love. Evanescent wave coupling of whispering gallery modes of a dielectric cylinder, IEE Proceedings. *J. Optoelectronics* 140, 177–188, 1993.
20. M. L. Gorodetsky and V. S. Ilchenko. High-Q optical whispering gallery microresonators–precession approach for spherical mode analysis and emission patterns with prism couplers. *Opt. Comm*. 113, 133–143, 1994.
21. M. L. Gorodetsky, A. D. Pryamikov, and V. S. Ilchenko. Rayleigh scattering in high-Q microspheres. *J. Opt. Soc. Am. B* 17, 1051–1057, 2000.
22. D. G. Blair and I. N. Evans. High Q microwave properties of a sapphire ring resonator. *J. Phys. D* 15, 1651–1656, 1982.

23. V. B. Braginsky. V. P. Mitrofanov and V. I. Panov. *Systems with small dissipation*. Chicago University Press, Chicago, IL, 1985.
24. V. B. Braginsky, V. S. Ilchenko, and K. S. Bagdassarov. Experimental observation of fundamental microwave absorption in high quality dielectric crystals. *Phys. Lett. A* 120, 300–305, 1987.
25. W. L. Bond. Making crystal spheres. *Rev. Sci. Instr*. 25, 401–401, 1954.
26. D. A. Cohen and A. F. J. Levi. Microphotonic components for a mm-wave receiver. *Solid State Electron*. 45, 495–505, 2001.
27. T. Baer. Continuous-wave laser oscillation in a Nd:YAG sphere. *Opt. Lett*. 12, 392–394, 1987.
28. V. S. Ilchenko, X. S. Yao, and L. Maleki. Microsphere integration in active and passive photonics devices. *Proc. SPIE* 3930, 154–162, 2000.
29. V. S. Ilchenko and L. Maleki. Novel whispering-gallery resonators for lasers, modulators, and sensors. *Proc. SPIE* 4270, 120–130, 2001.
30. D. A. Cohen and A. F. J. Levi. Microphotonic millimetre-wave receiver architecture. *Electron. Lett*. 37, 37–39, 2001.
31. D. A. Cohen, M. Hossein-Zadeh, and A. F. J. Levi. Microphotonic modulator for microwave receiver. *Electron. Lett*. 37, 300–301, 2001.
32. D. A. Cohen, M. Hossein-Zadeh, and A. F. J. Levi. High-Q microphotonic electro-optic modulator. *Solid State Electron*. 45, 1577–1589, 2001.
33. D. K. Serkland, R. C. Eckardt, and R. L. Byer. Continuous-wave total-internal-reflection optical parametric oscillator pumped at 1064 nm. *Opt. Lett*. 19, 1046–1048, 1994.
34. A. A. Savchenkov, A. B. Matsko, V. S. Ilchenko, and L. Maleki. Optical resonators with ten million finesse. *Opt. Express* 15, 6768–6773, 2007.
35. G. Lee. Realization of ultrasmooth surface with atomic scale step structure on $LiNbO_3$ and $LiTaO_3$ substrates. *Opt. Express* 10, 556–560, 2002.
36. J. L. Yuan, P. Zhao, J. Ruan, Z. X. Cao, W. H. Zhao, and T. Xing. Lapping and polishing process for obtaining super-smooth surfaces of quartz crystal. *J. Mat. Process. Technol*. 138, 116–119, 2003.
37. J. W. Yan, K. Syoji, and J. Tamaki. Crystallographic effects in micro/nanomachining of single-crystal calcium fluoride. *J. Vac. Sci. Technol*. 22, 46–51, 2004.
38. I. S. Grudinin, A. B. Matsko, A. A. Savchenkov, D. Strekalov, V. S. Ilchenko, and L. Maleki. Ultra high Q crystalline microcavities. *Opt. Commun*. 265, 33–38, 2006.
39. J. W. Yan, J. Tamaki, K. Syoji, T. Kuriyagawa. Single-point diamond turning of CaF_2 for nanometric surface. *Int. J. Adv. Manuf. Technol*. 24, 640–646, 2004.
40. S. T. Chu, B. E. Little, V. Van, J. V. Hryniewicz, P. P. Absil, F. G. Johnson, D. Gill, O. King, F. Seiferth, M. Trakalo, and J. Shanton. Compact full C-band tunable filters for 50 GHz channel spacing based on high order micro-ring resonators. Optical Fiber Communication Conference 2004, presentation PDP9.
41. C. H. Townes and A. L. Shawlow. *Microwave spectroscopy.* McGraw-Hill, New York, 1955.
42. J. P. Gordon. Variable coupling reflection cavity for microwave spectroscopy. *Rev. Scientific Instruments* 32, 658–661, 1961.
43. A. Yariv. Critical coupling and its control in optical waveguide-ring resonator systems. *IEEE Photon. Tech. Lett*. 14, 483–485, 2002.
44. R. Ulrich. Theory of the prism-film coupler by plane wave analysis. *J. Opt. Soc. Am*. 60, 1337–1350, 1970.
45. P. K. Tien and R. Ulrich. Theory of prism-film coupler and thin film light guides. *J. Opt. Soc. Am*. 60, 1325–1336, 1970.
46. A. V. Chelnokov, and J.-M. Lourtioz. Optimized coupling into planar waveguides with cylindrical prisms. *Electron. Lett*. 31, 269–271, 1995.
47. D. Sarid, P. J. Cressman, and R. L. Holman. High-efficiency prism coupler for optical waveguides. *Appl. Phys. Lett*. 33, 514–515, 1978.
48. D. Sarid. High efficiency input-output prism waveguide coupler: an analysis. *Appl. Optics* 18, 2921–2926, 1979.
49. M. L. Gorodetsky and V. S. Ilchenko. Optical microsphere resonators: optimal coupling to high-Q whispering-gallery modes. *J. Opt. Soc. Am. B* 16, 147–154, 1999.

50. F. Treussart, V. S. Ilchenko, J. F. Roch, J. Hare, V. Lefevre-Seguin, J. M. Raimond, and S. Haroche. Evidence for intrinsic Kerr bistability of high-Q microsphere resonators in superfluid helium. *Eur. Phys. J. D* 1, 235–238, 1998.
51. Y. L. Pan and R. K. Chang. Highly efficient prism coupling to whispering gallery modes of a square μ cavity. *Appl. Phys. Lett*. 82, 487–489, 2003.
52. M. Mohageg, A. Savchenkov, and L. Maleki. High-Q optical whispering gallery modes in elliptical $LiNbO_3$ resonant cavities. *Opt. Express* 15, 4869–4875, 2007.
53. A. A. Savchenkov, I. S. Grudinin, A. B. Matsko, D. Strekalov, M. Mohageg, V. S. Ilchenko, and L. Maleki. Morphology-dependent photonic circuit elements. *Opt. Lett*. 31, 1313–1315, 2006.
54. A. Serpenguzel, S. Arnold, and G. Griffel. Excitation of resonances of microspheres on an optical fiber. *Opt. Lett*. 20, 654–656, 1995.
55. G. Griffel, S. Arnold, D. Taskent, A. Serpenguzel, J. Connoly, and N. Morris. Morphology-dependent resonances of a microsphere-optical fiber system. *Opt. Lett*. 21, 695–697, 1995.
56. N. Dubreuil, J. C. Knight, D. Leventhal, V. Sandoghdar, J. Hare, V. Lefevre-Seguin, J. M. Raimond, and S. Haroche. Eroded monomode optical fiber for whispering-gallery mode excitation in fused-silica microspheres. *Opt. Lett*. 20, 1515–1517, 1995.
57. V. S. Ilchenko, X. S. Yao, and L. Maleki. Pigtailing the high-Q microsphere cavity: a simple fiber coupler for optical whispering-gallery modes. *Opt. Lett*. 24, 723–725, 1999.
58. V. V. Vassiliev, V. L. Velichansky, V. S. Ilchenko, M. L. Gorodetsky, L. Hollberg, and A. V. Yarovitsky. Narrow-line-width diode laser with a high-Q microsphere resonator. *Opt. Comm*. 158, 305–312, 1998.
59. V. V. Vassiliev, S. M. Ilina, and V. L. Velichansky. Diode laser coupled to a high-Q microcavity via a GRIN lens. *Appl. Phys. B* 76, 521–523, 2003.
60. J. C. Knight, G. Cheung, F. Jacques, and T. A. Birks. Phase-matched excitation of whispering gallery mode resonances using a fiber taper. *Opt. Lett*. 22, 1129–1131, 1997.
61. M. K. Chin and S. T. Ho. Design and modeling of waveguide-coupled single-mode microring resonators. *J. Lightwave. Technol*. 16, 1433–1446, 1998.
62. B. E. Little, J. P. Laine, and H. A. Haus. Analytic theory of coupling from tapered fibers and half-blocks into microsphere resonators. *J. Lightwave. Technol*. 17, 704–715, 1999.
63. M. Cai, O. Painter, and K. J. Vahala. Observation of critical coupling in a fiber taper to a silica-microsphere whispering-gallery mode system. *Phys. Rev. Lett*. 85, 74–77, 2000.
64. M. Cai and K. J. Vahala. Highly efficient optical power transfer to whispering-gallery modes by use of a symmetrical dual-coupling configuration. *Opt. Lett*. 25, 260–262, 2000.
65. S. M. Spillane, T. J. Kippenberg, O. J. Painter, and K. J. Vahala. Ideality in a fiber-taper-coupled microresonator system for application to cavity quantum electrodynamics. *Phys. Rev. Lett*. 91, 043902, 2003.
66. P. E. Barclay, K. Srinivasan, and O. Painter. Design of photonic crystal waveguides for evanescent coupling to optical fiber tapers and integration with high-Q cavities. *J. Opt. Soc. Am. B* 20, 2274–2284, 2003.
67. A. Nurenberg and G. Schweiger. Excitation and recording of morphology-dependent resonances in spherical microresonators by hollow light guiding fibers. *Appl. Phys. Lett*. 84, 2043–2045, 2004.
68. K. Srinivasan, P. E. Barclay, M. Borselli, and O. Painter. Optical-fiber-based measurement of an ultrasmall volume high-Q photonic crystal microcavity. *Phys. Rev. B* 70, 081306, 2004.
69. H. Konishi, H. Fujiwara, S. Takeuchi, K. Sasaki. Polarization-discriminated spectra of a fiber-microsphere system. *Appl. Phys. Lett*. 89, 121107, 2006.
70. C. P. Michael, M. Borselli, T. J. Johnson, C. Chrystal, and O. Painter. An optical fiber-taper probe for wafer-scale microphotonic device characterization. *Opt. Express* 15, 4745–4752, 2007.
71. P. E. Barclay, K. Srinivasan, O. Painter, B. Lev, and H. Mabuchi. Integration of fiber coupled high-Q SiNx microdisks with atom chips. *Appl. Phys. Lett*. 89, 131108, 2006.
72. F. C. Blom, D. R. van Dijk, H. J. W. M. Hoekstra, A. Driessen, and Th. J. A. Popma. Experimental study of integrated-optics microcavity resonators: Toward an all-optical switching device. *Appl. Phys. Lett*. 71, 747–749, 1997.

73. D. Rafizadeh, J. P. Zhang, S. C. Hagness, A. Taflove, K. A. Stair, S. T. Ho, and R. C. Tiberio. Waveguide-coupled AlGaAs/GaAs microcavity ring and disk resonators with high finesseand 21.6-nm free spectral range. *Opt. Lett*. 22, 1244–1246, 1997.
74. B. E. Little, S. T. Chu, W. Pan, D. Ripin, T. Kaneko, Y. Kokubun, and E. Ippen. Vertically coupled glass microring resonator channel dropping filters. *IEEE Photon. Technol. Lett*. 11, 215–217, 1999.
75. P. Rabiei, W. H. Steier, C. Zhang, and L. R. Dalton. Polymer microring filters and modulators. *J. Lightwave Technol*. 20, 1968–1975, 2002.
76. D. V. Tishinin, P. D. Dapkus, A. E. Bond, I. Kim, C. K. Lin, and J. O'Brien. Vertical resonant couplers with precision coupling efficiency control fabricated by wafer bonding. *IEEE Photon. Technol. Lett*. 11, 1003–1005, 1999.
77. M. R. Poulsen, P. I. Borel, J. Fage-Pedersen, J. Hubner, M. Kristensen, J. H. Povlsen, K. Rottwitt, M. Svalgaard, and W. Svendsen. Advances in silica-based integrated optics. *Opt. Engin*. 42, 2821–2834, 2003.
78. S. J. Choi, K. Djordjev, S. J. Choi, P. D. Dapkus, W. Lin, G. Griffel, R. Menna, and J. Connolly. Microring resonators vertically coupled to buried heterostructure bus waveguides. *IEEE Photon. Technol. Lett*. 16, 828–830, 2004.
79. C. W. Tee, K. A. Williams, R. V. Penty, I. H. White. Fabrication-tolerant active-passive integration scheme for vertically coupled microring resonator. *IEEE J. Sel. Top. Quantum Electron*. 12, 108–116, 2006.
80. T. Le, A. A. Savchenkov, H. Tazawa, W. H. Steier, and L. Maleki, Polymer optical waveguide vertically coupled to high-Q whispering gallery resonators. *IEEE Photon. Technol. Lett*. 18, 859–861, 2006.
81. B. E. Little, J.-P. Laine, D. R. Lim, H. A. Haus, L. C. Kimerling, and S. T. Chu. Pedestal antiresonant reflecting waveguides for robust coupling to microsphere resonators and for microphotonic circuits. *Opt. Lett*. 25, 73–75, 2000.
82. J. P. Laine, B. E. Little, D. R. Lim, H. C. Tapalian, L. C. Kimerling, and H. A. Haus. Microsphere resonator mode characterization by pedestal anti-resonant reflecting waveguide coupler. *IEEE Photon. Technol. Lett*. 12, 1004–1006, 2000.
83. I. M. White, H. Oveys, X. Fan, T. L. Smith, and J. Zhang. Integrated multiplexed biosensors based on liquid core optical ring resonators and antiresonant reflecting optical waveguides. *Appl. Phys. Lett*. 89, 191106, 2006.
84. I. M. White, J. D. Suter, H. Oveys, X. Fan, T. L. Smith, J. Zhang, B. J. Koch, and M. A. Haase. Universal coupling between metal-clad waveguides and optical ring resonators. *Opt. Express* 15, 646–651, 2007.
85. A. Morand, K. Phan-Huy, Y. Desieres, and P. Benech. Analytical study of the microdisk's resonant modes coupling with a waveguide based on the perturbation theory. *J. Lightwave Technol*. 22, 827–832, 2004.
86. A. Belarouci, K. B. Hill, Y. Liu, Y. Xiong, T. Chang, and A. E. Craig. Design and modeling of waveguide-coupled microring resonator. *J. Luminescence* 94, 35–38, 2001.
87. C. Li, L. J. Zhou, S. M. Zheng, and A. W. Poon. Silicon polygonal microdisk resonators. *IEEE J. Sel. Top. Quantum Electron*. 12, 1438–1449, 2006.
88. V. S. Ilchenko, M. L. Gorodetsky, X. S. Yao, and L. Maleki. Microtorus: a high-finesse microcavity with whispering-gallery modes. *Opt. Lett*. 26, 256–258, 2001.
89. D. K. Armani, T. J. Kippenberg, S. M. Spillane, and K. J. Vahala. Ultra-high-Q toroid microcavity on a chip. *Nature* 421, 925–928, 2003.
90. M. Sumetsky. Whispering-gallery-bottle microcavities: the three-dimensional etalon. *Opt. Lett*. 29, 8–10, 2004.
91. V. S. Ilchenko, A. A. Savchenkov, A. B. Matsko, and L. Maleki. Dispersion compensation in whispering-gallery modes. *J. Opt. Soc. Am. A* 20, 157–162, 2003.
92. L. G. Guimaraes and H. M. Nussenzveig. Theory of Mie resonances and ripple fluctuations. *Opt. Commun*. 89, 363–369, 1992.
93. D. Q. Chowdhury, S. C. Hill, and P. W. Barber. Morphology-dependent resonances in radially inhomogeneous spheres. *J. Opt. Soc. Am. A* 8, 1702–1705, 1991.

94. B. Z. Katsenelenbaum, L. Mercader del Rio, M. Pereyaslavets, M. Sorolla Ayza, and M. Thumm. *Theory of nonuniform waveguides: the cross-section method*. Institute of Electrical Engineers, London, 1998.
95. V. S. Ilchenko, A. A. Savchenkov, A. B. Matsko, and L. Maleki. Tunability and synthetic lineshapes in high-Q optical whispering gallery modes. *Proc. SPIE* 4969, 195–206, 2003.
96. M. L. Gorodetsky and A. E. Fomin. Geometrical theory of whispering-gallery modes. *IEEE J. Sel. Top. Quantum Electron*. 12, 33–39, 2006.
97. G. Meijer, M. G. H. Boogaarts, R. T. Jongma, D. H. Parker, and A. M. Wodtke. Coherent cavity ring down spectroscopy. *Chem. Phys. Lett*. 217, 112–116, 1994.
98. V. S. Ilchenko, A. A. Savchenkov, A. B. Matsko, and L. Maleki. Whispering-gallery-mode electro-optic modulator and photonic microwave receiver. *J. Opt. Soc. Am. B* 20, 333–342, 2003.
99. A. Wicht, K. Danzmann, M. Fleischhauer, M. Scully, G. Müller, and R.-H. Rinkleff. White-light cavities, atomic phase coherence, and gravitational wave detectors. *Opt. Commun*. 134, 431–439, 1997.
100. G. S. Pati, M. Salit, K. Salit, and M. S. Shahriar. Demonstration of a tunable-bandwidth white-light interferometer using anomalous dispersion in atomic vapor. *Phys. Rev. Lett*. 99, 133601, 2007.
101. A. A. Savchenkov, A. B. Matsko, and L. Maleki. White-light whispering gallery mode resonators. *Opt. Lett*. 31, 92–94, 2006.
102. W. von Klitzing, R. Long, V. S. Ilchenko, J. Hare, and V. Lefevre-Seguin. Frequency tuning of the whispering-gallery modes of silica microspheres for cavity quantum electrodynamics and spectroscopy. *Opt. Lett*. 26, 166–168, 2001.
103. S. Blair and Y. Chen. Resonant-enhanced evanescent-wave fluorescence biosensing with cylindrical optical cavities. *Appl. Optics* 40, 570–582, 2001.
104. R. W. Boyd and J. E. Heebner. Sensitive disk resonator photonic biosensor. *Appl. Optics* 40, 5742–5747, 2001.
105. E. Krioukov, D. J. W. Klunder, A. Driessen, J. Greve, and C. Otto. Sensor based on an integrated optical microcavity. *Opt. Lett*. 27, 512–514, 2002.
106. S. Arnold, M. Khoshsima, I. Teraoka, S. Holler, and F. Vollmer. Shift of whispering-gallery modes in microspheres by protein adsorption. *Opt. Lett*. 28, 272–274, 2003.
107. F. Vollmer, S. Arnold, D. Braun, I. Teraoka, and A. Libchaber. Multiplexed DNA quanti. cation by spectroscopic shift of two microsphere cavities. *Biophys. J*. 85, 1974–1979, 2003.
108. C. Y. Chao and L. J. Guo. Design and optimization of microring resonators in biochemical sensing applications. *J. Lightwave Technol*. 24, 1395–1402, 2006.
109. S. Y. Cho and N. M. Jokerst. A polymer microdisk photonic sensor integrated onto silicon. *IEEE Photon. Technol. Lett*. 18, 2096–2098, 2006.
110. N. M. Hanumegowda, I. M. White, and X. D. Fan. Aqueous mercuric ion detection with microsphere optical ring resonator sensors. *Sensors Actuators B* 120, 207–212, 2006.
111. A. M. Armani, R. P. Kulkarni, S. E. Fraser, R. C. Flagan, and K. J. Vahala. Label-free, single-molecule detection with optical microcavities. *Science* 317, 783–787, 2007.
112. H. Zhu, I. M. White, J. D. Suter, P. S. Dale, and X. Fan. Analysis of biomolecule detection with optofluidic ring resonator sensors. *Opt. Express* 15, 9139–9146, 2007.
113. F. Xu, P. Horak, and G. Brambilla. Optical microfiber coil resonator refractometric sensor. *Opt. Express* 15, 7888–7893, 2007; *Opt. Express* 15, 9385–9385, 2007.
114. M. Sumetsky. Optimization of optical ring resonator devices for sensing applications. *Opt. Lett*. 32, 2577–2579, 2007.
115. A. T. Rosenberger. Analysis of whispering-gallery microcavity-enhanced chemical absorption sensors. *Opt. Express* 15, 12959–12964, 2007.
116. A. A. Savchenkov, A. B. Matsko, D. Strekalov, V. S. Ilchenko, and L. Maleki. Mode filtering in optical whispering gallery resonators. *Electron. Lett*. 41, 495–497, 2005.
117. M. Kuznetsov, M. Stern, and J. Coppeta. Single transverse mode optical resonators. *Opt. Express* 13, 171–181, 2005.
118. R. G. Hunsperger. *Integrated Optics: Theory and Technology.* Springer Verlag, Berlin, 2002.

119. S.-T. Ho, D. Y. Chu, J.-P. Zhang, S. Wu, and M.-K. Chin. In *Optical processes in microcavities* R. K. Chang and A. J. Campillo (Eds). Word Scientific, Singapore, 1996, p. 339.
120. M. V. Berry. Regularity and chaos mechanics, illustrated in classical by three deformations of a circular "billiard". *Eur. J. Phys*. 2 91–102, 1981.
121. A. Ancey, A. Folacci, and P. Gabrielli. Exponentially improved asymptotic expansions for resonances of an elliptic cylinder. *J. Phys. A: Math. Gen*. 33, 3179–3208, 2000.
122. S. Ancey, A. Folacci, and P. Gabrielli. Whispering-gallery modes and resonances of an elliptic cavity. *J. Phys. A: Math. Gen*. 34, 1341–1359, 2001; *J. Phys. A: Math. Gen*. 34, 2657–2657, 2001.
123. S. V. Boriskina, T. M. Benson, P. Sewell, and A. I. Nosich. Tuning of elliptic whispering-gallery-mode microdisk waveguide filters. *J. Lightwave Technol*. 21, 1987–1995, 2003.
124. L. Zhang, Y. -X. Wang, F. Zhang, and R. O. Claus. Observation of whispering-gallery and directional resonant laser emission in ellipsoidal microcavities. *J. Opt. Soc. Am. B* 23, 1793–1800, 2006.
125. G. Rempe, R. J. Thompson, H. J. Kimble, and R. Lalezari. Measurement of ultralow losses in an optical interferometer. *Opt. Lett*. 17, 363–365, 1992.
126. C. J. Hood, H. J. Kimble, and J. Ye. Characterization of high-finesse mirrors: Loss, phase shifts, and mode structure in an optical cavity. *Phys. Rev. A* 64, 033804, 2001.
127. H. R. Bilger, P. V. Wells, and G. E. Stedman. Origins of fundamental limits for reflection losses at multilayer dielectric mirrors. *Appl. Opt*. 33, 7390–7396, 1994.
128. H.-J. Cho, M.-J. Shin, and J.-C. Lee. Effects of substrate and deposition method onto the mirror scattering. *Appl. Opt*. 45, 1440–1446, 2006.
129. E. M. Purcell. Spontaneous emission probabilities at radio frequencies. *Phys. Rev*. 69, 681–681, 1946.
130. A. B. Matsko, A. A. Savchenkov, D. Strekalov, V. Ilchenko, and L. Maleki. Optical hyperparametric oscillations in a whispering-gallery-mode resonator: Threshold and phase diffusion. *Phys. Rev. A* 71, 033804, 2005.
131. V. S. Ilchenko, A. A. Savchenkov, A. B. Matsko, and Lute Maleki. Nonlinear optics and crystalline whispering gallery mode cavities. *Phys. Rev. Lett*. 92, 043903, 2004.
132. D. W. Vernooy, V. S. Ilchenko, H. Mabuchi, E. W. Streed, and H. J. Kimble. High-Q measurements of fused-silica microspheres in the near infrared. *Opt. Lett*. 23, 247–249, 1998.
133. T. J. Kippenberg, S. M. Spillane, and K. J. Vahala. Demonstration of ultra-high-Q small mode volume toroid microcavities on a chip. *Appl. Phys. Lett*. 85, 6113–6115, 2004.
134. I. S. Grudinin, V. S. Ilchenko, and L. Maleki. Ultrahigh optical Q factors of crystalline resonators in the linear regime. *Phys. Rev. A* 74, 063806, 2006.
135. S. M. Spillane, T. J. Kippenberg, and K. J. Vahala. Ultralow-threshold Raman laser using a spherical dielectric microcavity. *Nature* 415, 621–623, 2002.
136. I. S. Grudinin and L. Maleki. Ultralow-threshold Raman lasing with CaF_2 resonators. *Opt. Lett*. 32, 166–168, 2007.
137. T. J. Kippenberg, H. Rokhsari, T. Carmon, A. Scherer, and K. J. Vahala. Analysis of radiation-pressure induced mechanical oscillation of an optical microcavity. *Phys. Rev. Lett*. 95, 033901, 2005.
138. T. J. Kippenberg, S. M. Spillane, and K. J. Vahala. Kerr-nonlinearity optical parametric oscillation in an ultrahigh-Q toroid microcavity. *Phys. Rev. Lett*. 93, 083904, 2004.
139. A. A. Savchenkov, A. B. Matsko, D. Strekalov, M. Mohageg, V. S. Ilchenko, and L. Maleki. Low threshold optical oscillations in a whispering gallery mode CaF_2 resonator. *Phys. Rev. Lett*. 93, 243905, 2004.
140. A. A. Savchenkov, A. B. Matsko, M. Mohageg, and L. Maleki. Ringdown spectroscopy of stimulated Raman scattering in a whispering gallery mode resonator. *Opt. Lett*. 32, 497–499, 2007.
141. A. A. Savchenkov, V. S. Ilchenko, A. B. Matsko, and L. Maleki. Kilohertz optical resonances in dielectric crystal cavities. *Phys. Rev. A* 70, 051804R, 2004.

142. A. B. Matsko, A. A. Savchenkov, and L. Maleki. Ring-down spectroscopy for studying properties of CW Raman lasers. *Opt. Commun*. 260, 662–665, 2006.
143. B. Wang, R. R. Rockwell, and J. List. Linear birefringence in CaF_2 measured at deep ultraviolet and visible wavelengths. *J. Microlithography, Microfabrication, and Microsystems* 3, 115–121, 2004.
144. V. Deuster, M. Schick, Th. Kayser, H. Dabringhaus, H. Klapper, and K. Wandelt. Studies of the facetting of the polished (100) face of CaF_2. *J. Cryst. Growth* 250, 313–323, 2003.
145. Q. -Z. Zhao, J. -R. Qiu, X. -W. Jiang, C. -J. Zhao, and C. -S. Zhu. Fabrication of internal diffraction gratings in calcium fluoride crystals by a focused femtosecond laser. *Opt. Express* 12, 742–746, 2004.
146. I. S. Grudinin, A. B. Matsko, and L. Maleki. On the fundamental limits of Q factor of crystalline dielectric resonators. *Opt. Express* 15, 3390–3395, 2007.
147. M. E. Lines. Scattering losses in optic fiber materials. I. A new parametrization. *J. Appl. Phys*. 55, 4052–4057, 1984; Scattering losses in optic fiber materials. II. Numerical estimates. *J. Appl. Phys.* 55, 4058–4063, 1984.
148. S. Logunov and S. Kuchinsky. Experimental and theoretical study of bulk light scattering in CaF_2 monocrystals. *J. Appl. Phys*. 98, 053501, 2005.
149. I. L. Fabelinskii. *Molecular scattering of light*. Plenum Press, New York, 1968.
150. D. C. Wallace. *Thermodynamics of crystals*. Dover, New York, 1998.
151. R. Loudon. The Raman effect in crystals. *Adv. Phys*. 50, 813–864, 2001.
152. M. Daimon and A. Masumara. High-accuracy measurements of the refractive index and its temperature coefficient of calcium fluoride in a wide wavelength range from 138 to 2326 nm. *Appl. Opt*. 41 5275–5281, 2002.
153. E. Palik. *Handbook of optical constants of solids*. Academic, New York, 1998.
154. M. Lines. Ultralow-loss glasses, *Ann. Rev. Mater. Sci*. 16, 113–135, 1986.
155. A. Laufer, J. Pirog, and J. McNesby. Effect of temperature on the vacuum ultraviolet transmittance of lithium fluoride, calcium fluoride, barium fluoride, and sapphire. *J. Opt. Soc. Am*. 55, 64–66, 1965.
156. L. L. Boyer, J. A. Harrington, M. Hass, and H. B. Rosenstock. Multiphonon absorption in ionic crystals. *Phys. Rev. B* 11, 1665–1680, 1975.
157. S. Venugopalan and A. K. Ramdas. Effect of uniaxial stress on the raman spectra of cubic crystals: CaF_2, BaF_2, and $Bi_{12}GeO_{20}$. *Phys. Rev. B* 8, 717–734, 1973.
158. R. W. Boyd. *Nonlinear optics*. Academic Press, New York, 1992.
159. A. A. Savchenkov, V. S. Ilchenko, A. B. Matsko, and L. Maleki. KiloHertz optical resonances in dielectric crystal cavities. *Phys. Rev. A* 70, 051804(R), 2004.
160. A. A. Savchenkov, V. S. Ilchenko, A. B. Matsko, and L. Maleki. Tunable filter based on whispering gallery modes. *Electron. Lett*. 39, 389–391, 2003.
161. A. A. Savchenkov, V. S. Ilchenko, A. B. Matsko, and L. Maleki. High-order tunable filters based on a chain of coupled crystalline whispering gallery mode resonators. *IEEE Photonics Technol. Lett*. 17, 136–138, 2005.
162. A. A. Savchenkov, A. B. Matsko, V. S. Ilchenko, N. Yu, and L. Maleki. Microwave photonics applications of whispering gallery mode resonators physics and engineering of microwaves. Millimeter and Submillimeter Waves and Workshop on Terahertz Technologies, 2007. MSMW '07. The Sixth International Kharkov Symposium, 1, pp. 79–84, 2007.
163. B. E. Little, S. T. Chu, H. A. Haus, J. Foresi, and J. P. Laine. Microring resonator channel dropping filters. *J. Lightwave Tech*. 15, 998–1005, 1997.
164. J. V. Hryniewicz, P. P. Absil, B. E. Little, R. A. Wilson, and P. -T. Ho. Higher order filter response in coupled microring resonators. *IEEE Phot. Tech. Lett*. 12, 320–322, 2000.
165. S. T. Chu, B. E. Little, W. Pan, T. Kaneko, and Y. Kukubun. Cascaded microring resonators for crosstalk reduction and spectrum cleanup in add-drop filters. *IEEE Phot. Tech. Lett*. 11, 1423–1425, 1999.
166. S. T. Chu, B. E. Little, W. Pan, T. Kaneko, and Y. Kukubun. Second-order filter response from parallel coupled glass microring resonators. *IEEE Phot. Tech. Lett*. 11, 1426–1428, 1999.

167. K. Djordjev, S. J. Choi, S. J. Choi, and P. D. Dapkus. Microdisk tunable resonant filters and switches. *IEEE Phot. Tech. Lett*. 14, 828–830, 2002.
168. O. Schwelb and I. Frigyes. Vernier operation of series coupled optical microring resonator filters. *Microwave Opt. Technol. Lett*. 39, 258–261, 2003.
169. J.-L. Gheorma and R. M. Osgood. Fundamental limitations of optical resonator based high-speed EO modulators. *IEEE Photon. Tech. Lett*. 14, 795–797, 2002.
170. G. Griffel. Vernier effect in asymmetrical ring resonator arrays. *IEEE Phot. Technol. Lett*. 12, 1642–1644, 2000.
171. P. Urquhart. Compound optical-fiber-based resonators. *J. Opt. Soc. Am. A* 5, 803–812, 1988.
172. K. Oda, N. Takato, and H. Toba. Wide-FSR waveguide double-ring resonator for optical FDM transmission system. *J. Lightwave Technol*. 9, 728–736, 1991.
173. M. Mohageg, A. Savchenkov, D. Strekalov, A. Matsko, V. Ilchenko, and L. Maleki. Reconfigurable optical filter. *Electron. Lett*. 41, 91–92, 2005.
174. C. K. Madsen and J. H. Zhao. A general planar waveguide autoregressive optical filter. *J. Lightwave Technol*. 14, 437–447, 1996.
175. A. B. Matsko, A. A. Savchenkov, and L. Maleki. Vertically coupled whispering-gallery-mode resonator waveguide. *Opt. Lett*. 30, 3066–3068, 2005.
176. L. Maleki, A. B. Matsko, A. A. Savchenkov, and D. Strekalov. Slow light in vertically coupled whispering gallery mode resonators. *Proc. SPIE*, 6130, 61300R, 2006.
177. A. Yariv, Y. Xu, R. K. Lee, and A. Scherer. Coupled–resonator optical waveguide: a proposal and analysis. *Opt. Lett*. 24, 711–713, 1999.
178. J. E. Heebner, P. Chak, S. Pereira, J. E. Sipe, and R. W. Boyd. Distributed and localized feedback in microresonator sequences for linear and nonlinear optics. *J. Opt. Soc. Am. B* 21, 1818–1832, 2004.
179. M. Sumetsky. Vertically-stacked multi-ring resonator. *Opt. Express* 13, 6354–6375, 2005.
180. X. S. Yao and L. Maleki. Optoelectronic microwave oscillator. *J. Opt. Soc. Am. B* 13, 1725–1735, 1996.
181. D. Strekalov, D. Aveline, N. Yu, R. Thompson, A. B. Matsko, and L. Maleki. Stabilizing an optoelectronic microwave oscillator with photonic filters. *J. Lightwave Technol*. 21, 3052–3061, 2003.
182. A. B. Matsko, L. Maleki, A. A. Savchenkov, and V. S. Ilchenko. Whispering gallery mode based optoelectronic microwave oscillator. *J. Mod. Opt*. 50, 2523–2542, 2003.
183. A. B. Matsko, A. A. Savchenkov, N. Yu, and L. Maleki. Whispering-gallery-mode resonators as frequency references. I. Fundamental limitations. *J. Opt. Soc. Am. B* 24, 1324–1335, 2007.
184. A. A. Savchenkov, A. B. Matsko, V. S. Ilchenko, N. Yu, and L. Maleki. Whispering-gallery-mode resonators as frequency references. II. Stabilization. *J. Opt. Soc. Am. B* 24, 2988–2997, 2007.
185. M. L. Gorodetsky and I. S. Grudinin. Fundamental thermal fluctuations in microspheres. *J. Opt. Soc. Am. B* 21, 697–705, 2004.
186. F. L. Walls and J. R. Vig. Fundamental limits on the frequency stabilities of crystal oscillators. *IEEE Tran. Ferroelectrics and Freq. Control* 42, 576–589, 1995.
187. V. B. Braginsky, M. L. Gorodetsky, and S. P. Vyatchanin. Thermodynamical fluctuations and photo-thermal shot noise in gravitational wave antennae. *Phys. Lett. A* 264, 1–10, 1999.
188. C. Audoin. *Proceedings of the International School of Physics Enrico Fermi*, Course LXVIII, A. F. Milone and P. Giacomo (Eds). Amsterdam, North-Holland, p. 169, 1980.
189. A. Feldman, D. Horowitz, R. M. Waxler, and M. J. Dodge. *Optical materials characterization*. National Bureau of Standards Technical Note 993. U.S. Government Printing Office, Washington DC, 1979.
190. V. B. Braginsky, V. P. Mitrofanov, and V. I. Panov. *Systems with small dissipation*. The University of Chicago Press, Chicago, IL, 1985.
191. K. Numata, A. Kemery, and J. Camp. Thermal-noise limit in the frequency stabilization of lasers with rigid cavities. *Phys. Rev. Lett*. 93, 250602, 2004.

192. K. Goda, K. McKenzie, E. E. Mikhailov, P. K. Lam, D. E. McClelland, and N. Mavalvala. Photothermal fluctuations as a fundamental limit to low-frequency squeezing in a degenerate optical parametric oscillator. *Phys. Rev. A*, 72, 043819, 2005.
193. V. B. Braginsky and S. P. Vyatchanin. Frequency fluctuations of nonlinear origin in self-sustained optical oscillators. *Phys. Lett. A* 279, 154–162, 2001.
194. S. Chang, A. G. Mann, A. N. Luiten, and D. G. Blair. Measurements of radiation pressure effect in cryogenic sapphire dielectric resonators. *Phys. Rev. Lett*. 79, 2141–2144, 1997.